

## ABSTRACT

Title of Dissertation:                   ATOMIC LAYER DEPOSITION OF ALKALI  
  PHOSPHORUS OXYNITRIDE  
  ELECTROLYTES FOR BEYOND-LITHIUM  
  NANOSCALE BATTERIES

Ramsay Blake Nuwayhid, Doctor of Philosophy,  
2022

Dissertation directed by:            Professor Gary W. Rubloff, Department of  
  Materials Science and Engineering

Lithium-ion batteries dominate portable energy storage systems today due to their light weight and high performance. However, with the continuing demand for battery capacity projected to outstrip the supply of lithium, alternative energy storage systems based on the more abundant Na and K alkali metals are attractive from both a resource perspective and their similar charge storage mechanism. Beyond limited lithium resources, there remains significant opportunity for innovation to improve battery architecture and thus performance. Nanostructured solid-state batteries (SSBs) are poised to meet the demands of next-generation energy storage technologies, with atomic layer deposition (ALD) being a powerful tool enabling high-performance nanostructured SSBs that offer competitive performance with their liquid-based counterparts. This dissertation has two main objectives: First, the development of the first reported ALD solid-state Na<sup>+</sup> and K<sup>+</sup> conductors are presented. Second, by leveraging the work on developing new solid-state Na<sup>+</sup> ion conductors, a proof-of-principle nanoscale Na-SSB is fabricated and tested.

ALD processes are developed for the Na and K based analogues of the well-known solid-state electrolyte (SSE) lithium phosphorus oxynitride (LiPON). In this case; NaPON and KPON. A comprehensive comparison of the structure, electrochemical, and processing parameters between the APON (A = Li, Na, K) family of materials is presented. The structure of NaPON closely resembles that of ALD LiPON, both possessing a N/P of 1, classifying them as alkali polyphosphazenes. Interestingly, KPON exhibits similar ALD process parameters to NaPON and LiPON, but the resulting film composition is quite different, showing little nitrogen incorporation and more closely resembling a phosphate glass.

NaPON is determined to be a promising SSE with an ionic conductivity of  $1.0 \times 10^{-7}$  S/cm at 25 °C and a wide electrochemical stability window of 0-6.0V vs. Na/Na<sup>+</sup>. The electrochemical stability and performance of NaPON as a SSE is tested in liquid-based and all solid-state battery configurations comprised of a V<sub>2</sub>O<sub>5</sub> cathode and Na metal anode. Electrochemical analysis suggests intermixing of the NaPON/V<sub>2</sub>O<sub>5</sub> layers during the ALD NaPON deposition, and further reaction during the Na metal evaporation step. The reaction during the ALD NaPON deposition on V<sub>2</sub>O<sub>5</sub> is determined to be two-fold: (1) reduction of V<sub>2</sub>O<sub>5</sub> to VO<sub>2</sub> and (2) Na<sup>+</sup> insertion into VO<sub>2</sub> to form Na<sub>x</sub>VO<sub>2</sub>. The Na metal evaporation process is found to exacerbate this reactivity, resulting in the formation of irreversible interphases leading to poor SSB performance. Despite the relatively poor performance, this work represents the first report of a nanoscale Na-SSB and showcases cryo-TEM as a powerful characterization technique to further the understanding of nanoscale SSBs. Looking forward, the intermixing during the ALD NaPON deposition does not impact the cycling of the Na<sub>x</sub>VO<sub>2</sub> electrode in liquid-based cells, with NaPON-coated electrodes outperforming unsodiated V<sub>2</sub>O<sub>5</sub> electrodes. This may be advantageous for the fabrication of SSBs, as the SSE deposition simultaneously could pre-sodiate a stable cathode material, excluding the need for *ex-*

*situ* sodiation in liquid solutions or depositing a pre-sodiated electrode material. Strategies to pair this  $\text{Na}_x\text{VO}_2/\text{NaPON}$  cathode/electrolyte with a stable anode are discussed, with a focus on the ultimate realization of a high-performance Na-SSB. This work highlights the high reactivity of Na compared to Li based battery chemistries, not only necessitating the need for interfacial coatings in Na SSBs, but also the extreme caution required during fabrication of Na-SSBs or liquid sodium-ion batteries.

ATOMIC LAYER DEPOSITION OF ALKALI PHOSPHORUS OXYNITRIDE  
ELECTROLYTES FOR BEYOND-LITHIUM NANOSCALE BATTERIES

by

Ramsay Blake Nuwayhid

Dissertation submitted to the Faculty of the Graduate School of the  
University of Maryland, College Park, in partial fulfillment  
of the requirements for the degree of  
Doctor of Philosophy  
2022

Advisory Committee:

Professor Gary Rubloff, Chair

Professor Sang-Bok Lee

Professor Eric Wachsman

Professor Paul Albertus

Professor John Cumings

© Copyright by  
Ramsay Blake Nuwayhid  
2022

## Acknowledgements

I would first like to thank my advisor, Dr. Gary Rubloff, for encouraging me and supporting me throughout my graduate studies.

Thanks to my mentors in the Rubloff group, Dr. Keith Gregorczyk and Dr. Alexander Kozen, for guiding my research and aiding my development as an independent scientist.

Thanks to all my friends and colleagues in the Rubloff group for fostering an environment that welcomes collaboration and teamwork: Kunal Ahuja, Daniela Fontecha, Victoria Ferrari, Sam Kleuter, Stefan Theodoru, Haotian Wang, Dr. David Stewart, and Dr. Angelique Jarry.

Thanks to the FabLab staff for their time and dedication to making this research possible and for making it fun: Jon Hummel, Tom Loughran, John Abrahams, and Mark Lecates.

Thanks to the IREAP support staff, for always providing a helping hand on any maintenance project in our lab or machining shadow masks for my depositions: Nolan Ballew and Don Schmadel.

Thanks to my collaborators at CINT-Sandia National Laboratories for performing cryo-EM experiments on my samples and helping me make sense of the results: Dr. Daniel Long and Dr. John Watt.

Thanks to my parents for supporting me throughout my pursuit of a Ph.D: Ramsay and Elizabeth, and my sisters: Kathryn and Allyson.

A big thanks to my friends and church family at National Community Church (NCC). I started attending NCC in my second year of my Ph.D., at a time where I was lost and seemed like everything in my life was falling apart. Through the relationships I've formed at NCC, I've experienced tremendous personal and spiritual growth, which was crucial to my development as a

leader and seeing myself as a competent researcher. Thanks to Charles Williams, Kiersten Telzerow, and Jodi Otto for calling out leadership qualities in me and positioning me to cultivate my gifts. Most importantly, none of this would have been possible without God guiding me the entire way. I give all the praise and gratitude to my Lord and Savior for positioning me to succeed when it didn't make sense to me and for His grace providing me the skills to accomplish this dissertation.

Lastly, I would like to acknowledge my funding sources over the course of my Ph.D. This work was supported by the U.S.-Israel Energy Center program, which is managed by the U.S.-Israel Binational Industrial Research and Development (BIRD). This work was also supported as part of the Nanostructures for Electrical Energy Storage (NEES), an Energy Frontier Research Center (EFRC) funded by the U.S. Department of Energy, Office of Science, Office of Basic Energy Sciences, under Award no. DESC0001160.

# Table of Contents

<b><i>Acknowledgements</i></b> .....	<b><i>ii</i></b>
<b><i>Table of Contents</i></b> .....	<b><i>iv</i></b>
<b><i>Chapter 1: Introduction</i></b> .....	<b><i>1</i></b>
<b>1.1. Motivation</b> .....	<b>1</b>
<b>1.1. Thin-Film Solid-State Batteries</b> .....	<b>1</b>
<b>1.2. Atomic Layer Deposition</b> .....	<b>3</b>
<b>1.3. Lithium Phosphorus Oxynitride</b> .....	<b>5</b>
<b>1.2. Beyond Lithium Solid-State Batteries</b> .....	<b>7</b>
<b>1.3. Review of Solid-State Sodium-Ion Conductors</b> .....	<b>9</b>
<b>1.4. Dissertation Overview</b> .....	<b>11</b>
<b><i>Chapter 2: Experimental Techniques</i></b> .....	<b><i>12</i></b>
<b>2.1. Atomic Layer Deposition Nanostructures Laboratory (ANSLab)</b> .....	<b>12</b>
<b>2.2. Atomic Layer Deposition</b> .....	<b>13</b>
<b>2.3. X-ray Photoelectron Spectroscopy</b> .....	<b>14</b>
<b>2.4. Spectroscopic Ellipsometry</b> .....	<b>16</b>
<b>2.5. Electrochemical Analysis</b> .....	<b>17</b>
<b><i>Chapter 3: Atomic Layer Deposition of Sodium Phosphorus Oxynitride: A Conformal Solid-State Sodium-Ion Conductor</i></b> .....	<b><i>19</i></b>
<b>3.1. Chapter Summary</b> .....	<b>19</b>
<b>3.2. Introduction</b> .....	<b>19</b>
<b>3.3. Experimental Procedures</b> .....	<b>22</b>
ALD Process Development.....	22
Characterization.....	24
Electrochemistry.....	24
<b>3.4. Results and Discussion:</b> .....	<b>26</b>
Atomic Layer Deposition Process Parameters.....	26
Chemical Characterization by XPS .....	28
Conformality .....	33
Electrochemical Characterization .....	34
<b>3.5. Discussion</b> .....	<b>37</b>
<b>3.6. Conclusions</b> .....	<b>40</b>

<b>Chapter 4: Nanoscale Li, Na, and K Ion-Conducting Polyphosphazenes by Atomic Layer Deposition .....</b>	<b>42</b>
<b>4.1. Chapter Summary .....</b>	<b>42</b>
<b>4.2. Motivating Nanoscale Ion Conductors .....</b>	<b>42</b>
<b>4.3. Background .....</b>	<b>44</b>
ALD Solid Electrolytes .....	44
Polyphosphazenes.....	46
Lithium Phosphorous Oxynitride .....	47
Goal .....	48
<b>4.4. ALD Process Parameters .....</b>	<b>49</b>
<b>4.5. Chemical Structure.....</b>	<b>52</b>
<b>4.6. Understanding the Surface Reaction .....</b>	<b>56</b>
Mass spectra of LiOtBu.....	56
Surface Decomposition of LiOtBu.....	58
Mass Spectra of DEPA .....	59
Time-resolved Mass Spectra of LiPON Process. ....	61
<b>4.7. Proposed Reaction Mechanism.....</b>	<b>63</b>
<b>4.8. Electrochemistry.....</b>	<b>65</b>
<b>4.9. Discussion .....</b>	<b>68</b>
<b>4.10. Summary and Conclusions.....</b>	<b>71</b>
<b>Chapter 5: Nanoscale Sodium Solid-State Batteries Enabled by the Solid Electrolyte NaPON.....</b>	<b>74</b>
<b>5.1. Introduction .....</b>	<b>74</b>
<b>5.2. Experimental Procedures .....</b>	<b>75</b>
Fabrication.....	75
Electrochemistry.....	76
Characterization.....	76
<b>5.3. Electrochemical Analysis in Liquid Electrolyte .....</b>	<b>78</b>
<b>5.4. Solid-State Electrochemistry .....</b>	<b>81</b>
<b>5.5. Interfacial Characterization.....</b>	<b>86</b>
NaPON-V2O5 .....	86
Na-NaPON-V2O5 .....	94
<b>5.6. Discussion .....</b>	<b>96</b>
<b>5.7. Conclusions.....</b>	<b>100</b>
<b>Chapter 6: Conclusions and Future Work .....</b>	<b>102</b>
<b>6.1. Conclusions.....</b>	<b>102</b>
<b>6.2. Future Work.....</b>	<b>103</b>
<b>Bibliography.....</b>	<b>107</b>

# Chapter 1: Introduction

## **1.1. Motivation**

The efficient and sustainable storage of energy is of utmost importance to society and garners critical recognition from scientists and engineers. The storage of energy generated by renewable resources such as solar and wind power necessitates the use of high-performance batteries. Emerging sustainable technologies such as electric vehicles, autonomous sensor networks, biomedical devices, and wearable electronics also require advanced batteries. Lithium-ion batteries (LIBs) are the most widely used battery device today due to their higher energy density compared to currently available battery technologies.<sup>1, 2</sup> However, they raise safety concerns because of the flammability and reactivity of their organic liquid electrolytes, leading to possible short-circuiting and explosions in extreme cases. Solid-state batteries (SSB) can be a viable solution for energy storage based on their intrinsic safety advantages over LIBs. Solid-state electrolytes (SSE) alleviate the safety concern in all-SSBs and can help with increasing battery lifetime, lowering the overall systems cost while simultaneously increasing power-density.<sup>3</sup> Beyond the push to SSBs for safety considerations, SSBs based on materials of higher abundance offer both lower costs and prolonged societal sustainability. Sodium-ion batteries (SIBs) and potassium-ion batteries (KIBs) are attractive replacements for LIBs due to the small ionic size and mass of  $\text{Na}^+$  and  $\text{K}^+$  and their similar chemical/electrochemical with to  $\text{Li}^+$  charge storage behavior.<sup>4</sup>

## **1.1. Thin-Film Solid-State Batteries**

The main draw of SSBs is their inherent safety and stability, allowing their use in critical and diverse applications where flammable liquids must be avoided. Despite the attractiveness of

SSBs, obstacles preventing rapid commercialization remain such as low ionic conductivity in the SSE and high interfacial impedance with the electrolyte/electrode interface. Thin-film processing presents one method to alleviate these concerns, whereas thin layers (<100 nm) do not require high ionic conductivity comparable to liquid electrolyte (1 mS/cm) and can reduce interfacial impedance within the battery.<sup>5-9</sup> However, an underlying challenge in thin-film SSBs persists due to their planar configuration, limiting power densities and applications in small scale systems.

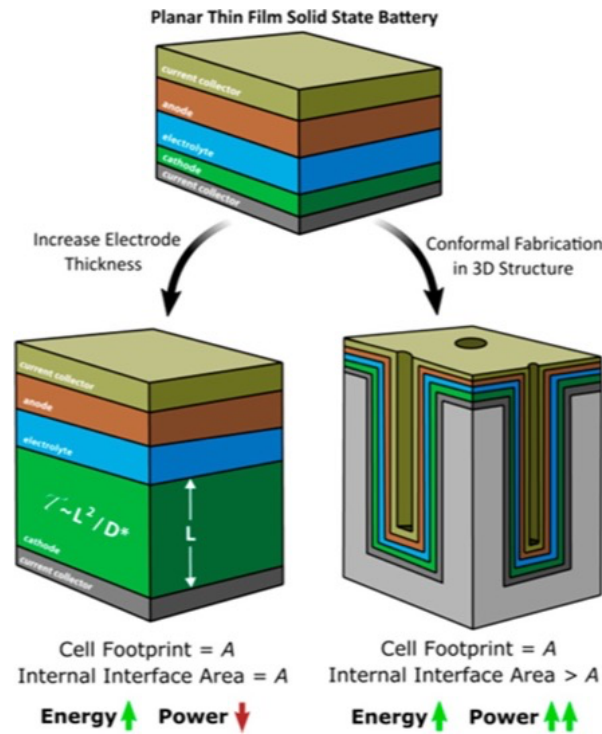


Figure 1.1. Decoupling of energy-power in thin-film SSBs. Increasing the electrode thickness increases energy density but sacrifices rate performance. 3D structuring provides a pathway to simultaneous enhancement in energy and power metrics. From Pearse et al., 2018.<sup>10</sup>

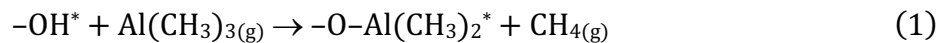
Methods to improve the energy and power density of thin-film SSBs are depicted in Figure 1.1. The planar nature of the conventional SSB requires a trade-off for energy or power, as electrode thickness increases energy density also increases, but leads to power losses as transport time scales with diffusion length. However, 3D structuring provides a pathway for decoupling the energy-power conundrum. The simultaneous improvement in energy and power of 3D SSBs is attributed

to the large increase of internal surface area in a given foot print area as a result of the 3D architecture.<sup>9-12</sup> The areal enhancement can be quantitatively defined by the area enhancement factor ( $AEF = A/A_f$ ), which represents the ratio of the internal surface area,  $A$ , to the footprint area,  $A_f$ , of the substrate. Realization of a conformal 3D SSB is complex and unreasonable for scaling to micro/nano form factors with traditional battery manufacturing techniques. Traditional processing of SSBs involves the milling and sintering of powder precursors (binders, salts, conductive additives), requiring thick layers, and limiting use in small-scale applications. Standard thin-film battery processing techniques such as sputtering produce high-quality films at the nanoscale but fail in attempts of maintaining conformality for 3D devices.<sup>13</sup> Alternative vapor phase processing methods such as chemical vapor deposition (CVD) and atomic layer deposition (ALD) opens the doorway for achieving 3D SSBs, providing conformal deposition of each battery component over a high aspect ratio template. Both techniques are already industry standards for complementary metal oxide semiconductor (CMOS) processing. 3D conformal SSBs not only enhance battery performance but provide a means to merge energy storage capability with on-chip Si manufacturing. This opens the door for next-generation micro/nano-electronic devices for applications in but not limited to smart sensors and implantable medical devices.

## **1.2. Atomic Layer Deposition**

ALD is a powerful technique for thin-film deposition, gaining its fame in the miniaturization of semiconductor processing. More recently, ALD has emerged as the predominant technique for surface and interface engineering in batteries and other energy storage applications due to its ability to deposit high-purity conformal films at the nanoscale.<sup>14-17</sup> The essence of ALD is its utilization of self-limiting and sequential surface reactions. In an ideal ALD process, the growth of the film is independent of precursor exposure time, which is in contradiction to other

vapor phase processing techniques. Physical vapor deposition growth rate can be described as line-of-sight deposition, meaning growth proceeds with exposure of the reactive source (e.g. sputtering target or evaporation crucible). In CVD, the growth rate is directly related to exposure time, as the precursors react in the gas phase and then adsorb on the surface. ALD utilizes alternating precursor pulse/purge sequences (*pulse A–purge–pulse B–purge*)<sub>x</sub> sequences, so that A and B precursor molecules do not meet in the gas phase, therefore all the reactions take place on the surface and excess reactants are purged away before introduction of the next precursor. The quintessential ALD process is the thermal growth of Al<sub>2</sub>O<sub>3</sub> using trimethyl aluminum (TMA) and H<sub>2</sub>O as precursors. The half reactions for the TMA-H<sub>2</sub>O ALD process on an OH terminated surface are described by equations 1 and 2 below, where \* indicates a surface species.<sup>18</sup>



The self-limiting nature of ALD provides the ability to coat pinhole free films on complex porous and 3D structures, key hallmarks of ALD. This makes it an attractive means of fabrication for SSBs as well as many other applications.

ALD protective coatings, namely metal oxides, have been extremely successful in improving and stabilizing battery materials.<sup>5, 6, 19</sup> Direct coating of anodes and cathodes have proven the capability to mitigate undesired reactions with liquid electrolytes and promote a stable solid electrolyte interphase (SEI) layer. These coatings have also demonstrated the ability to dramatically reduce interfacial impedance and reactivity between SSE/electrodes.<sup>20</sup> Stand-alone ALD fabricated thin-film SSEs and electrode materials have also been demonstrated. TiO<sub>2</sub> and SnO<sub>2</sub> are the most widely used ALD anodes.<sup>21, 22</sup> On the cathode side, V<sub>2</sub>O<sub>5</sub> has been the most heavily researched ALD cathode material, due to its straightforward processing and as-deposited

crystalline morphology.<sup>23</sup> ALD processes exist for conventional battery cathodes with higher voltage and capacity such as  $\text{LiCoO}_2$ <sup>24</sup> or  $\text{LiMnO}_4$ <sup>25</sup>, however, such ALD processes are undesirable and require multiple super-cycles of ALD processes and high temperature annealing. The most successful ALD SSEs are amorphous glass films such as lithium borates, phosphates, or silicates, which achieve ionic conductivities in the  $10^{-6}$  S/cm range.<sup>20</sup>

### 1.3. Lithium Phosphorus Oxynitride

Lithium phosphorus oxynitride (LiPON) is currently the premier thin-film SSE. First pioneered by Bates and Dudney<sup>26,27</sup> at Oak Ridge National Laboratory via sputtering in the 1990s, LiPON has since enabled thin-film SSBs and shown excellent stability with Li metal.<sup>28</sup>

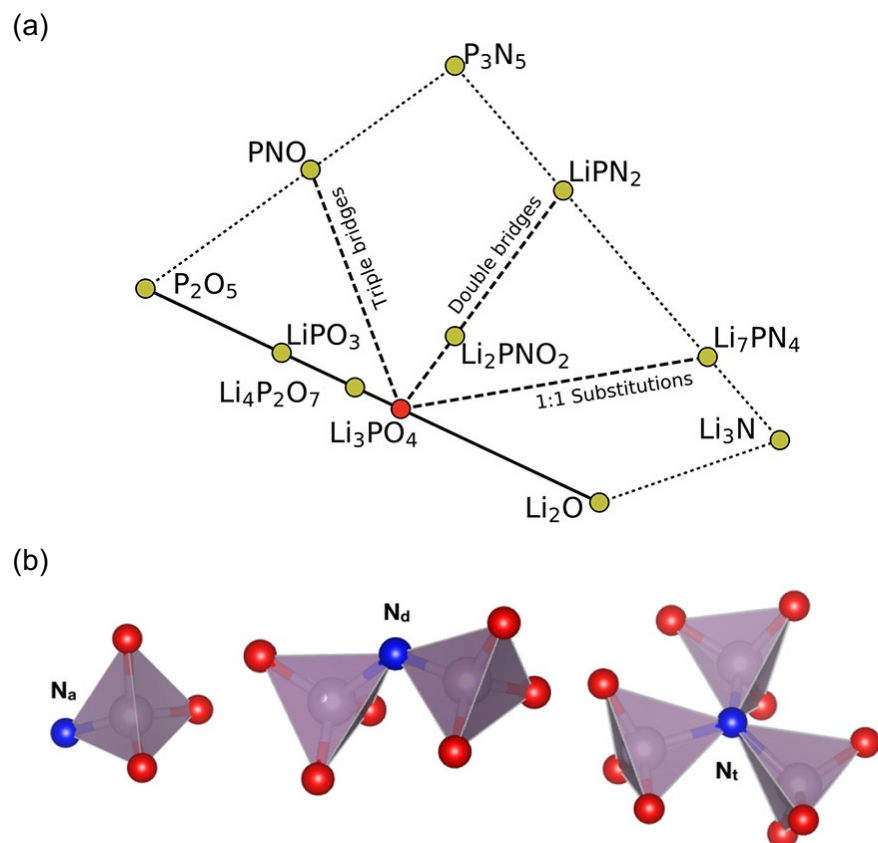


Figure 1.2. (a) Phase diagram showing LiPON compositions in the  $\text{Li}_x\text{PO}_y\text{N}_z$  space. (b) Possible N binding environments in LiPON structures.  $N_a$  is apical N,  $N_d$  is doubly coordinated N,  $N_t$  is triply coordinated N. Color code: N (blue), O (red), P (gray). From Lacivita et al. 2018.<sup>29</sup>

LiPON normally adopts an amorphous glass structure, based on a  $\text{LiPO}_3$  base metaphosphate structure with nitrogen doping, existing in a doubly ( $\text{N}_d$ , P-N=P) or triply ( $\text{N}_t$ , P-N<P) coordinated environment. Lacivita et al.<sup>30</sup> recently suggested the adoption of a singly coordinated, or apical nitrogen ( $\text{N}_a$ , P-N) in LiPON. As a result of different nitrogen bridging configurations, multiple polymorphs of LiPON exist within the broader  $\text{Li}_x\text{PO}_y\text{N}_z$  system as shown in the phase diagram in Figure 1.2a. The three coordination types of N with the phosphate unit are depicted in Figure 1.2b. The N coordination state and the overall degree of nitridation is one of the most important parameters effecting the ionic conductivity of the SSE, with more N resulting in a higher ionic conductivity due to decreased electrostatic interactions of P-O and replacement with a more covalent P-N bond.<sup>31, 32</sup>

Several ALD processes of LiPON have since been developed, with varying stoichiometries of  $\text{Li}_x\text{PO}_y\text{N}_z$ .<sup>33-36</sup> Kozen et al.<sup>36</sup> developed the first plasma-enhanced ALD LiPON process using four precursors to grow the film. The process incorporated the thermal growth of the  $\text{Li}_3\text{PO}_4$  through lithium *tert*-butoxide ( $\text{LiO}^t\text{Bu}$ ),  $\text{H}_2\text{O}$ , and trimethyl phosphate, with nitridation through an added  $\text{N}_2$  plasma exposure step. Pearse et al.<sup>35</sup> built upon this work and others to develop a two-step thermal ALD process using  $\text{LiO}^t\text{Bu}$  and diehtylphosphoramidate (DEPA) as precursors. The subsequent film is more precisely described as a lithium polyphosphazene<sup>37, 38</sup>, due to the overall stoichiometry of  $\text{Li}_2\text{PO}_2\text{NC}$ . The N/P of 1 implies a complete substitution of the bridging oxygen (P-O-P) with P-N-P bonds in the backbone of the oxynitride structure, however significant carbon content of the films implies significant remaining methyl ligands in the films. Such complete backbone nitridation was not able to be achieved in other ALD LiPON or sputtering processes, making this particular polymorph of LiPON highly desirable, and is attributed to the P-N bond preformed in the DEPA precursor. In this dissertation, the ALD processes of sodium phosphorus

oxynitride (NaPON) and potassium phosphorus oxynitride (KPON) are explored using their respective alkali *tert*-butoxide and DEPA as precursors for next generation SSEs.

## 1.2. Beyond Lithium Solid-State Batteries

Lithium-based energy storage has made great strides in moving away from fossil-fuel energy sources and combating climate change. LIBs have been successful in part to the light weight and high electropositivity of Li, meaning Li loses electrons to form  $\text{Li}^+$  very easily to produce energy, and which can be transported relatively quickly due to its low mass. It is clear batteries are crucial for the energy storage landscape of the future, but with this in mind it is prudent to develop battery chemistries centered around an ion charge carrier of higher abundance. Figure 1.3a depicts the abundance of elements relevant to batteries in the earth's crust. Excluding oxygen, sodium is the 5<sup>th</sup> most and potassium the 7<sup>th</sup> most abundant elements in the earth's crust, making them attractive alkali metals to replace lithium. Figure 1.3b shows the current distribution of lithium

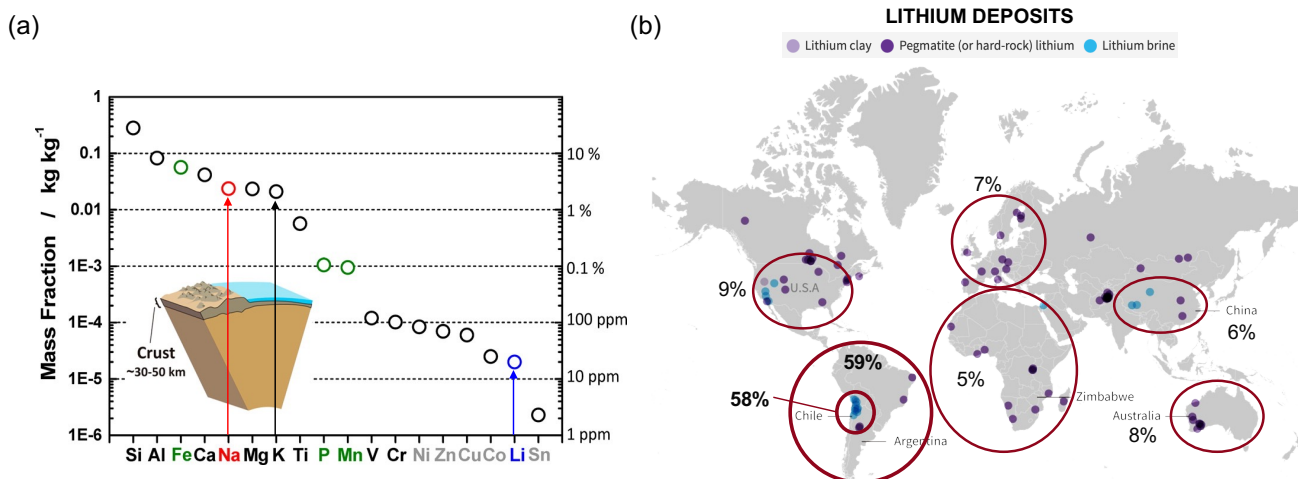


Figure 1.3. (a) Elemental abundance in the Earth's crust. From Yabuuchi et al. 2014.<sup>4</sup> (b) Distribution of lithium reserves in the world. From Reuters. <https://graphics.reuters.com/ELECTRIC-VEHICLES-METALS/010092JB38P/index.html>.

resources in the world according to the 2021 Mineral Commodity Summaries by the United States Geological Survey.<sup>39</sup> Not only are lithium resources limited, but they are also unevenly distributed throughout the world. An overwhelmingly majority of lithium reserves are all in South America (59%), with Chile dominating this contribution, possessing 58% of the total lithium resources in the world.

Similar alkali metals to Li such as Na and K are attractive replacements due to their similar properties to Li. Comparison of physical properties as well as price of raw materials for Li, Na, and K are shown in Table 1.1. Despite the larger mass and ionic radius of Na and K than Li, they have a similar reduction potential providing reasonable electrochemical energy production and are a fraction of the cost of Li. Of the two alkali-ions, Na is the more likely replacement for Li due to its smaller size and similar intercalation mechanism in electrode materials with Li.<sup>4</sup> Historically, Na<sup>+</sup> as a charge carrier for electrochemical energy storage was studied alongside the early reports

*Table 1.1. Comparison of Physical Properties and Cost of Alkali Metals.*

	Li <sup>+</sup>	Na <sup>+</sup>	K <sup>+</sup>
<b>Relative Atomic Mass</b>	6.94	23	39.1
<b>Ionic Radii (Å)</b>	0.76	1.02	1.38
<b>E° vs SHE (V)</b>	-3.04	-2.71	-2.93
<b>Minerals Cost (\$/kg)</b>	8	0.5	0.9

of Li<sup>+</sup> insertion into TiS<sub>2</sub> that was reported in the 1970s.<sup>40-43</sup> However, LIB research picked up due to its higher energy density and has since dominated the market. Since 2010, research efforts on SIBs has skyrocketed, and is now a hot topic with commercialization of SIBs in sight. Contemporary Ampere Technology Co., Limited (CATL), a global leader in lithium-ion batteries, unveiled their first SIB in 2021 and plans to begin production in 2023. Additionally, the UK-based

start-up Faradion is developing SIBs and showing promise, as it was purchased in 2022 for \$135 million by the Indian corporation Reliance Industries. The excitement and potential of SIBs position the ALD fabricated NaPON SSE invented in this dissertation to be highly sought after in SSBs or as a protection layer in liquid-electrolyte SIBs.

### **1.3. Review of Solid-State Sodium-Ion Conductors**

An ideal solid electrolyte should possess the following properties: (1) high ionic conductivity, (2) high thermal stability, (3) chemical stability with electrode materials, (4) wide voltage window, and (5) low cost.<sup>3</sup> Typical SSEs employed to meet these criteria include inorganic, polymer, and thin-film materials. A summary of solid Na<sup>+</sup> conductors is shown in Table 1, in which ceramic type materials are the most prevalent. Sodium superionic conductor or NASICON-type (Na<sub>1+x</sub>Zr<sub>2</sub>P<sub>3-x</sub>Si<sub>x</sub>O<sub>12</sub>)<sup>44</sup> crystalline electrolytes are also of interest due to their high room temperature ionic conductivity (~10<sup>-4</sup> S/cm). Despite their high conductivities, β''-Al<sub>2</sub>O<sub>3</sub> and NASICON have major drawbacks for practical applications, such as need for high temperature sintering and prevalence of poor electrode-electrolyte contact.<sup>45, 46</sup> Recently, glass-ceramic SSEs such as thiophosphates (Na<sub>3</sub>PS<sub>4</sub>) and sulfide glasses have been considered a promising alternative. Na<sub>3</sub>PS<sub>4</sub>-based glass-ceramic electrolytes<sup>47-51</sup> have demonstrated an ionic conductivity up to 10<sup>-3</sup> S/cm at room temperature, which rivals that of organic liquid electrolytes. However, the thickness of such SSEs is quite large (~1-2 mm) as a result of the powder processing technique, which further limits SIB performance. There has been little efforts in thin-film SSEs, with the thinnest SIB being enabled by a polymer electrolyte<sup>52</sup> (100-200 μm), but its thickness and polymeric structure prevent direct comparison to an inorganic thin-film SSE. The only prior demonstration of thin-film solid Na<sup>+</sup> conductors were deposited by magnetron RF sputtering<sup>53-55</sup>, which require relatively large thicknesses (>500 nm) and are not compatible with 3D high-aspect-ratio structures. For the

realization of next-generation SIBs, further research attention is required on the development of thin-film Na-ion conductors.

Table 1.2. Summary of Solid-State Sodium-Ion Conductors.

Material	Ionic Conductivity (S/cm)	Activation Energy (eV)	Measured Temperature (°C)	Thickness (nm)	Reference
<b>Thin Film</b>					
ALD-NaPON	$1.0 \times 10^{-7}$	0.53	25	$1.1 \times 10^2$	56
RF Sputtered-NaPON	$8.7 \times 10^{-6}$	0.16	27	$1.2 \times 10^3$	55
NASICON ( $\text{Na}_3\text{Zr}_2\text{Si}_2\text{PO}_{12}$ )	$3.1 \times 10^{-5}$	-	25	$1.0 \times 10^3$	54
NASICON ( $\text{Na}_3\text{Zr}_2\text{Si}_2\text{PO}_{12}$ )	0.29 (annealed 700 °C 1h)	0.55	200	$2.0\text{-}2.5 \times 10^3$	53
<b>Ceramic</b>					
NASICON ( $\text{Na}_3\text{Zr}_2\text{Si}_2\text{PO}_{12}$ )	$6.7 \times 10^{-4}$	0.35	25	$1.0 \times 10^6$	57
NASICON ( $\text{Na}_{3.3}\text{Zr}_{1.7}\text{La}_{0.3}\text{Si}_2\text{PO}_{12}$ )	$3.4 \times 10^{-3}$	0.29	25	$1.0 \times 10^6$	57
Polycrystalline $\beta''\text{-Al}_2\text{O}_3$	$1.2 \times 10^{-3}$	0.27	-	-	58
Single crystal $\beta''\text{-Al}_2\text{O}_3$	$4.0 \times 10^{-2}$	0.22	-	-	59
<b>Sulfide Glass-Ceramic</b>					
c- $\text{Na}_3\text{PS}_4$	$2.0 \times 10^{-4}$	0.28	25	$1.0\text{-}1.5 \times 10^6$	47
$\text{Na}_{10}\text{SnP}_2\text{S}_{12}$	$4.0 \times 10^{-4}$	0.36	25	$7.5 \times 10^5$	60
$\text{Na}_{3.1}\text{Sn}_{0.1}\text{P}_{0.9}\text{S}_4$	$2.5 \times 10^{-4}$	0.18	25	-	61
$\text{Na}_{3.1}\text{Ge}_{0.1}\text{P}_{0.9}\text{S}_4$	$2.1 \times 10^{-4}$	0.21	25	-	61
$\text{Na}_{3.1}\text{Ti}_{0.1}\text{P}_{0.9}\text{S}_4$	$2.3 \times 10^{-4}$	0.20	25	-	61
$\text{Na}_3\text{P}_{0.62}\text{As}_{0.38}\text{S}_4$	$1.5 \times 10^{-3}$	0.26	25	$0.6\text{-}1.2 \times 10^6$	62
t- $\text{Na}_3\text{PS}_4$	$1.0 \times 10^{-6}$	0.42	30	$1.0\text{-}2.0 \times 10^6$	63
t- $\text{Na}_3\text{PS}_4$ ( $\text{Na}_{2.9375}\text{PS}_{3.9375}\text{Cl}_{0.0625}$ )	$1.1 \times 10^{-3}$	0.25	30	-	48
$0.75\text{Na}_2\text{S} \cdot 0.25\text{P}_2\text{S}_5$	$2.0 \times 10^{-4}$	0.28	25	$1.0\text{-}1.5 \times 10^6$	64
$94\text{Na}_3\text{PS}_4 \cdot 6\text{Na}_4\text{Si}_4$	$7.4 \times 10^{-4}$	0.25	25	$1.0\text{-}1.5 \times 10^6$	65
$75\text{c-}\text{Na}_3\text{PS}_4 \cdot 25\text{NaI}$	$1.0 \times 10^{-4}$	-	25	$1.5 \times 10^6$	66
<b>Other Na Superionic Conductors</b>					
$\text{Na}_3\text{SbS}_4$	$1.1 \times 10^{-3}$	0.20	25	-	49
$\text{Na}_3\text{PSe}_4$	$1.2 \times 10^{-3}$	0.21	25	-	67
<b>Closo-borates</b>					
$\text{Na}_3\text{BH}_4\text{B}_{12}\text{H}_{12}$	$5.0 \times 10^{-4}$	0.34	25	$1.5 \times 10^6$	68
$\text{Na}_2(\text{B}_{12}\text{H}_{12})_{0.5}(\text{B}_{10}\text{H}_{10})_{0.5}$	$9.0 \times 10^{-4}$	0.40	20	$1.0\text{-}2.0 \times 10^6$	69
$\text{Na}_2\text{B}_{10}\text{H}_{10}\text{-Na}_2\text{B}_{12}\text{H}_{12}$	$3.2 \times 10^{-4}$	0.56			70
<b>Antiperovskite</b>					
$\text{Na}_{2.9}\text{Sr}_{0.05}\text{OBr}_{0.6}\text{I}_{0.4}$	$4.5 \times 10^{-5}$	0.62	100	$1.0 \times 10^5$	71
$\text{Na}_3\text{OBr}_{0.6}\text{I}_{0.4}$	$1.0 \times 10^{-5}$	0.63	100	$1.0 \times 10^5$	71
$\text{Na}_3\text{OBr}$	$5.6 \times 10^{-7}$	0.76	100	$1.0 \times 10^5$	71
<b>Plastic Crystal</b>					
Succinonitrile- $\text{NaClO}_4$	$3.3 \times 10^{-3}$	-	-	-	72
<b>Polymer</b>					
PEO- $\text{NaClO}_4$	$1.5 \times 10^{-5}$	-	30	$1.8 \times 10^5$	73

TiO <sub>2</sub> -nanocomposite PEO-NaClO <sub>4</sub>	$2.0 \times 10^{-5}$	-	30	$1.8 \times 10^5$	<sup>73</sup>
PEO-NaAsF <sub>6</sub>	$2.5 \times 10^{-6}$	0.46	25	$5.0 \times 10^5$	<sup>74</sup>
<b>Liquid</b>					
1M NaClO <sub>4</sub> EC:PC	$3.3 \times 10^{-3}$	-	25	-	<sup>75</sup>

## 1.4. Dissertation Overview

In this dissertation novel alkali SSEs are synthesized by ALD and characterized for incorporation in nanoscale beyond-lithium SSBs. In Chapter III, the development the first ALD-fabricated Na<sup>+</sup> conductor, NaPON, is presented as a SSE for nanoscale Na-SSBs. In chapter IV, a holistic review of the thermal LiPON and NaPON ALD process are presented, in addition to new results the first ALD-fabricated K<sup>+</sup> conductor, KPON. The ALD process parameters, chemical structure, reaction mechanism, and electrochemical properties are discussed for each APON (A = Li, Na, K) SSE. In chapter V, NaPON is incorporated as a SSE with a V<sub>2</sub>O<sub>5</sub> cathode and Na metal anode for demonstration of the first nanoscale Na-SSB. NaPON is also implemented with V<sub>2</sub>O<sub>5</sub> in liquid-electrolyte batteries for comparison.

## Chapter 2: Experimental Techniques

### 2.1. Atomic Layer Deposition Nanostructures Laboratory (ANSLab)

ANSLab is a state of the art highly customized laboratory for synthesizing, characterizing, and electrochemically testing air-sensitive materials, specifically those relevant to SSBs and microelectronics. A suite of thin-film deposition chambers, surface analysis instrumentation, and an Ar-filled glovebox are coupled through an ultra-high vacuum (UHV) integrated system. A schematic of the ANSLab equipment is shown in Figure 2.1. The ANSLab instrumentation houses two Veeco Fiji F200 ALD reactors nicknamed “Mario” and “Luigi”. Luigi is connected through a UHV load-lock to an Ar glovebox. Mario is UHV coupled directly to the central Kurt J. Lesker RTTA radial transfer chamber, which is connected to 4 other UHV chambers via 8” pneumatic gate valves. Other than Mario, the RTTA chamber connects to a custom thermal evaporator/load-

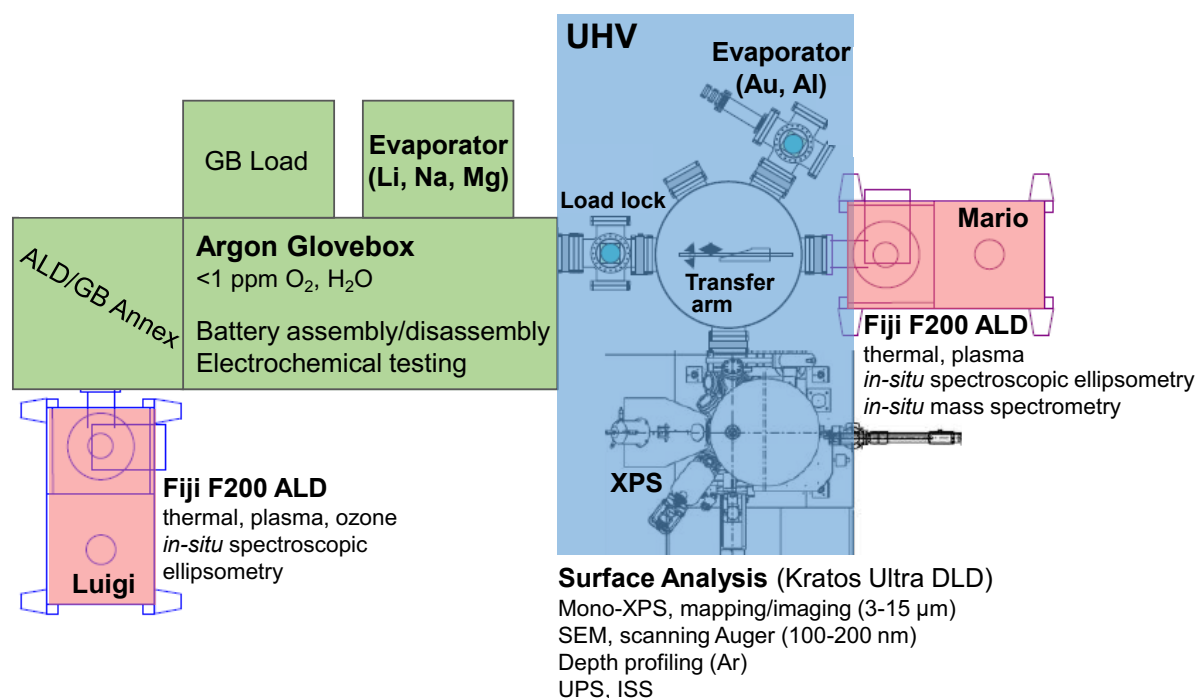


Figure 2.1. Schematic of ANSLab equipment used to fabricate, characterize, and evaluate materials in this dissertation.

lock chamber, a load-lock chamber capable of venting to Ar atmosphere for glovebox sample transfer, and a Kratos Ultra DLD surface analysis system. The RTTA chamber is considered the workhorse of the ANSLab integrated system. The RTTA chamber contains a robotic transfer arm allowing for transfer of 3'' Si wafers or 3'' custom stainless-steel sample holders between chambers. The MBraun Labmaster Ar glovebox is another key feature of ANSLab. The glovebox allows for sample preparation/storage, electrical feedthroughs to an external Biologic VSP potentiostat for electrochemical testing, inert transferring to the UHV integrated system, and is directly coupled to a custom thermal evaporator through an 8'' conflat port used for Li, Na, and Mg metal evaporation. The glovebox-integrated thermal evaporator is used for thin-film Na metal evaporation in this dissertation, providing a cleaner alternative to Na foil used in most battery experiments. The ANSLab setup is unprecedented for an academic laboratory, allowing for ultra-clean experimental studies without perturbation for highly sensitive materials such as alkali ionic materials and SSBs.

## **2.2. Atomic Layer Deposition**

ALD is the primary deposition method used in this dissertation as it is capable of growing ultra-high purity films with angstrom level tunable thickness. The characteristics of ALD and their applications in battery systems are described in Chapter 1. ALD is used to grow LiPON, NaPON, and KPON solid electrolytes, as well as  $V_2O_5$  cathodes. The Mario ALD reactor in ANSLab (Figure 2.2) is used to fabricate APON films ( $A = \text{Li, Na, K}$ ), providing *in-operando* characterization of the ALD processes. Mario has *in-operando* spectroscopic ellipsometry and mass spectrometry capabilities that are used for optimization of process parameters and identification of chemical species during the process for insight into the reaction mechanism of the ALD process. *In-vacuo* coupling to the Kratos surface analysis system allows for pristine film

characterization through X-ray photoelectron spectroscopy (XPS). A Beneq TFS 500 ALD reactor in the Maryland Nanocenter FabLab was used for deposition of  $V_2O_5$  cathodes.

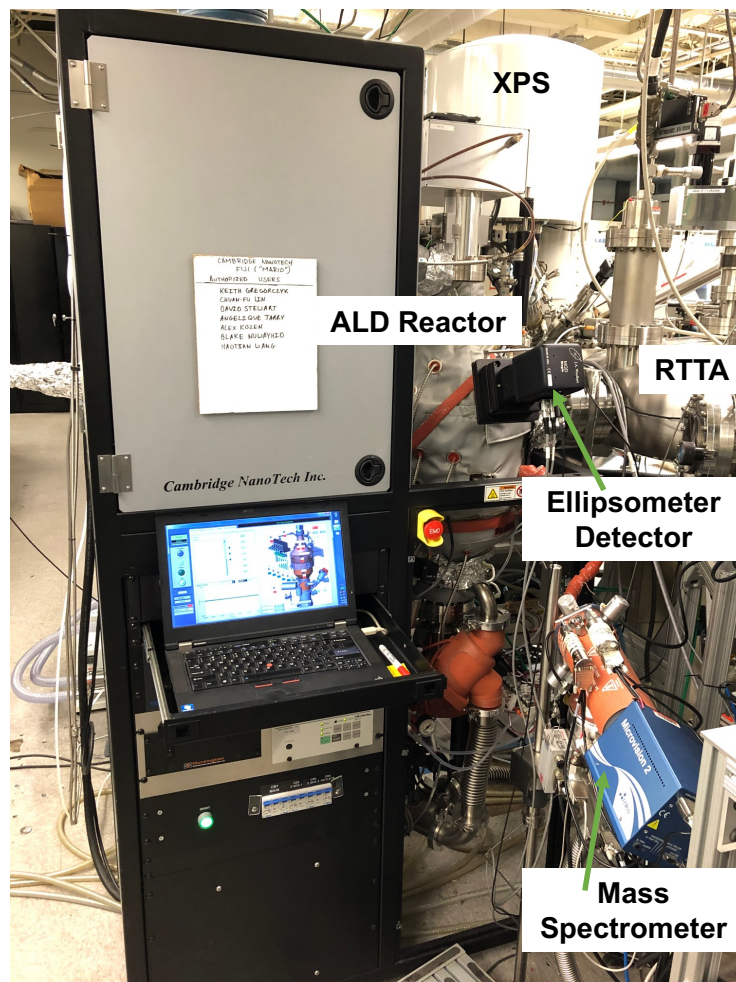


Figure 2.2. Fiji-F200 ALD Reactor (Mario) in ANSLab. Mario is equipped with in-line mass spectrometry sampling and in-operando spectroscopic ellipsometry. ALD films can be transferred directly to a surface analysis system for XPS through the RTTA UHV transfer chamber.

### 2.3. X-ray Photoelectron Spectroscopy

XPS is the primary chemical characterization technique used in this dissertation to understand the chemical structure of novel APON films. XPS is a highly surface-sensitive spectroscopy technique, making it ideal for understanding the chemical composition of thin-film

materials. The fundamental operation of XPS is based on the photoelectric effect<sup>76</sup> (Nobel Prize, 1922, Einstein), in which spectra are obtained by irradiating the sample with X-rays and detecting the kinetic energy of electrons that are emitted from the top ~10 nm of the surface. The electron binding energy of emitted electrons can then be determined by the conservation of energy equation below,

$$E_{binding} = h\nu - (E_{kinetic} + \phi) \quad (1)$$

where  $E_{binding}$  is the binding energy of the excited electron,  $h\nu$  is the photon energy,  $E_{kinetic}$  is the kinetic energy of the excited electron, and  $\phi$  is the work function of the material. In actual lab measurements, the work function term is an instrumental correction factor that includes the spectrometer's work function and a surface potential term. The binding energy not only provides information to the elemental species present, but also the oxidation state and binding environment of the atom. From this information, the overall stoichiometry of materials are determined and the types of bonds can be inferred for structure determination.

XPS measurements were conducted in the Kratos surface analysis system in ANSLab shown in Figure 2.3. ALD films were transferred directly from the reactor to the XPS system under UHV conditions for characterization of the pristine film. Such APON films are extremely air sensitive, necessitating characterization without air-exposure to accurately characterize the materials composition.

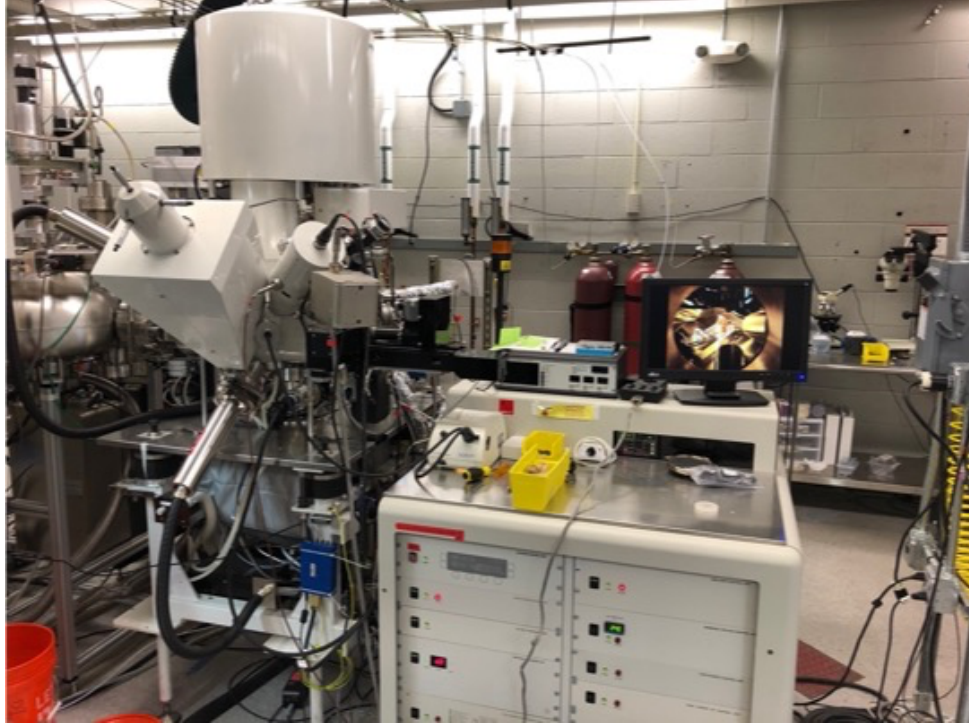


Figure 2.3. Kratos Ultra DLD surface analysis system in ANSLab used for XPS measurements.

## 2.4. Spectroscopic Ellipsometry

The ALD process development in this dissertation relies heavily on *in-operando* spectroscopic ellipsometry. This is crucial for determining the optimal precursor pulse and purge times for film growth. The raw SE data measures the change of polarization as light interacts with the sample surface, which is correlated to the film thickness through an optical model.<sup>77</sup> The polarization is described by the equation below,

$$\tilde{p} = \frac{\tilde{r}_p}{\tilde{r}_s} = \frac{|\tilde{r}_p|}{|\tilde{r}_s|} e^{i(\delta_p - \delta_s)} = \tan \Psi e^{i\Delta} \quad (2)$$

where  $r_p$  and  $r_s$  are the Fresnel reflection coefficients for the p- and s- polarized light, respectively. The amplitude ratio ( $\Psi$ ) and phase difference ( $\Delta$ ) are measured dynamically across the spectral range (200-2000 nm) throughout the deposition process and are correlated to film thickness

through optical models. A J.A. Woollam M-2000D spectroscopic ellipsometer was used for *in-operando* and *ex-situ* measurements of samples in this thesis. The optical models for the ALD materials described in this thesis were developed in collaboration with Greg Pribil at J.A. Woollam Company.

## 2.5. Electrochemical Analysis

Electrochemical testing is key for evaluating the properties of new SSE materials as well as battery performance. A Biologic VSP potentiostat (Figure 2.4) was used for all electrochemical tests in both solid-state and liquid-electrolyte coin-cell configurations. Electrochemical tests include electrochemical impedance spectroscopy (EIS), cyclic voltammetry (CV), and galvanostatic battery cycling measurements. Figure 2.4b shows an image of a NaPON SSE undergoing electrochemical testing on a custom probe station inside the Ar glovebox. It is critical to evaluate such SSEs in the glovebox to avoid air-exposure for precise determination of electrochemical properties, which is evidenced in chapter 3 and 4.

(a)



(b)

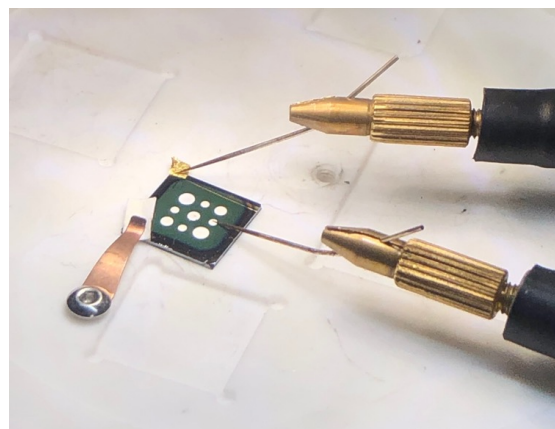


Figure 2.4. (a) BioLogic VSP potentiostat used for EIS, CV, and battery cycling measurements. (b) Electrochemical testing of a NaPON SSE with micro-manipulator probes inside an Ar glovebox.

A majority of this dissertation involved SSE synthesis and characterization, in which the ionic conductivity and activation energy are key parameters for evaluation. Electrochemical impedance spectroscopy (EIS) is used to probe these ionic transport parameters by depositing the SSE between inert metal contacts such as Pt or Au. In the EIS measurement, an alternating current potential is applied to the electrochemical cell at different frequencies and monitoring the current through the cell. The impedance is represented as a function of frequency containing a real and imaginary part,

$$Z(\omega) = \frac{E}{I} = Z_o \exp(i\varphi) = Z_o(\cos\varphi + i\sin\varphi) \quad (3)$$

where  $Z$  is the impedance,  $\omega$  is the frequency,  $E$  is the voltage,  $I$  is the current,  $Z_o$  is the magnitude, and  $\varphi$  is the phase shift.<sup>78</sup> This data is represented in a Nyquist diagram, which plots the imaginary part of the impedance vs. the real part of the impedance. An equivalent circuit model is used to fit the Nyquist plot to determine the total resistance, from which ionic conductivity and resistance are determined.

The voltage stability is also an important parameter in solid electrolytes, which can be investigated using cyclic voltammetry (CV). In CV, the potential of the working electrode is increased at a constant rate up to a set voltage, then the potential is reversed in the opposite direction to a lower potential.<sup>78</sup> In performing CV measurements on solid electrolytes, a two electrode setup consisting of a Na metal reversible electrode and inert metal blocking electrode are used, e.g. Na/NaPON/Pt.

# Chapter 3: Atomic Layer Deposition of Sodium Phosphorus Oxynitride: A Conformal Solid-State Sodium-Ion Conductor

## 3.1. Chapter Summary

The development of novel materials that are compatible with nanostructured architectures is required to meet the demands of next-generation energy storage technologies. Atomic layer deposition (ALD) allows for the precise synthesis of new materials that can conformally coat complex 3D structures. In this work, we demonstrate a thermal ALD process for sodium phosphorus oxynitride (NaPON), a thin-film solid-state electrolyte (SSE) for sodium-ion batteries (SIBs). NaPON is analogous to the commonly used lithium phosphorus oxynitride SSE in lithium-ion batteries. The ALD process produces a conformal film with a stoichiometry of  $\text{Na}_4\text{PO}_3\text{N}$ , corresponding to a sodium polyphosphazene structure. The electrochemical properties of NaPON are characterized to evaluate its potential in SIBs. The NaPON film exhibited a high ionic conductivity of  $1.0 \times 10^{-7}$  S/cm at 25 °C and up to  $2.5 \times 10^{-6}$  S/cm at 80°C, with an activation energy of 0.53 eV. In addition, the ionic conductivity is comparable and even higher than the ionic conductivities of ALD fabricated  $\text{Li}^+$  conductors. This promising result makes NaPON a viable SSE or passivation layer in solid-state SIBs.

## 3.2. Introduction

The utilization of rechargeable energy storage is essential for the adoption of next generation renewable systems. In particular, rechargeable lithium-ion batteries (LIBs) are already ubiquitous in modern society, used in everything from cell phones to cars. Despite their diverse application and broad adoption, especially in portable electronics, LIBs still present major challenges related to health, safety, and sustainability. With few exceptions, LIBs use flammable

liquid electrolytes which generate toxic by-products such as HF gas when they fail. For these reasons there has been a significant push to move away from liquid electrolyte systems toward solid-state electrolytes (SSEs).<sup>1-3</sup> In addition, it is impracticable to continue consumption of lithium resources at current rates as it is non-abundant and non-uniformly spread in the Earth's crust.<sup>79</sup> The replacement of the lithium ion charge carrier with materials of higher abundance has garnered significant interest in the energy storage community. Sodium is a promising candidate due to its similarities in chemical behavior to lithium and its vast abundance.<sup>4, 80</sup>

Sodium-ion batteries (SIBs) were initially explored in the 1980s alongside LIBs<sup>41, 81, 82</sup>, but focus shifted towards LIBs due to their higher energy density and early success. The energy storage mechanism of SIBs and LIBs are essentially the same, owing to their very similar intercalation chemistry, differing only in the charge carrier.<sup>4, 80, 83</sup> From a resource perspective, the desirability of SIBs is clear. Sodium is the fifth most abundant element and is distributed all over the Earth. Raw sodium materials ( $\text{Na}_2\text{CO}_3$ ) required to produce SIBs are much cheaper (~26x) than the raw lithium materials ( $\text{Li}_2\text{CO}_3$ ) used to make LIBs. A 2018 cost analysis by Vaalma *et al.*<sup>84</sup> calculated a \$0.5/kg price for battery-grade (99.5%)  $\text{Na}_2\text{CO}_3$ , whereas the 2019 cost for battery-grade  $\text{Li}_2\text{CO}_3$  was \$13/kg according to the 2020 Mineral Commodity Summaries by The United States Geological Survey.<sup>85</sup> Despite the abundance of sodium, SIBs have remained in their infancy due to difficulties caused by the larger ion size, higher reactivity, and lower energy density.<sup>80, 83</sup> The adoption of SIBs configured in a similar manner to current LIBs (Carbon/ $\text{NaClO}_4$ -PC/ $\text{Na}_x\text{CoO}_2$ ) have the same underlying issues, except the safety concern is magnified due to the higher reactivity of sodium with the organic electrolyte.

Further adoption of SIBs, therefore, will require a solid electrolyte to alleviate such hazards. The only commercialized sodium-based systems are high temperature solid-state batteries

(SSBs) for grid storage, which utilize a molten sodium anode and a  $\beta$ -alumina ( $\beta''$ -Al<sub>2</sub>O<sub>3</sub>) ceramic electrolyte. Na superionic conductor or NASICON-type (Na<sub>1+x</sub>Zr<sub>2</sub>P<sub>3-x</sub>Si<sub>x</sub>O<sub>12</sub>)<sup>44</sup> crystalline electrolytes are also of interest due to their high room temperature ionic conductivity ( $\sim 10^{-4}$  S/cm). However,  $\beta''$ -Al<sub>2</sub>O<sub>3</sub> and NASICON have major drawbacks for practical applications, such as need for high temperature sintering and prevalence of poor electrode-electrolyte contact.<sup>45, 46</sup> Recently, glass-ceramic SSEs such as thiophosphates (Na<sub>3</sub>PS<sub>4</sub>) and sulfide glasses have been considered a promising alternative. Na<sub>3</sub>PS<sub>4</sub>-based glass-ceramic electrolytes<sup>47-51</sup> have demonstrated an ionic conductivity up to  $10^{-3}$  S/cm at room temperature, which rivals that of organic liquid electrolytes. However, the thickness of such SSEs is quite large ( $\sim 1$ -2 mm), which limits SIB performance. A polymer electrolyte film<sup>52</sup> (100-200  $\mu$ m) was shown to enable a solid-state SIB but its thickness and organic nature prevent direct comparison to an inorganic thin-film SSE. Additionally, the only demonstration of thin-film solid Na<sup>+</sup> conductors were deposited by magnetron RF sputtering<sup>53-55</sup>, which require large thicknesses ( $>1000$  nm) and are not compatible with 3D high-aspect-ratio structures. For the realization of next-generation SIBs, further research attention is required on the development of thin-film Na-ion conductors.

Conformal thin film coatings, namely by chemical vapor deposition (CVD) and atomic layer deposition (ALD), have proven to be extremely successful in improving interfacial stability and longevity in LIBs<sup>5-7, 19</sup>, but have more recently been explored in SIBs.<sup>21, 86-89</sup> Thin film SSBs have advantageous qualities such as extended cyclability, low self-discharge rates, precise electrode-electrolyte interface control, and improved safety.<sup>12, 90</sup> The major challenge in SSBs arises from their planar configuration, limiting power densities. This can be overcome by simultaneously increasing power and energy density by fabricating the SSB in a 3D configuration.<sup>11</sup> ALD is an ideal technique for fabricating such devices due to its ability to grow

conformal layers over complex 3D architectures.<sup>15</sup> Pearse et al<sup>10</sup> recently reported the first fully conformal 3D SSB, in which ALD was used to deposit all active components. Building upon this achievement, we are interested in exploring thin-film SSBs comprised of more abundant materials, specifically a SIB as an alternative to the LIB.

Herein, we report the development of the first Na-ion conductor synthesized by ALD, sodium phosphorus oxynitride (NaPON). NaPON is analogous to lithium phosphorus oxynitride (LiPON), the most successful thin-film SSE, which was developed at Oak Ridge National Laboratory.<sup>26</sup> Within the past few years, ALD processes have emerged for polymorphs of LiPON.<sup>33-36</sup> The aforementioned conformal 3D SSB<sup>10</sup> was enabled by the development of a lithium polyphosphazene (Li<sub>2</sub>PO<sub>2</sub>N) (LPZ) thermal ALD process involving two reactants, lithium tert-butoxide (LiO<sup>t</sup>Bu) and diethylphosphoramidate (DEPA).<sup>35</sup> In this work, we explore the reaction of sodium tert-butoxide (NaO<sup>t</sup>Bu) and DEPA as a direct extension of the thermal LiPON LPZ process. As this is a new ALD process, the growth characteristics and chemical composition are first investigated as a function of temperature. Its electrochemical properties are also examined for the potential use in a thin-film Na SSB. The NaPON solid electrolyte possesses an ionic conductivity of  $1.0 \times 10^{-7}$  S/cm at room temperature and an activation energy of 0.53 eV, demonstrating its capability to serve as a stable Na-ion conductor, particularly if employed in very thin electrolyte layers (<50nm) as already reported for the LiPON LPZ analog.

### ***3.3. Experimental Procedures***

#### **ALD Process Development**

Prior to ALD growth, thermogravimetric analysis (TGA) was performed on NaO<sup>t</sup>Bu using a PerkinElmer Pyris. The measurement was carried out at atmospheric pressure with a 20 SCCM

flow of nitrogen. The sample was held at 27 °C for 15 min to purge out any contaminants from brief air exposure of the powder, and then heated to 500 °C at a rate of 5 °C/min.

Test-grade Si (100) wafers (University Wafer) were used as substrates throughout this work. For ALD growth studies, Si wafers were rinsed stepwise with acetone, isopropyl alcohol, and deionized water. The wafers were then blown dry and pumped down in a load lock to  $10^{-6}$  Torr before loading into the ALD reactor. For electrochemical characterization, a passivation layer of  $\text{Si}_3\text{N}_4$  (~400 nm) was grown on Si wafers by LPCVD in a Tystar CVD furnace. A platinum current collector (~50 nm) with a titanium adhesion layer was then deposited in an Angstrom E-beam evaporator. The wafers were then diced into 1x1 cm<sup>2</sup> chips using a dicing saw. The chips were subsequently cleaned thoroughly and loaded into custom built sample holders for transfer into the ultra-high vacuum (UHV) system for ALD deposition.

ALD depositions were carried out at 250-400 °C in a Cambridge Nanotech (now Veeco) Fiji F100 ALD reactor coupled to an UHV cluster system ( $< 1 \times 10^{-8}$  Torr). The base pressure of the ALD reactor was  $1 \times 10^{-6}$  Torr, and the process pressure was maintained at ~200 mTorr by flow of UHP Argon (Airgas, 99.999%) gas. Sodium *tert*-butoxide ( $\text{NaO}^t\text{Bu}$ ) (Sigma, 97%) and diethyl phosphoramidate (DEPA) (Sigma, 98%) were chosen as precursors based on our prior work<sup>10, 35</sup> and were used as received.  $\text{NaO}^t\text{Bu}$  was loaded into a stainless steel bubbler and heated to 155 °C, while DEPA was loaded into a standard stainless steel cylinder and heated to 115 °C. A 60  $\mu\text{m}$  VCR filter was included at the outlet of the  $\text{NaO}^t\text{Bu}$  bubbler to prevent fine particles entering the reactor. Film thickness was monitored *in-operando* using a J.A. Woolam M-2000D spectroscopic ellipsometer with a spectral range of 220-1000 nm. Data was fit to a single Tauc-Lorentz oscillator model.

## Characterization

After deposition, films were transferred under UHV directly to a Kratos Ultra Surface Analysis System ( $1 \times 10^{-9}$  Torr) for X-ray photoelectron spectroscopy (XPS) analysis. All XPS data were collected using monochromatic Al K $\alpha$  radiation (12 kV) at a total power of 144 W. Survey spectra were collected using a pass energy of 160 eV and a binding energy step size of 1 eV. High-resolution spectra were collected using a pass energy of 20 eV and a binding energy step size of 0.1 eV. Charge neutralization was employed using the flood gun with 1A filament current, 1.15 V charge balance, and 1 V filament bias. Samples were observed not to change over time in the vacuum environment. All data was analyzed using CasaXPS with a Shirley background and 50/50 Gaussian/Lorentzian pseudo-Voigt functions. High-resolution peak area ratios were used for elemental quantification, using tabulated Kratos relative sensitivity factors. All spectra were calibrated to the P 2P ( $j=3/2$ ) peak at 132.3 eV.

SEM and FIB cross sections were performed using a Tescan GAIA dual SEM/FIB system. For conformality studies, NaPON was deposited into high aspect ratio anodic aluminum oxide (AAO) nanopores on wafer substrates and analyzed by energy-dispersive X-ray spectroscopy (EDS) in a Hitachi SU-70 SEM. Crystallographic characterization was carried out on 1000 cycles of NaPON deposited on Si and Pt substrates using a PANalytical XPert Pro MRD system. X-ray Diffraction (XRD) scans were measured at a scan range of  $2\theta = 10-90^\circ$  with a step size of  $0.1^\circ$ . Ex-situ atomic force microscopy (AFM) characterization was performed using a NT-MDT NTEGRA instrument.

## Electrochemistry

Devices for electrochemical testing were prepared by depositing 1000 cycles of NaPON onto the Pt coated chips that were fabricated as described above. A stainless steel shadow mask

with various circular holes was used to pattern the top current collector for device testing. Two methods were used for depositing top contacts. The first, NaPON films were briefly exposed to air before deposition of Pt by E-beam evaporation. Second, Au was deposited by a custom-built thermal evaporator coupled to the ALD reactor and glovebox through a UHV cluster tool. The contrast between the two methods provided important insight into the effect of air exposure on the NaPON electrolyte. Electrochemical impedance spectroscopy (EIS) was performed using a Biologic VSP potentiostat inside an Ar-filled glovebox (<0.1 ppm H<sub>2</sub>O and O<sub>2</sub>). Samples were mounted on a custom-built mica glass-ceramic stage with a PID temperature controller, and electrical contact was made with micromanipulator probes. EIS measurements were collected at 25-80 °C at a frequency range of 500 kHz-300 mHz with a sinusoidal amplitude of 10 mV.

### 3.4. Results and Discussion:

#### Atomic Layer Deposition Process Parameters

NaO<sup>t</sup>Bu was chosen as the precursor for a sodium source due to the success of LiO<sup>t</sup>Bu in depositing lithium containing films.<sup>35, 36, 91, 92</sup> There has been little effort in sodium-based ALD processes, but NaO<sup>t</sup>Bu has been used to deposit sodium aluminates<sup>93</sup> and sodium titanates.<sup>89</sup> In evaluating new precursors, it is critical to determine their vaporization behavior. Figure 3.1 shows the TGA curve measured for NaO<sup>t</sup>Bu, from which a sharp weight loss of ~70% between 220-300 °C is observed, followed by a minor drop of ~10% at 300-400 °C. The sublimation of NaO<sup>t</sup>Bu is represented by the sharp weight loss in a single step, indicating desirable precursor volatilization properties of NaO<sup>t</sup>Bu. This is in agreement with TGA data of alkali tert-butoxides in the literature.<sup>91, 93</sup> Based on the TGA curve for NaO<sup>t</sup>Bu and instrumentation limits, it was determined

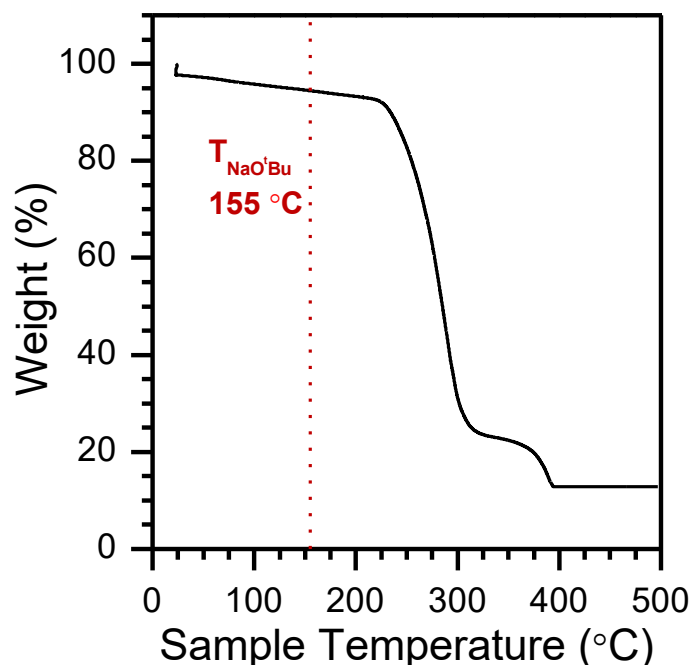


Figure 3.1. TGA curve of NaOtBu. NaOtBu was heated at a rate of 5 °/min under N<sub>2</sub> flow. The dotted line indicates the NaOtBu source temperature for ALD depositions.

to heat the precursor to 155 °C for ALD depositions. The TGA curve of DEPA was previously measured by Nisula et al.<sup>34</sup>, which showed complete weight loss in a single step with evaporation beginning ~95 °C.

The ALD process parameters were explored using *in-operando* spectroscopic ellipsometry (SE), with the results of these experiments shown in Figures 3.2a-c. Initial pulse times of 20s for NaO<sup>t</sup>Bu and 2s for DEPA were chosen based on the optimized LiPON process (LiO<sup>t</sup>Bu-DEPA) we have previously published.<sup>35</sup> Figure 3.2a shows the growth per cycle (GPC) of the NaPON process as a function of reaction temperature from 250-400 °C. The process does not display the typical temperature window (i.e. a region with a temperature-independent GPC) that is normally

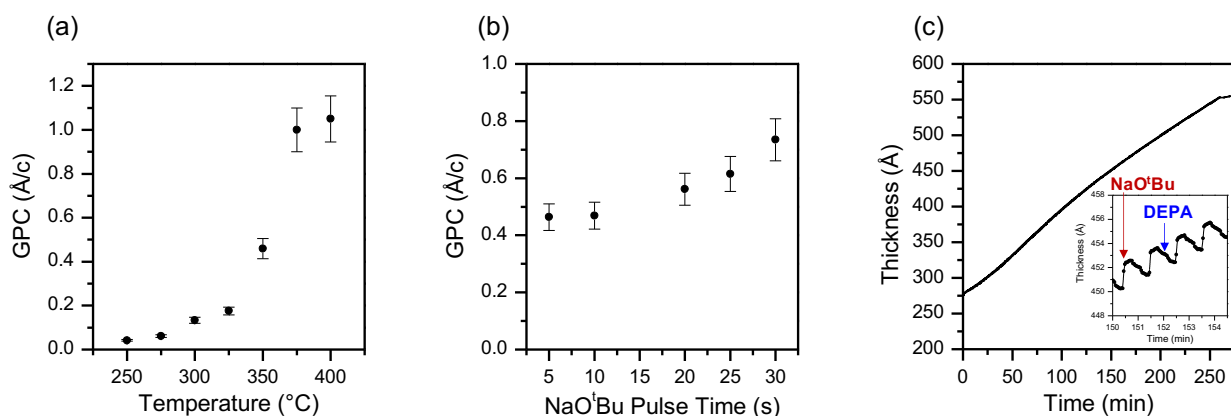


Figure 3.2. ALD process parameters of NaOtBu-DEPA measured by *in-situ* spectroscopic ellipsometry. (a) Growth rate per cycle as a function of reactor temperature. (b) Growth rate per cycle as a function of NaOtBu pulse time. The DEPA pulse was fixed at 2s. (c) Thickness profile for 250 cycles of NaPON deposited at 375 °C.

associated with an ideal ALD process. Instead, the GPC increases continually as a function of temperature. These results indicate some amount of CVD-like behavior contributing to the increase in growth rates. The GPC was measured to be <0.2 Å/cycle up to 325 °C, but increased to 0.5 Å/cycle at 350 °C. At even higher temperatures the growth continued to increase, reaching ~1.0 Å/cycle at 400°C. Figure 3.2b shows the growth rate with varying NaO<sup>t</sup>Bu dose with a constant DEPA pulse of 2s. The GPC was taken as an average over the 100 cycles after steady-state growth was achieved. The GPC can be seen to increase with increasing NaO<sup>t</sup>Bu dose time, indicating that

the NaO<sup>t</sup>Bu half-reaction is not self-limiting. Despite these non-ideal observations, linear and stepwise growth is captured by SE in Figure 3.2c and its inset, showing clear thickness increases associated with individual precursor pulses.

The non-ideal characteristics of the NaPON process can be attributed primarily to the NaO<sup>t</sup>Bu precursor. The reaction required higher temperatures than initially expected, as the LiO<sup>t</sup>Bu-DEPA process<sup>35</sup> exhibited a growth rate of  $\sim 0.9$  Å/cycle at 300 °C, there is negligible growth at this temperature for NaPON. We suggest this is related to the larger atomic radius of Na than Li, as the NaO<sup>t</sup>Bu complex is bulkier and therefore less volatile than LiO<sup>t</sup>Bu. NaO<sup>t</sup>Bu also does not display any growth saturation with DEPA, but saturation of LiO<sup>t</sup>Bu did occur at a 20s pulse time with a DEPA pulse of 2s. Liu et al.<sup>89</sup> reported saturated growth when using NaO<sup>t</sup>Bu as the sodium source for the ALD deposition of sodium titanates. This suggests that the reaction of NaO<sup>t</sup>Bu-DEPA may be more complex than the reactions of LiO<sup>t</sup>Bu-DEPA and NaO<sup>t</sup>Bu-H<sub>2</sub>O, requiring further studies aimed at understanding the surface mediated reaction chemistry.

### **Chemical Characterization by XPS**

Chemical characterization of NaPON was carried out by directly transferring samples from the ALD reactor to a UHV coupled XPS to avoid air exposure. The characterization of sodium-containing films without air exposure is extremely important due to the film's rapid reaction with atmospheric contaminants. Our unique laboratory setup is able to preserve the structure of the films for precise characterization. The composition of films deposited from 300-375 °C is summarized in Figure 3.3b. A survey spectrum can be seen in Figure 3.3a and shows all expected peaks at the expected energy positions. All fitted peaks were calibrated to the P 2p ( $j = 3/2$ ) peak at 132.3 eV instead of the frequently used adventitious C 1s peak. The P 2p peak provides a better reference for energy scale correction in sodium phosphates<sup>94, 95</sup> because the phosphorus atom is in a single

chemical state. This calibration point is further verified by the near exact match of all components with the binding energies of the ALD LPZ film we previously published.<sup>35</sup>

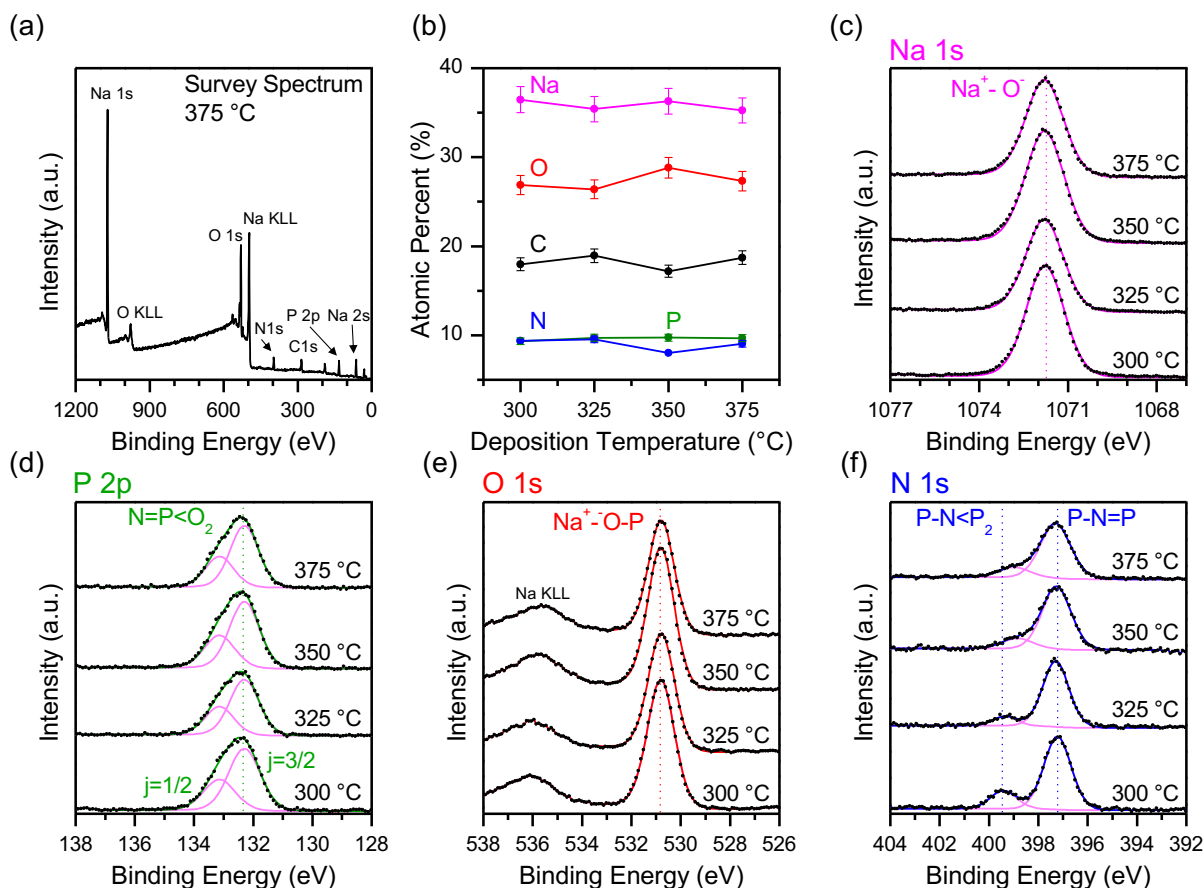


Figure 3.3. XPS Analysis of ALD NaPON Films. (a) Survey spectrum of NaPON deposited at 375 °C. (b) NaPON stoichiometry as a function of temperature. (c-f) High resolution core level spectra of NaPON films deposited between 300-375 °C.

High-resolution XPS spectra are shown in Figures 3.3c-f. There is only one distinguishable component for sodium, phosphorus, and oxygen observed for the core level spectra. The Na 1s spectra in Figure 3.3c shows a single peak at 1071.8 eV assigned to  $\text{Na}^+\text{-O}^-$ , which is consistent with the expected polyphosphazene structure. The P 2p spectra in Figure 3.3d has two peaks centered at 132.3 eV and 133.1 eV due to spin-orbit splitting. These peaks were assigned to the phosphorus atom ( $=\text{P}-$ ) linking the oxynitride chain. The O 1s spectra in Figure 3.3e shows a single

peak at 530.8 eV assigned to P-O<sup>-</sup>-Na<sup>+</sup>. The N 1s spectra in Figure 3.3f contains two peaks, a large peak at 397.2 eV assigned to doubly coordinated N (P-N=P) and a smaller peak at 399.4 eV assigned to triply coordinated (P-N<P<sub>2</sub>). Reidmeyer et al.<sup>96, 97</sup> reported XPS quantification of sodium oxynitride glasses with binding energies of 397.9 eV for -N= and 399.4 eV for -N<, which is in strong agreement with this work. It was observed that the N 1s peaks slightly broaden in films deposited at higher temperature, attributed to the thermal decomposition of the precursors at higher temperatures resulting in a less precise structure. The C 1s spectra is shown in Figure 3.4, which arises from residual hydrocarbon precursor ligands in the film. The C 1s spectra display differential sample charging, signified by the small shoulder peak at low binding energy present in samples deposited at 300-375 °C.

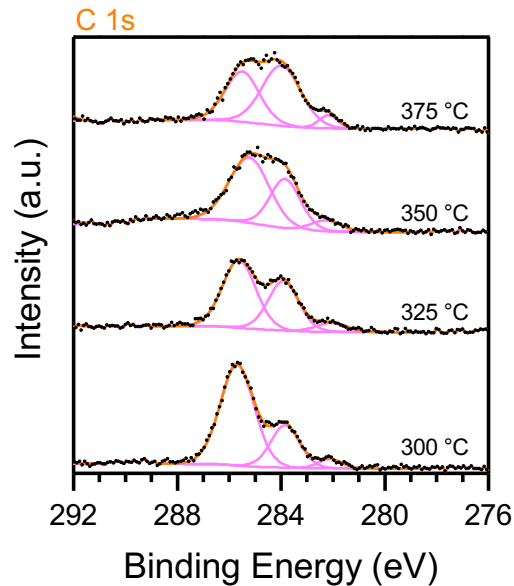


Figure 3.4. High resolution C 1s core level spectra of NaPON deposited at 300-375 °C.

From these spectra we conclude that the NaPON films possess a nearly constant stoichiometry of Na<sub>4</sub>PO<sub>3</sub>N(C<sub>2</sub>) as the spectra of the individual components are unchanged with temperature. Conventional preparation of oxynitride glasses by reactive RF sputtering<sup>26, 31</sup> or

annealing phosphate glasses in  $\text{NH}_3$ <sup>98</sup> are unable to completely replace the O atoms with N atoms in the backbone of the oxynitride chain. In such films, the O 1s spectra typically shows two peaks, a bridging oxygen (P-O-P) and a non-bridging oxygen (P-O). However, using a precursor with a pre-built P-N bond (DEPA), the resulting NaPON film here contain no bridging oxygen. This is evidenced by the O 1s spectra showing a single peak with a FWHM of 1.3 at 530.8 eV. This peak matches the P-O bond at 530.6 eV in the ALD LPZ film we published previously.<sup>35</sup> There is no shoulder associated with C-O bonding in the O 1s spectra, however the films contain 17-18% carbon. This is slightly higher than that observed in the ALD LPZ process (10% at 300 °C and 17% at 250 °C). Also, a small shoulder in the O 1s spectra at ~533 eV was observed in the ALD LPZ film, corresponding to P-O-C. However, it is interesting and evident that none such peak is observable for NaPON. The resulting carbon incorporation is due to incomplete reactions or decomposition of the organic precursor ligands (tert-butoxide and diethyl groups). It is important to note that the N/P ratio is one in all of the deposited films, signifying that the N-P bond in the DEPA precursor remains intact during the ALD reactions, similar to the  $\text{LiO}^t\text{Bu-DEPA}$ <sup>35</sup> reaction published previously. The N/P ratio of LiPON films is known to have a profound impact on the ionic conductivity of the films, with higher nitrogen content correlating to a higher ionic conductivity and lower activation energy.<sup>31, 32</sup> A similar trend is expected to occur in NaPON due to the similarities in the oxynitride binding network of NaPON and LiPON glasses.

In comparing the stoichiometry of ALD NaPON ( $\text{Na}_4\text{PO}_3\text{N}$ ) and LiPON ( $\text{Li}_2\text{PO}_2\text{N}$ ), the  $\text{NaO}^t\text{Bu-DEPA}$  process did not indicate a simple replacement of Li by Na. However, structural analysis by XPS shows a close resemblance with LiPON<sup>35</sup> and sodium oxynitride glasses<sup>96, 97, 99</sup>. Despite the variations in growth rate of the film depicted in Figure 3.2a with temperature, it is interesting that the chemical composition remains constant for films deposited at 300-375 °C

(Figure 3.3b). Although the ALD process is non-ideal, the chemistry of the deposited film is determined to be quite robust. The N/P ratio is 1 and the appearance of single chemical states for P, O, and Na support the classification of NaPON as a sodium polyphosphazene. The films exhibit an amorphous morphology in the deposited temperature range, as indicated by the lack of reflections in the XRD pattern in Figure 3.5 and low surface roughness (2.1 nm) measured by AFM.

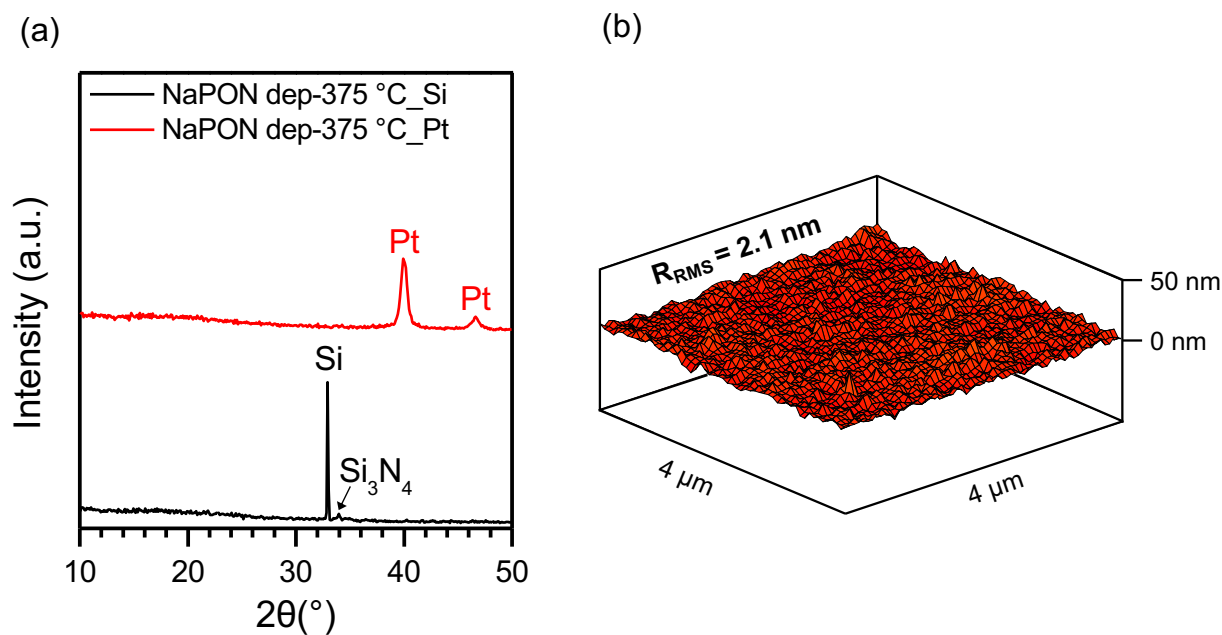


Figure 3.5. Morphology of NaPON. (a) XRD of 1000 cycles of NaPON deposited at 375 °C on Si and Pt substrates. The only identifiable peaks are those of the substrates. (b) AFM 3D topography of 1000 cycles of NaPON deposited at 375 °C on Si.

## Conformality

For conformality studies, a modified ALD process was used in which a throttle valve to the pump was closed off during precursor pulse and opened completely for purging. This process consisted of a pulse-exposure-purge sequence. The sequence for NaO<sup>t</sup>Bu was 10s-10s-30s and 2s-10s-30s for DEPA. To enable 3D Na SSBs, all layers must be able to conformally coat substrates with high aspect ratios. ALD is ideal for such coatings as it is based upon sequential surface reactions. To test the conformality of the NaPON ALD process, NaPON was deposited into AAO nanopore substrates with ~400 nm wide pores and 15 μm depth. The pores were closed at the bottom, preventing deposition from both directions.

Figure 3.6a shows a NaPON coating of ~50 nm extending along the pore walls about halfway down. Figure 3.6b and c show EDS mapping and line scans through the AAO pores. EDS mapping shows ~7 μm thickness of sodium distribution into the AAO. The line scans show reasonably uniform sodium and phosphorus content ~7 μm into the pores, and then their intensities decrease while aluminum and oxygen signals increase due to the AAO substrate. The inability of the NaPON film to completely coat the 15 μm deep pore can be ascribed to the non-ideal nature of the ALD process. The ALD reaction of NaO<sup>t</sup>Bu-DEPA was found to be non-self-limiting, which

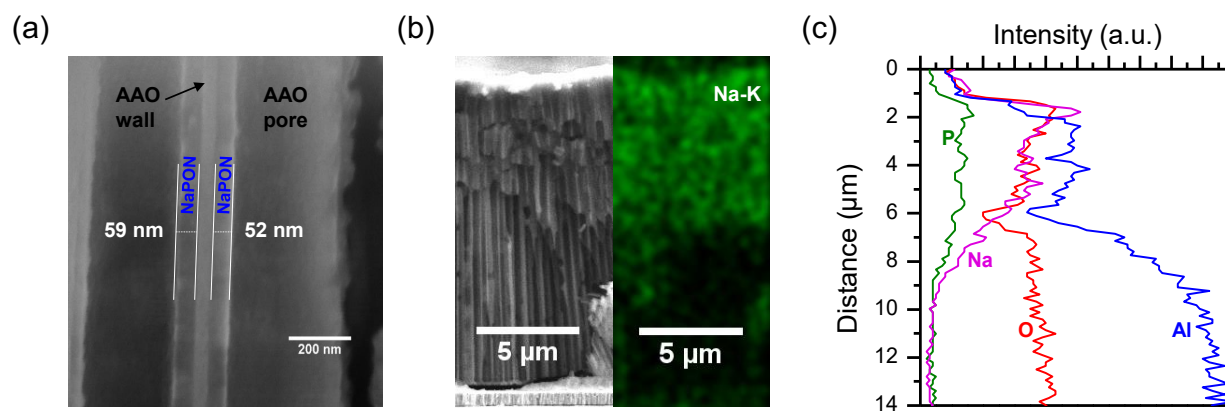


Figure 3.6. SEM images of NaPON in AAO. (a) Cross-section of NaPON/AAO showing deposition along the pore walls. (b) Cross section of AAO and Na EDS mapping (c) EDS line scan through an AAO pore showing atomic distribution.

hinders the films growth in nanosized pores. To improve conformality depth into nanopore structures, alterations in the ALD process should be considered, such as extending the dose and purge times. While not fully optimized, these results are promising towards developing 3D Na SSBs in high-aspect ratio structures.

### **Electrochemical Characterization**

In evaluating new SSE materials, the ionic conductivity is a key property. To test the ionic transport properties of NaPON, EIS was performed on films grown at 375°C. The effect of air exposure, electrode area, and temperature were investigated (Figure 3.7, Figure 3.8, and Table 3.1). Devices were prepared by depositing NaPON between two Pt blocking electrodes, as shown in Figure 3.7a. The top contacts were deposited through a shadow mask to provide circular electrodes of varying sizes on a single sample. Initially, the top current collector was deposited with brief air exposure of the film for transfer to an E-beam evaporator. The film reacted rapidly upon air exposure and could visually be seen to change color on the scale of minutes. To circumvent this issue, we used an effusion cell to evaporate Au in our custom-built multi-chamber UHV system. By comparing the different sets of samples, the effect of degradation in air on electrochemical performance could be evaluated.

Room temperature EIS measurements of air exposed and pristine (no air exposure) samples were performed to determine the ionic transport properties of NaPON, shown in Figure 3.7. The Nyquist plots all display a semicircular arc at high frequencies and a sharp increase in the imaginary impedance component at low frequencies. We note that the imaginary and real part of the plot decrease significantly with the area but that the shape of the plot remains constant. This indicates the ionic transport mechanism remains unaltered while changing the active electrochemical area of the measurement. The equivalent circuit used to model the EIS curves

includes parallel resistor-constant-phase element (CPE) components for the high-mid range frequencies with another CPE in series for the low frequencies, as shown in the inset of Figure 3.7b and c. For the high-mid range frequencies, to extract resistance values  $R$  from the semicircle and hence assess the ionic conductivity, a constant phase element rather than a pure capacitor was used to account for inhomogeneity within the thin films. The semicircular arc is associated with ion transport through the NaPON electrolyte and is assigned two CPE components for the air exposed sample (Figure 3.7b) and one component for the pristine sample (Figure 3.7c). At the highest frequencies, the first component,  $CPE_b$ , represents bulk ion conduction of the amorphous

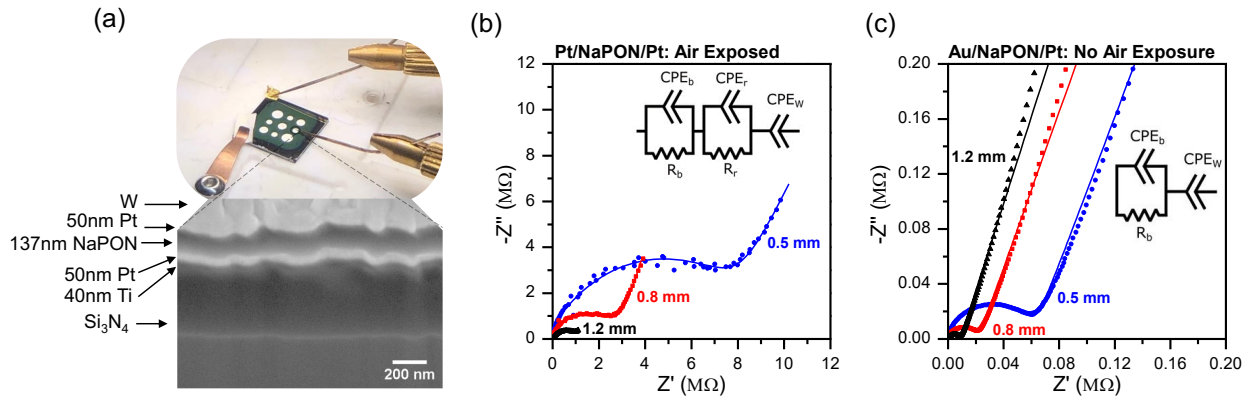


Figure 3.7. Electrochemical characterization of NaPON. (a) FIB-SEM cross section and optical image of Pt/NaPON/Pt stack used for electrochemical analysis. (b) Nyquist plot of air exposed Pt/NaPON/Pt devices of varying electrode surface area. (c) Nyquist plot of pristine Au/NaPON/Pt devices of varying electrode surface area. NaPON films were deposited on Pt at 375 °C.

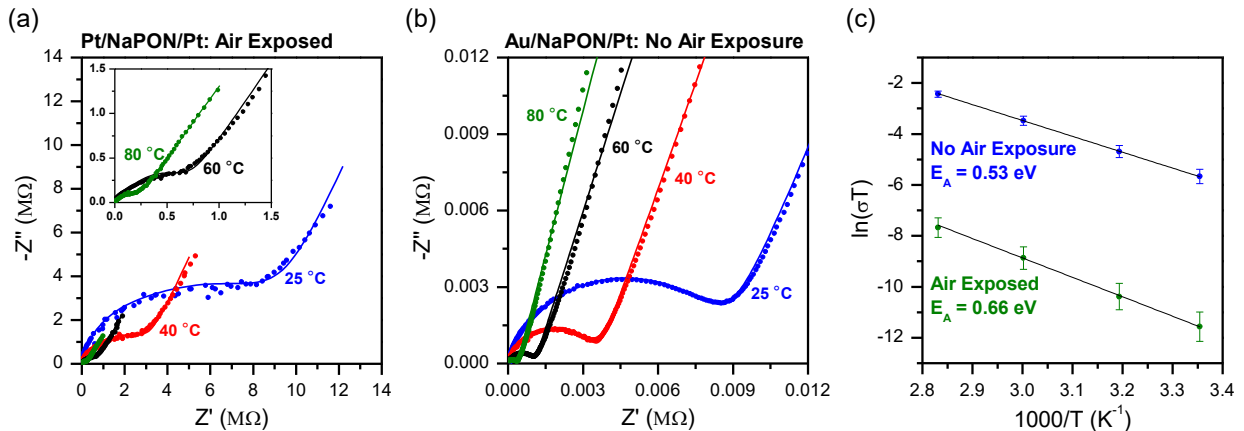


Figure 3.8. Transport Properties of NaPON. (a) Nyquist plots of air exposed Pt/NaPON/Pt devices between 25-80 °C. (b) Nyquist plots of Au/NaPON/Pt between 25-80 °C. (c) Arrhenius plots for air exposed and non-air exposed NaPON films showing activation energies of the films.

film. The second component at mid-range frequencies,  $CPE_r$ , is assigned to an interphase layer formed upon air exposure. The ionic conductivity for the air exposed film was calculated from the sum of the resistance ( $R_h$  and  $R_r$ ), whereas the pristine film only had contribution from  $R_b$ . At low frequencies a  $CPE_w$  is used to fit the Warburg-like diffusion associated with the blocking electrodes.

The samples exposed to air displayed a low average ionic conductivity of  $1.3 \times 10^{-9} \pm 2.4 \times 10^{-10}$  S/cm at room temperature. This ionic conductivity is  $\sim 2$  orders of magnitude lower than that typically observed in  $Li^+$  conducting electrolytes produced by ALD.<sup>34-36, 100-102</sup> The high resistance of the film is most likely related to the reactive layer ( $CPE_r$ ) formed upon air exposure. This is confirmed by the drastic increase in conductivity for the pristine samples, with  $\sigma = 1.0 \times 10^{-7} \pm 7.9 \times 10^{-9}$  S/cm at room temperature. The ionic conductivity of pristine ALD NaPON is comparable and even higher than some of the ALD  $Li^+$  conducting electrolytes. The enhancement was a result of depositing the entire device and testing without air exposure, thus avoiding contamination/reaction and consequently avoiding formation of the impeding interphase layer.

EIS measurements were also performed on the samples at varying temperature from room temperature to 80°C, with the results shown in Figure 3.8a and b. The Nyquist plots display the same features at elevated temperatures as at room temperature, with resistance decreasing as a function of temperature. As a result, the equivalent circuit models described above were used again to extract the ionic conductivities. Ionic conductivity displays an Arrhenius behavior with a dramatic improvement in temperature, from  $1.0 \times 10^{-7}$  S/cm at room temperature, to up to  $2.47 \times 10^{-6}$  at 80 °C for the samples not exposed to air (Figure 3.8 and Table 3.1). The Arrhenius plot in Figure 3.8c shows the ionic conductivity as a function of temperature for air exposed and pristine NaPON films. It should be noted that the air-exposed NaPON aged in the glovebox  $\sim 3$  months

after the EIS data in Figure 3.7b was collected. The result of this was an order of magnitude decrease in the room temperature conductivity from initial measurements. The perfect linear relationship between the ionic conductivity and the temperature indicate that the NaPON solid electrolyte is stable within the temperature range measured. From the slope of these curves, activation energies for Na<sup>+</sup> transport can be determined by using the Arrhenius relation for conductivity:  $\sigma T = Ae^{-\frac{E_A}{kT}}$ , where  $\sigma$  is the ionic conductivity,  $T$  is temperature,  $A$  is the pre-exponential factor,  $E_A$  is the activation energy, and  $k$  is the Boltzmann constant. The activation energy represents the thermal energy required for ionic migration and is a critical parameter for SSEs. The activation energy for the air exposed film is 0.66 eV, while the activation energy for the pristine film is 0.53 eV. The lower activation energy is further evidence for the removal of the resistive interphase layer formed upon air exposure. In addition, the activation energy for NaPON is on the same order of that of the ALD LPZ film (0.64 eV for air exposed and 0.55 eV for pristine LPZ).<sup>35</sup> This indicates that despite the larger ionic radius of Na, the kinetics of ionic migration are facile in the amorphous NaPON network and are comparable to that in LiPON. This demonstrates the potential to develop thin-film SIBs using a NaPON solid electrolyte.

Table 3.1. Summary of Ionic Conductivity Results for Air Exposed and Pristine NaPON<sup>a</sup>.

	temperature (°C)			
	25	40	60	80
electrode diameter (mm)	0.5	0.8	1.2	
Na <sup>+</sup> conductivity (10 <sup>-7</sup> S/cm) <i>air exposed NaPON</i>	0.011	0.011	0.015	0.010
Na <sup>+</sup> conductivity (10 <sup>-7</sup> S/cm) <i>pristine NaPON</i>	1.03	1.00	1.15	2.93

<sup>a</sup>The Error for all measurements is within 5% (Table S1).

### 3.5. Discussion

The profound impact of air exposure on the NaPON films is evident from the very large (100X) differences in ionic conductivity with vs without the air exposure. The preservation of

pristine NaPON is thus crucial, implying that precautions must be taken in characterization of NaPON and of course in any corresponding manufacturing. LIBs are typically manufactured in dry rooms. However, in our experience with handling ALD NaPON and LiPON solid electrolyte materials, the sodium film is much more sensitive to air exposure than the lithium version. With that being said, the production of NaPON may require further protective measures be taken to ensure its optimal performance, which may be impractical for manufacturing. A careful analysis aimed at understanding the air reactivity should be investigated, determining if degradation arises mainly from H<sub>2</sub>O, or O<sub>2</sub> and even CO<sub>2</sub>.

The oxidation resistance of silicate-based oxynitrides has been reported by several studies<sup>103-105</sup>, but the oxidation behavior of other oxynitride glasses such as sodium and lithium based glasses is poorly understood. Parashiv et al.<sup>106</sup> recently investigated the structural stability of NaPON glass and found an overlapping effect of crystallization with oxidation in the oxynitride network. Their work suggested that NaPON glasses maintain their core structural features but undergo a thermally driven depolymerization at temperatures near the glass transition temperature. Their findings also indicate that as oxidation occurs, triply coordinated nitrogen (-N<) is more sensitive to replacement with O in the glass network than doubly coordinated nitrogen (-N=). There are certainly differences in the bulk/powder NaPON glasses in the study and the ALD films reported here, but these general conclusions certainly inform the results witnessed here.

As mentioned in the introduction, comparison to thin film Na<sup>+</sup> conductors reported in the literature is difficult as most are relatively thick (>1000 nm) and were deposited through physical vapor deposition. A sputtered NaPON film was reported by Chun<sup>55</sup> and shown to have a room temperature ionic conductivity of  $8.7 \times 10^{-6}$  S/cm with an activation energy of 0.164 eV. However, the author did not present any chemical analysis (i.e. XPS, TOF-SIMS, EDS, *etc.*) to confirm the

film stoichiometry thus preventing a direct comparison. Sputtered NASICON ( $\text{Na}_3\text{Zr}_2\text{Si}_2\text{PO}_4$ ) has been reported for applications in  $\text{CO}_2$  sensors and electrochromic devices.<sup>53, 54</sup> Horwat et al.<sup>54</sup> reported room temperature ionic conductivity of  $3.1 \times 10^{-5}$  S/cm for amorphous as-deposited films (1000 nm). Bang et al.<sup>53</sup> reported an ionic conductivity of 0.29 S/cm at 200°C with an activation energy of 0.55 eV for an annealed crystalline NASICON film (2000-2500 nm). The energy barrier for  $\text{Na}^+$  conduction in sputtered NASICON (0.55 eV) is nearly the same as that observed here for ALD NaPON (0.53 eV). Although the activation energies are in agreement, the room temperature ionic conductivity of NASICON is  $\sim 2$  orders of magnitude higher than that in NaPON. This is due to higher diffusivity in the crystalline NASICON structure that possess a framework of 3D interconnected channels for ion motion.

The electrochemical properties of NaPON in this study were measured on films deposited at 375 °C because of the higher growth rate ( $\sim 1$  Å/cycle) while preserving the chemical composition of  $\text{Na}_4\text{PO}_3\text{N}$ . The electrochemical properties are not believed to change drastically when deposited at lower temperatures as the stoichiometry is constant and the films are amorphous. Though, it should be noted the XPS results in Figure 3.3f do show minor structural changes in the N 1s spectra in the deposited temperature range of 300-375 °C. These subtleties may have some effect on the ionic conductivity. The carbon content of the film is constant at all temperatures and therefore its direct effect on the ionic conductivity cannot be determined. However, the EIS measurements shown in Figure 3.7 and Figure 3.8 give us an indication. A significant increase in ionic conductivity and decrease in activation energy was observed in pristine NaPON vs. air-exposed NaPON. This air exposure certainly adds carbon to the surface of the film, decreasing the ionic conductivity. It is therefore safe to conclude less carbon in the films would be desirable and may offer some improvements in ionic transport.

For the realization of thin-film sodium SSBs, further electrochemical characterization of NaPON is required. Such characterization includes examining electrochemical properties of NaPON films as a function of deposition temperature, thickness, and stability against electrode materials. Despite the lower ionic conductivity of ALD NaPON compared to sputtered NaPON and NASICON, it poses the potential to provide increases in energy density in SSBs beyond those fabricated by sputtering. This is due to the ability for ALD SSEs to be ionically conductive without device shorting at  $\sim 1/10^{\text{th}}$  of the typical thickness of sputtered SSEs. Talin et al.<sup>13</sup> demonstrated that sputtered SSB layers are ineffective in coating 3D nanostructures required for high energy and power devices, due to the poor deposition conformality. The electrochemical and chemical stability of NaPON with electrode materials also needs evaluation for battery development. Reversible sodium ion-insertion is well known and has been demonstrated in readily available ALD electrode materials, such as  $\text{V}_2\text{O}_5$ <sup>107</sup> cathodes and  $\text{TiO}_2$ <sup>108, 109</sup> and  $\text{SnO}_2$ <sup>110</sup> anodes. Thus, we foresee the implementation of NaPON in 3D fully conformal SSBs, as we have had success with lithium conformal SSBs that utilize the similar LPZ SSE.<sup>10</sup>

### **3.6. Conclusions**

This work demonstrates the development of a new solid electrolyte for sodium batteries, NaPON, which is the first  $\text{Na}^+$  conductor fabricated by ALD. The ALD process of  $\text{NaO}^t\text{Bu-DEPA}$  was found to be a non-ideal, but well-behaved, high temperature process. The surface chemistry of NaPON was examined by XPS without air exposure, showing a sodium polyphosphazene type structure similar to that observed in the ALD lithium polyphosphazene. The film composition of  $\text{Na}_4\text{PO}_3\text{N}$  was found to be unchanged in the temperature range of 300-375 °C. Minor carbon incorporation in the film was observed, likely due to secondary thermal decomposition of the organometallic ALD precursors during deposition. Electrochemical characterization using EIS

highlighted the sensitivity and criticality of preserving the structure of NaPON. At room temperature, an ionic conductivity of  $1 \times 10^{-7}$  S/cm was observed in the pristine NaPON film, two orders of magnitude higher than the air exposed film. The conductivity displays a perfect Arrhenius behavior pinpointing that the solid electrolyte is stable at elevated temperature and that the amorphous phosphorus oxynitride network is capable of conducting  $\text{Na}^+$  and  $\text{Li}^+$  at the same energy cost. NaPON is therefore a very attractive SSE for SIBs, specifically because of the success the LiPON SSE has had and their similarity.

The fabrication of materials that are conformal at the nanoscale in 3D structures and are ion-conducting is extremely attractive. The polyphosphazenes (NaPON and LiPON) produced by the ALD reaction of alkali tert-butoxides and DEPA require further characterization to understand their unique properties. It is interesting to broaden the work on the phosphorus oxynitride glasses to look at other ionic species such as  $\text{K}^+$  and  $\text{Mg}^{2+}$  because of their relevancy to energy storage systems.

# Chapter 4: Nanoscale Li, Na, and K Ion-Conducting Polyphosphazenes by Atomic Layer Deposition

## 4.1. Chapter Summary

A key trailblazer in the development of thin-film solid-state electrolytes has been lithium phosphorous oxynitride (LiPON), the success of which has led to recent progress in thin-film ion conductors. Here we compare the structural, electrochemical, and processing parameters between previously published LiPON and NaPON ALD processes with a novel ALD process for the K analogue potassium phosphorous oxynitride (KPON). In each ALD process, alkali *tert*-butoxides and diethylphosphoramidate are used as precursors. To understand the ALD surface reactions, this work proposes a reaction mechanism determined by *in-operando* mass spectrometry for the LiPON process as key to understanding the characteristics of the APON (A = Li, Na, K) family. As expected, NaPON and LiPON share similar reaction mechanisms as their structures are strikingly similar. KPON, however, exhibits similar ALD process parameters but the resulting film composition is quite different, showing little nitrogen incorporation and more closely resembling a phosphate glass. Due to the profound difference in structure, KPON likely undergoes an entirely different reaction mechanism. This chapter presents a comprehensive summary of ALD ion conducting APON films as well as a perspective that highlights the versatility of ALD chemistries as a tool for the development of novel thin film ion-conductors.

## 4.2. Motivating Nanoscale Ion Conductors

As electronic devices and systems shrink, those with onboard battery power become increasingly limited by the size of the battery. This is particularly critical in applications where space is at a premium, such as implantable biomedical devices (i.e., cardiac pacemakers, cardiac

defibrillators, neurostimulators, cochlear implants etc.), satellites, wearable electronics, and autonomous sensors.<sup>12, 111, 112</sup> Conventional battery architectures are difficult to shrink, in part because liquid electrolytes are retained in porous separators. The liquid electrolytes are flammable and produce toxic by-products when combusted or even exposed to air.<sup>1-3</sup> This increases safety concerns, particularly for implantable devices, where the consequences of failure are these same toxic chemicals leaking into the body cavity. Solid-state batteries (SSBs) are predicted to alleviate these safety concerns by replacing the liquid electrolyte with a solid material, referred to as solid-state electrolyte (SSE). To date however, the ionic conductivity of thin-film SSEs has not matched that of liquid electrolytes. Furthermore, replacing liquid electrolytes by their solid counterparts presents formidable obstacles – from forming high quality interfaces between electrodes and SSEs to altering battery manufacturing processes.

Our strategy is to design and fabricate nano- and micro-scale electrochemical energy storage devices using thin film fabrication as employed in semiconductor and related technologies to produce novel battery architectures.<sup>8</sup> In this way, we take advantage of decades of scalable manufacturing experience used for the fabrication of integrated chips (ICs), capacitors, solar panels, LCD screens, etc., where thin film fabrication is routinely employed to make very high density patterned 3D devices with extreme precision and success. High-aspect ratio structures have a similarly long history and have been used to increase the areal and volumetric densities of transistors, capacitors, and memory elements in CMOS fabricated devices. We use patterned nano-scale scaffold substrates such as etched silicon wafers and porous anodic aluminum oxide (AAO) to dramatically increase the active device surface area in the same two-dimensional footprint as non-patterned substrates.<sup>10, 113, 114</sup> This strategy necessitates the use of conformal deposition methods to fabricate our envisioned device architectures. Atomic layer deposition (ALD) is an

obvious choice as it is already used extensively in the semiconductor industry. ALD allows for the realization of this structure-based approach towards high-performance SSBs, of which we have demonstrated successful 3D energy storage devices such as an array of nanobatteries in nanoporous (AAO) and the first fully conformal 3D thin-film SSB.<sup>10, 113</sup>

### **4.3. Background**

#### **ALD Solid Electrolytes**

Considering active battery components, SSE materials are most challenging, given that the materials and their solid phase are new to the battery industry. This has made process development for ALD SSEs a highly active and ongoing field of research, for which recent progress has been thoroughly summarized by Han *et al.*<sup>20</sup> The first attempts at ALD SSEs were based on well-established ALD processes ( $\text{Al}_2\text{O}_3$ ,  $\text{TaO}_2$ ,  $\text{TiO}_2$ , etc.) modified by the addition of Li, resulting in  $\text{Li}_2\text{O-Al}_2\text{O}_3$  mixes<sup>115</sup>,  $\text{LiTaO}^{100}$ , and  $\text{LiAlSiO}^{116}$ . After these initial publications, two polymorphs of lithium phosphorous oxynitride (LiPON) were published nearly simultaneously. Our group published a quaternary plasma-enhanced ALD (PEALD) process using lithium *tert*-butoxide ( $\text{LiO}^t\text{Bu}$ ),  $\text{H}_2\text{O}$ , trimethyl phosphate (TMP), and plasma  $\text{N}_2$ , dosed sequentially without requiring super cycling.<sup>36</sup> The structural and electrochemical properties of LiPON are well known to be affected by N content<sup>31, 32</sup>, and as such the resulting films demonstrated varying degrees of crystallinity and ionic conductivity. This ALD process demonstrated remarkable tunability of N up to 16 %. Simultaneously to our work, Nisula *et al.*<sup>34</sup> developed a simpler binary ALD process using Li hexamethyldisilazide (LiHMDS) and diethylphosphoramidate (DEPA). This process produced a material with an N/P ratio of 0.6 and overall stoichiometry of  $\text{LiPO}_3\text{N}_{0.6}$ . Impressed with the simplicity of Nisula's process and given our experience with  $\text{LiO}^t\text{Bu}$ , we explored its reaction with DEPA. The results were different than both previously published ALD LiPON

processes. The substitution of LiO<sup>t</sup>Bu for LiHMDS leads to full nitrogenation of LiPON, resulting in a N/P ratio of ~1 and an overall stoichiometry of Li<sub>2</sub>PO<sub>2</sub>N.<sup>35</sup> Further chemical analysis, discussed in detail in section 4, showed that the material contained chains of primarily P-N=P bonds indicating a polyphosphazene like structure.<sup>38</sup> This unique LiPON process was a key enabler in the first fully conformal 3D thin-film SSB through its use as an ultrathin (40 nm) SSE.<sup>10</sup>

Several families of precursors have been tested for the purpose of introducing alkali cations into thin films by ALD. These include alkali trimethyl silanolates (TMSO), alkali hexamethyldisilazides (HMDS), alkali β-diketonates (thd), and alkali *tert*-butoxides (O<sup>t</sup>Bu).<sup>91, 117, 118</sup> The most well studied family, however, are the *tert*-butoxides, with LiO<sup>t</sup>Bu being the most common. It is part of a broader class of precursors called alkali *tert*-butoxides (AO<sup>t</sup>Bu) which include Li, Na, K, Cs, and Rb substitutes. They are strong non-nucleophilic bases with the degree of basicity increasing with alkali metal ion size. In part, these compounds do not take place in nucleophilic addition reactions as a consequence of the steric hindrance of the central C atom.<sup>119</sup> They are best handled in an inert environment, as they react violently and exothermically with water, forming a lithium hydroxide shell and releasing *tert*-butyl alcohol vapor, which can self-ignite. Despite these reports, some ALD groups allow for brief air exposure when filling delivery containers and the precursors are found to be safe to handle in air briefly below 35°C. In the vapor phase, AO<sup>t</sup>Bu do not retain a monomeric structure and have been shown to oligomerize, with the size varying as a function of the alkali metal mass. The lithium and sodium versions are well known to form a hexamer structure, while the heavier potassium, rubidium, and cesium *tert*-butoxides form a tetramer with a cubanelike structure.<sup>93, 120, 121</sup> Sonsteby *et al.*<sup>119</sup> have written an extensive review on AO<sup>t</sup>Bu's as precursors in ALD processes.

## Polyphosphazenes

As mentioned, the reaction between LiO<sup>t</sup>Bu and DEPA produces an inorganic polymer which can be classified as a polyphosphazene.<sup>35</sup> Polyphosphazenes are a well-studied class of inorganic polymers where the backbone structure contains no carbon, but rather repeating phosphorous and nitrogen atoms, with two substitute groups attached to each phosphorous atom as seen in Figure 4.1(a-c). They come in both cyclic and linear forms (Figure 4.1a and c). In most cases, the substitute groups are organic, leading to poly(organo) phosphazenes. The earliest known compounds were produced by Liebig and Wohler when a small amount of hexachlorocyclotriphosphazene was produced in 1834. Intensive investigation began in the mid-1960s after techniques were developed to replace the halogen with organic substitutes.<sup>37, 38</sup> This led to a wide variety of organophosphazenes being synthesized and studied.

The materials discussed in this chapter can be classified as poly(alkali) phosphazenes where the substitute groups attached to the phosphorous atoms are O<sup>-</sup>-A<sup>+</sup> (where A is Li, Na, or K). A depiction of an ideal alkali polyphosphazene chain is displayed in Figure 4.1b, along with 3D molecular structures of the linear and cyclic alkali polyphosphazene. While our focus is on ion conducting thin films, *tert*-butoxides present the broader ALD community an opportunity to study not only other alkali *tert*-butoxides to elucidate the reaction chemistry (the focus of this work) but, potentially a much broader class of materials where the substitution at the phosphorous atom is a functional organic group.

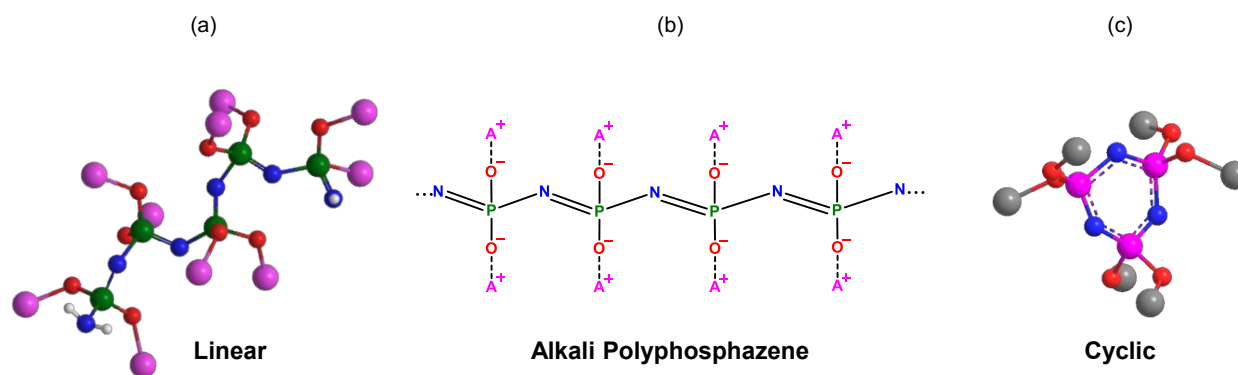


**Figure 4.1.** Molecular structure of an ideal alkali polyphosphazene. (a) 3D linear representation, (b) 2D structure based on the  $\text{Li}_2\text{PO}_2\text{N}$  structure described in this work, (c) 3D cyclic representation. The alkali ion  $A^+ = \text{Li}^+, \text{Na}^+, \text{K}^+$ .

### Lithium Phosphorous Oxynitride

Though the body of work for ALD ion conductors continues to grow, the most well-studied material is LiPON due to its attractive voltage stability window, its self-passivating interfaces, and large body of prior development work on the material using PVD.<sup>28</sup> LiPON was first developed as a sputtered SSE at Oak Ridge National Laboratory in the early 1990's by Bates *et al.*<sup>26, 27</sup> Even with this long history, the phosphorous oxynitride (PON) structure has been challenging to understand due to its amorphous nature. Despite this difficulty, there are several aspects of the bonding environment that are indicative of the structure and resulting properties. LiPON is part of a broader family of APON materials where the properties, including structure and ionic conductivity, are directly linked to the amount and coordination state of nitrogen in the film.<sup>31, 32</sup>

X-ray photoelectron spectroscopy (XPS) is the most common technique to characterize LiPON, in which the binding environment of the amorphous PON network can be determined. Bates *et al.*<sup>26, 27</sup> initially assigned two nitrogen states based on the XPS spectra of LiPON, a doubly coordinated nitrogen state ( $\text{N}_d$ ,  $\text{P-N=P}$ ) at low binding energy and a triply coordinated nitrogen

state ( $N_t$ , P-N<P) at higher binding energy. This agreed with earlier work in the 1980s on bulk nitrated lithium and sodium metaphosphate ( $Li/NaPO_3$ ) glasses.<sup>96, 99</sup> This convention continued and is most common for thin-film LiPON. However, it should be mentioned that Dudney and colleagues<sup>30</sup> recently suggested LiPON possesses only singly coordinated, or apical nitrogen ( $N_a$ , P-N) and  $N_d$  based on simulations and neutron scattering experiments to resolve the amorphous structure. Their simulations on LiPON with varying degree of N content imply the structure contained only  $N_a$  and  $N_d$ , and was in strong agreement with neutron scattering pair distribution function analysis on sputtered LiPON. It is important to note that the LiPON studied by Dudney and colleagues<sup>30</sup> was produced by sputtering, resulting in a stoichiometry of  $Li_{2.94}PO_{3.50}N_{0.31}$ . Furthermore, the authors mentioned they could not completely rule out the presence of  $N_t$  in the sputtered LiPON examined. This LiPON composition differs from that of our ALD LiPON ( $Li_2PO_2N$ )<sup>35</sup>, implying that the connectivity of the PON backbone may vary in polymorphs of LiPON. Due to the recent discrepancies and for consistency, we stick with the assignment of  $N_a$  and  $N_t$  for the APONs reported in this work.

## Goal

This work compares the reaction parameters, resulting chemical structure, and ion conducting properties of our two previously published LiPON and NaPON processes with new data that looks at the reaction between KO'Bu and DEPA. Section 4 discusses the ALD process parameters through *in-operando* spectroscopic ellipsometry (SE). The chemical structure of the three materials is discussed in section 5, where *in-vacuo* transfer to an XPS allowed for the measurement of pristine materials without contamination from air exposure. While the Li and Na substituted versions are shown to have very similar structures, interestingly the K version incorporates little N (2.2% max.), despite showing the presence of P. Next, in section 6, we present

*in-operando* mass spectrometry data for the (LiO<sup>t</sup>Bu + DEPA) LiPON process where we attempt to elucidate the reaction chemistry that leads to the unique polyphosphazene structure. In light of the structure and reaction chemistry of ALD LiPON, we propose a surface reaction scheme in section 7. In section 8, we discuss the electrochemical properties of the resulting thin films. Finally, we discuss, in a more holistic fashion, the implications of these materials from both an ALD process and application standpoint.

#### **4.4. ALD Process Parameters**

As discussed, LiO<sup>t</sup>Bu has been widely used as a precursor in ALD processes due to the pressing interest in applying ALD in Li battery technology.<sup>9,19</sup> The use of NaO<sup>t</sup>Bu and KO<sup>t</sup>Bu in ALD processes is growing with the recent interest in beyond Li-ion chemistries as well as applications in piezo/ferro-electric materials.<sup>119</sup> AO<sup>t</sup>Bu's inherently possess low vapor pressure, requiring higher temperature heating than most commonly used ALD precursors, and thus require bubbler assisted delivery to the ALD reactor. For the purposes of this discussion, we will focus on the AO<sup>t</sup>Bu + DEPA ALD process chemistries.

To understand the vaporization behavior of the AO<sup>t</sup>Bu's, thermogravimetric analysis (TGA) was conducted and compared to the literature. Figure 4.2 shows the TGA curves measured for Li-, Na-, and KO<sup>t</sup>Bu, in which all precursors display similar sublimation behavior. First, there is a small initial mass loss around 50 °C, corresponding to the release of crystal *tert*-butanol.<sup>119</sup> The onset temperature of vaporization is ~150 °C and proceeds in a single step for all precursors. These findings are well within literature values where available.<sup>91,93</sup> The residual mass varies from ~5% for LiO<sup>t</sup>Bu to ~12% for the K and Na substitutes. This additional residual mass is most likely due to the brief air exposure that forms alkali oxide and hydroxide decomposition products. The

onset temperature for AO<sup>t</sup>Bu decomposition is determined at the intersection of the starting mass baseline with the tangent to the point of maximum inflection of the curve.<sup>122</sup> The onset temperature for degradation was found to be 220 °C for LiO<sup>t</sup>Bu, 240 °C for KO<sup>t</sup>Bu, and 250°C for NaO<sup>t</sup>Bu. The thermal stability of the *tert*-butoxides does not follow the usual trend related to increasing size of the alkali ion, and is instead due to the vapor-phase oligomeric structure. KO<sup>t</sup>Bu crystalizes as a tetrameric cubane-like structure, making the overall complex smaller and lighter than the NaO<sup>t</sup>Bu hexameric structure.<sup>93, 119-121</sup>

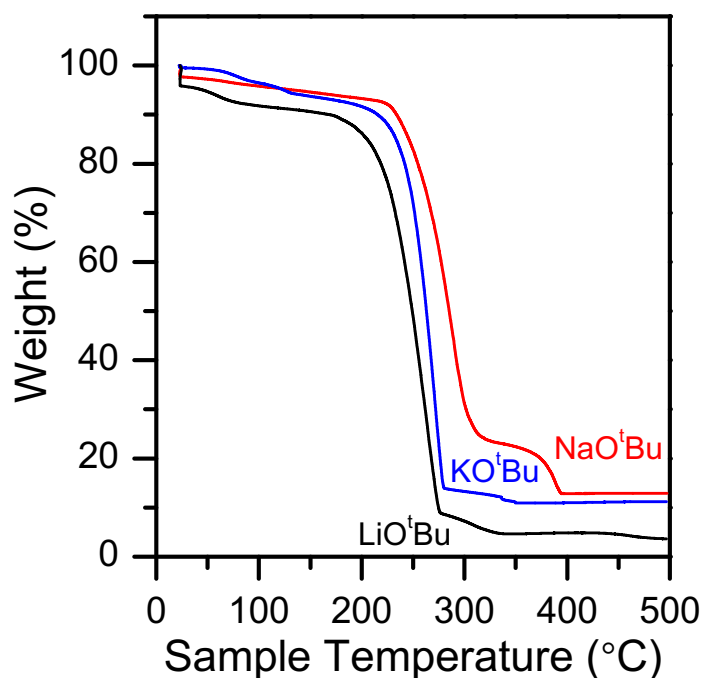


Figure 4.2. Thermogravimetric analysis of alkali *tert*-butoxides. AO<sup>t</sup>Bu's were heated at a rate of 5 °C/min under N<sub>2</sub> flow.

ALD process parameters were evaluated using *in-operando* SE, with the process results shown in Figure 4.3a-c. Figure 4.3a shows the growth per cycle (GPC) of the AO<sup>t</sup>Bu-DEPA processes as a function of temperature with a 20 s AO<sup>t</sup>Bu and 2 s DEPA pulse. All processes display features of a thermally activated process but are not ideal ALD reactions. The GPC of LiPON was measured to be ~0.9 Å/cycle at 300 °C, whereas the GPC of NaPON and KPON were only ~0.1 and ~0.2 Å/cycle, respectively, at this same temperature. Temperatures of 375 °C were

required for GPCs near 1 Å/cycle for NaPON and KPON. The NaPON and KPON processes have nearly identical temperature windows, both shifted ~50-100 °C higher than that of LiPON at comparable growth rates. Though, the GPC of KPON is slightly higher than NaPON at 275-325 °C, which is explained through the lower thermal stability of the KO<sup>t</sup>Bu precursor than NaO<sup>t</sup>Bu in Figure 4.2. The GPC as a function of AO<sup>t</sup>Bu dosage with a constant DEPA pulse of 2s is shown in Figure 4.3b. In the LiO<sup>t</sup>Bu case, the GPC increases from ~0.5 Å/cycle with a 5 s pulse and nearly saturates at ~0.9 Å/cycle above a 20s pulse. Similar trends are seen for NaO<sup>t</sup>Bu and KO<sup>t</sup>Bu. NaO<sup>t</sup>Bu shows a similar GPC of ~0.5 Å/cycle with a 5 s pulse, increasing to ~0.7 Å/cycle at 30s. The LiO<sup>t</sup>Bu pulse study took place at 300 °C, while the Na- and KO<sup>t</sup>Bu pulse studies were deposited at 375 °C. All three processes show linear, step-wise growth as a function of time or cycle number, as seen in Figure 4.3c.

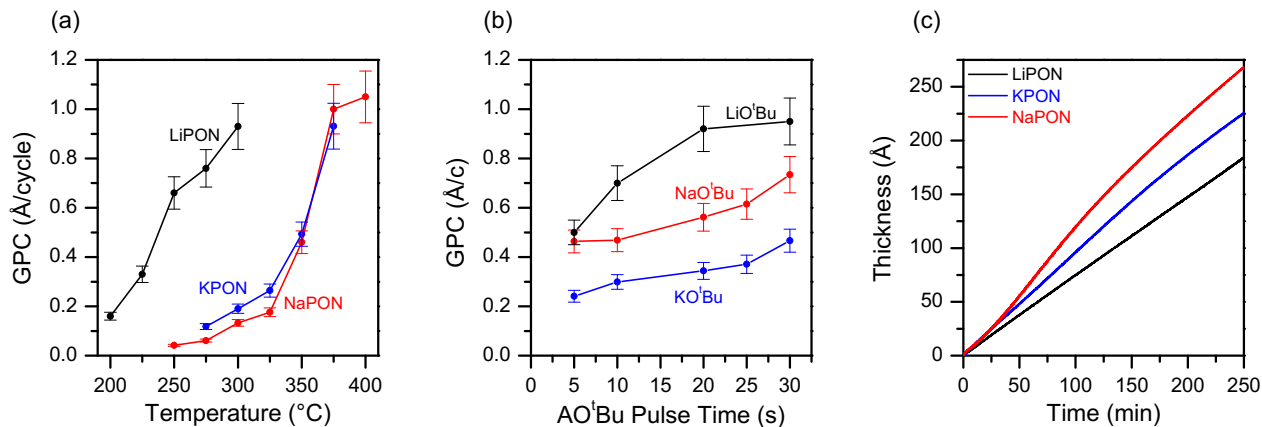


Figure 4.3. ALD process parameters of LiPON, NaPON, and KPON measured by in-operando spectroscopic ellipsometry. (a) Growth per cycle as a function of reactor temperature. (b) Growth per cycle as a function of AO<sup>t</sup>Bu pulse time. The LiO<sup>t</sup>Bu pulse study was deposited at 300 °C, while the NaO<sup>t</sup>Bu and KO<sup>t</sup>Bu pulse study were deposited at 375 °C. The DEPA pulse was fixed at 2 s. (c) Thickness profile for LiPON (deposited 250°C), NaPON (deposited 375°C), and KPON (deposited 375°C).

The three AO<sup>t</sup>Bu-DEPA processes for A = Li, Na, K explored here exhibit similar ALD growth characteristics, requiring relatively high temperatures for desirable growth rates (i.e., 1

Å/cycle). The higher temperatures required for comparable growth of NaPON/KPON as compared to LiPON are attributed to the larger atomic radius of the alkali ion and bulkier complexes formed in the gas phase.<sup>93, 119-121</sup> Though the ALD processes exhibit linear growth at fixed precursor doses, the lack of a clear temperature window suggests some CVD-like precursor decomposition contributing to enhanced growth rates. This behavior is more obvious in the case of NaPON and KPON, as the higher growth temperatures are above that of their respective AO<sup>t</sup>Bu's decomposition window as evidenced by the TGA (Figure 4.2). LiO<sup>t</sup>Bu displays the most desirable ALD characteristics of the AO<sup>t</sup>Bu's examined here, growing at lower temperatures, and exhibiting self-limiting reactions of each precursor pulse. Na- and KO<sup>t</sup>Bu have been demonstrated to be self-limiting with H<sub>2</sub>O in growing Na and K aluminates<sup>93</sup>, so perhaps introducing a H<sub>2</sub>O pulse between the AO<sup>t</sup>Bu and DEPA pulse would be worth investigating. Nonetheless, the thermal reactions of Li-, Na-, and KO<sup>t</sup>Bu with DEPA are desirable for highly chemically consistent ALD processes with fine tunability and extreme conformality.

#### **4.5. Chemical Structure**

We determine the structure of the alkali polyphosphazenes through XPS using *in-vacuo* transfer from the ALD chamber directly to the XPS chamber. Figure 4.4 shows the compositional information derived from XPS measurements for LiPON (Figure 4.4a), NaPON (Figure 4.4b), and KPON (Figure 4.4c) as a function of deposition temperature. LiPON exhibits a stable P/N ratio of 1 throughout the deposition temperature window, and the lowest total carbon content among the alkali polyphosphazenes, which decreases with increasing deposition temperature from 16.8% to 10% at the expense of Li and O. NaPON, shown in Figure 4.4b, has a remarkably stable chemistry throughout its temperature window from 300 °C to 375 °C, with a P/N ratio also near 1. However, unlike LiPON, NaPON shows significantly increased alkali metal content (~35% Na vs ~25% Li),

which occurs at the expense of decreased P and N content. Carbon contamination in NaPON is also higher than LiPON, with carbon levels at ~18% for all deposition temperatures. Figure 4.4c shows the chemistry of KPON from 275°C to 375°C. While there is phosphorous present in these films increasing with the temperature, there is negligible nitrogen incorporated, with a maximum of 2.2% nitrogen incorporated at 375°C, and the P/N ratio is far from one. With significantly more oxygen and carbon and less nitrogen than either LiPON or NaPON, this indicates scission of the amine ligand in the DEPA molecule during the deposition process, further indicating deviations from the ideal reaction mechanism. The resulting stoichiometry of the films are  $\text{Li}_2\text{PO}_2\text{NC}$ ,  $\text{Na}_4\text{PO}_3\text{NC}_2$ , and  $\text{K}_{5.2}\text{PO}_{6.3}\text{N}_{0.16}\text{C}_{4.7}$  respectively.

Figure 4.5 shows the high-resolution XPS regions for the constituent elements in LiPON, NaPON, and KPON. The alkali metal spectra (Figure 4.5a,f,k) all exhibit a single alkali-oxygen

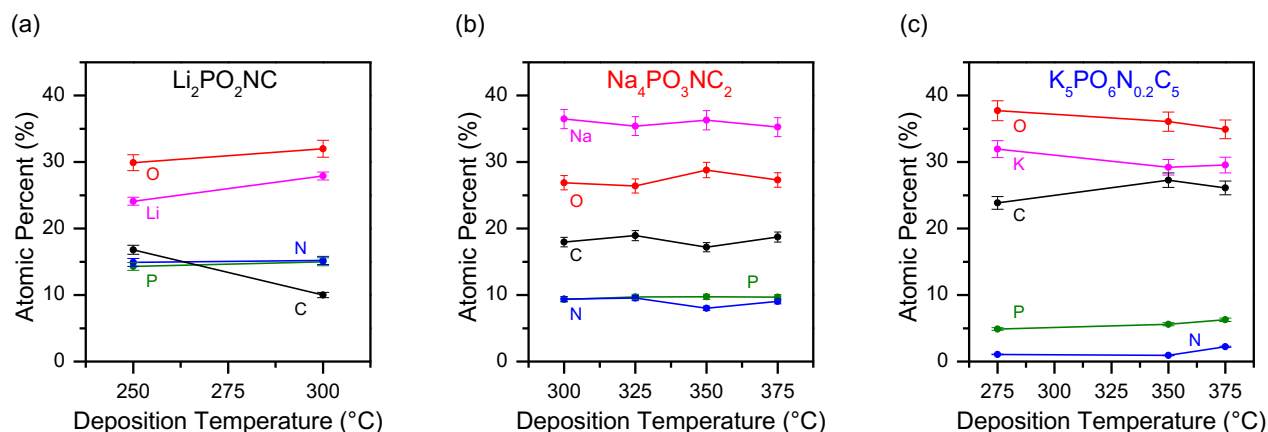


Figure 4.4. Elemental composition of (a) LiPON, (b) NaPON, and (c) KPON as a function of deposition temperature as determined by XPS without air-exposure of the films.

bonding state. The high-resolution spectra for LiPON displays a single peak in the P 2p region (Figure 4.5b), representing the backbone of the polyphosphazene chain. Two peaks are observed in the O 1s spectra (Figure 4.5c), with a major peak at 530.3 eV representing non-bridging oxygen ( $\text{P-O-Li}^+$ ) and a minor peak at 531.3 eV representing a bridging oxygen species ( $\text{P-O-P}$  or  $\text{P-O-}$

C). The N 1s region (Figure 4.5d) exhibits two peaks consistent with doubly coordinated nitrogen ( $N_d$ , P-N=P) and triply coordinated nitrogen ( $N_t$ , P-N<P<sub>2</sub>) bonding environments at 397.0 eV and 398.4 eV.  $N_t$  substitutes for  $N_d$  in the polyphosphazene chain, causing some deviation from the ideal -PO<sub>2</sub>N<sub>2</sub>- backbone. The C 1s region (Figure 4.5e) shows the presence of primarily hydrocarbon species (284.8 eV), with some -C-O- bonding (286.1 and 289.3 eV). This minor contribution is due to the incorporation of residual *tert*-butoxide/ethoxy ligands from the precursors. The ideal polyphosphazene would possess all  $N_d$  nitrogen and no carbon, but excluding carbon the resulting stoichiometry of Li<sub>2</sub>PO<sub>2</sub>N represents a lithium polyphosphazene.

The high-resolution XPS regions for NaPON (Figure 4.5f-j) indicate a strikingly similar material to LiPON. However, the NaPON exhibits increased P-N<P<sub>2</sub> content, resulting in a  $N_d/N_t$  ratio of 2.2 compared to 3.7 for LiPON. This indicates additional disorder in the ideal -PO<sub>2</sub>N<sub>2</sub>- backbone chains, and increased C-O bonding present in the films. The resolution of a distinct C-O peak is indistinguishable in the O 1s core-level spectra (Figure 5h), despite the O 1s region displaying a single sharp peak with a full-width-half-maximum (FWHM) of 1.24. This peak can therefore be attributed to contributions from Na<sup>+</sup>-O and C-O. It is possible that the close proximity of the Na KLL peak at 536.4 eV makes clear assignment of a distinct C-O peak difficult.

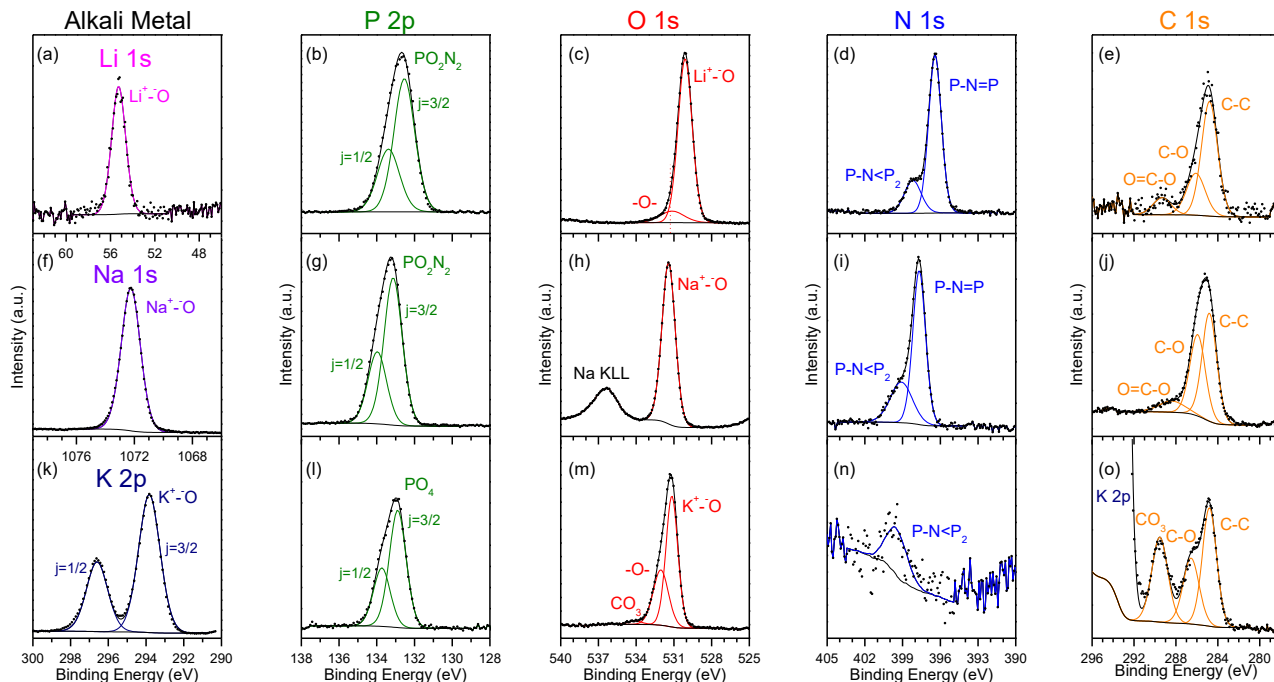


Figure 4.5. High-resolution core-level XPS spectra for the elements of interest of (a-e) LiPON deposited at 300 °C, (f-j) NaPON deposited at 350 °C, and (k-o) KPON deposited at 350 °C. All spectra are calibrated to the C-C peak at 284.8 eV.

Most interesting are the high resolution XPS figures for KPON, shown in Figure 4.5k-o, revealing a dramatically different material from both LiPON and NaPON. The P 2p region (Figure 4.5l) indicates a bonding environment consistent with PO<sub>4</sub> tetrahedra, indicating negligible P-N chain bonding. The O 1s spectra in Figure 4.5m indicates the presence of non-bridging oxygen at 531.2 eV (P-O-K<sup>+</sup>) and bridging oxygen at 532.0 eV (P-O-P, or P-O-C) typically observed in a phosphate. However, there is an additional peak indicative of carbonate formation due to the peak at 534.1 eV. The N 1s region, (Figure 4.5n) indicates negligible nitrogen (0.92%) in the films, with a single peak at 399.5 eV associated with N<sub>t</sub>, representing disorder of the PO<sub>4</sub> unit and an absence of P-N=P backbone chains. The C 1s spectra (Figure 4.5o) shows the presence of C-C and C-O bonds as in LiPON and NaPON, but also shows an additional peak at 289.6 eV, consistent with carbonate formation in the material.

As discussed previously, the ALD LiPON and NaPON films can both be classified as polyphosphazenes (N/P=1).<sup>35, 56</sup> Remarkably, while the NaPON process produces a film nearly structurally identical to the thermal LiPON ALD process, the resulting stoichiometry (Na<sub>4</sub>PO<sub>3</sub>N vs. Li<sub>2</sub>PO<sub>2</sub>N) does not indicate a simple replacement of Na with Li. Furthermore, when KO<sup>t</sup>Bu is reacted with DEPA in the same manner, similar growth characteristics are observed as in NaPON, but negligible nitrogen is incorporated into the film.

#### **4.6. Understanding the Surface Reaction**

*In-operando* quadrupole mass spectrometry (QMS) was employed to elucidate the surface reactions that enable the growth mechanisms of the Li/NaPON ALD processes, which can provide insight into and further unravel the film composition (XPS) and growth kinetics (SE) of the ALD APONs. As a case study, we first examined the LiPON ALD process to carefully characterize surface reactions before moving to the more complicated NaO<sup>t</sup>Bu/KO<sup>t</sup>Bu-DEPA processes. The mass spectra of the individual precursors in the ALD reactor are first examined, along with the surface decomposition of LiO<sup>t</sup>Bu, and then time-resolved QMS is used to infer the surface reaction mechanism.

##### **Mass spectra of LiO<sup>t</sup>Bu**

The mass spectrum of LiO<sup>t</sup>Bu was determined by QMS sampling of individual precursor pulses to understand their fragmentation/cracking pattern and thus distinguish from background species. Figure 4.6a shows the mass spectrum of LiO<sup>t</sup>Bu compared with that of the background Ar flow in the ALD reactor. Distinguishable peaks are observed over the Ar background at  $m/z = 15$  (CH<sub>3</sub><sup>+</sup>), 31 (CH<sub>3</sub>O<sup>+</sup>), 42 (C<sub>3</sub>H<sub>6</sub><sup>+</sup>/C<sub>2</sub>H<sub>2</sub>O<sup>+</sup>), and 59 (C<sub>3</sub>H<sub>7</sub>O<sup>+</sup>). These masses represent the cracking pattern of *tert*-butanol (*t*-BuOH), as supported by the close agreement with the mass spectrum for

*t*-BuOH in the NIST reference database.<sup>123</sup> The fragmentation of *t*-BuOH in the mass spectrometer proceeds by the pathways described in Figure 4.6b, resulting in the ion fragments at  $m/z$  15, 31, 43, and 59. The peak at  $m/z = 42$  is most likely  $C_3H_6^+$ , which appears from deprotonation of the  $C_3H_7$  ( $m/z = 43$ ) fragment. Due to their higher intensities,  $m/z = 31$  ( $CH_3O^+$ ) and 59 ( $C_3H_7O^+$ ) will be used to track LiO'Bu during the ALD process.

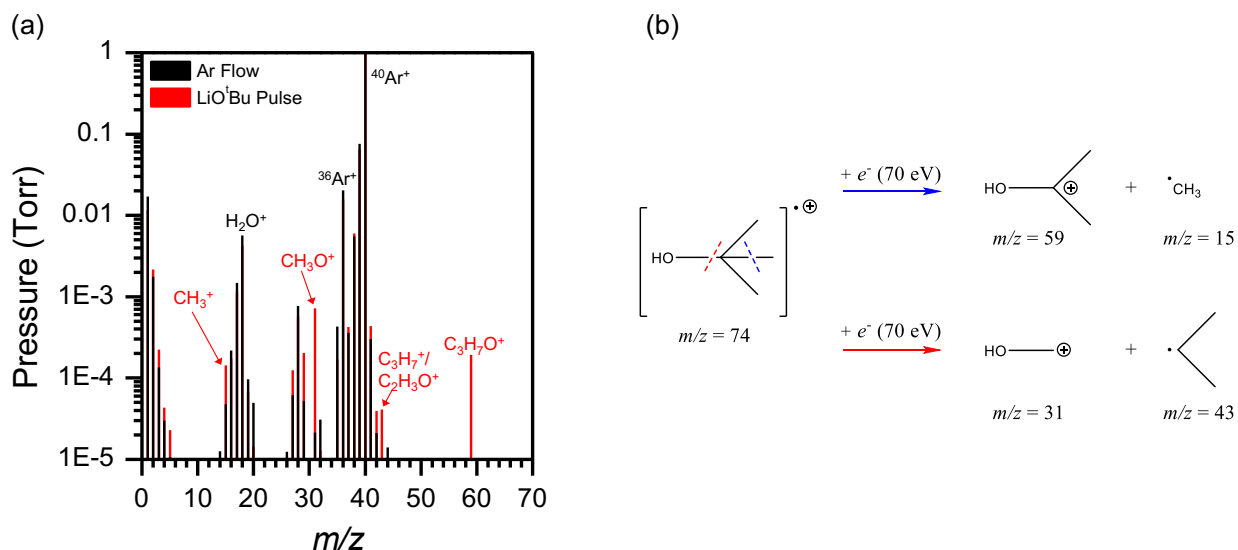


Figure 4.6. (a) Fragmentation pattern of LiO'Bu measured by in-operando mass spectrometry in the ALD reactor. The fragmentation pattern was obtained during precursor dose in the reactor with Ar flow and is overlaid with the background spectra of the reactor under Ar flow. (b) proposed fragmentation patterns of *t*-BuOH in the QMS.

The mass spectrum for LiO'Bu did not display direct fragmentations of LiO'Bu, but instead those representing *t*-BuOH. This was expected, as Hornsveld et al.<sup>124</sup> also observed this in their QMS study of a  $Li_2CO_3$  ALD process using LiO'Bu as the lithium source. The mass spectrum of pure LiO'Bu is not available in the NIST Standard Reference Database<sup>123</sup>, however direct vapor phase measurements of LiO'Bu have been reported using time of flight mass spectrometry.<sup>125, 126</sup> These results showed a fragmentation pattern of peaks corresponding to  $Li_nR_{n-1}^+$  species ( $R = t$ -BuO), evidencing that LiO'Bu forms a hexamer in the gas phase. However, such high masses are outside the detectable range of our ALD coupled QMS (1-300 amu) used in this study, and the high reactor pressure and small precursor dose lessens sensitivity. For instance, the base peak of

the LiO<sup>t</sup>Bu hexamer, [Li<sub>6</sub>(*t*-BuO)<sub>5</sub>]<sup>+</sup> has a *m/z* of 407. Therefore, while direct observation of LiO<sup>t</sup>Bu is not possible, its presence is monitored through *tert*-butanol.

### Surface Decomposition of LiO<sup>t</sup>Bu

To complement QMS measurements, XPS analysis was performed on a Si wafer subjected to LiO<sup>t</sup>Bu pulses at 250 °C. High-resolution scans of the Li 1s and O1s are shown in Figure 4.7. Deconvolution of the XPS spectra shows 2 peaks of equal atomic ratios corresponding to a 3:1 ratio of Li<sub>2</sub>O:LiOH. The overall film composition was Li<sub>1.6</sub>O with negligible carbon content (~0.6%), suggesting that LiO<sup>t</sup>Bu is depositing as mixed Li<sub>2</sub>O/LiOH on the Si surface. This finding is not in line with the proposed chemisorption of LiO<sup>t</sup>Bu during its initial pulse in Li<sub>2</sub>CO<sub>3</sub> and LiOH ALD processes by Cavanagh et al.<sup>127</sup> Chemisorption suggests that LiO<sup>t</sup>Bu remains intact on the surface and does not initially release volatile reaction byproducts such as *t*-BuOH until a subsequent H<sub>2</sub>O dose occurs. Hornsveld et al.<sup>124</sup> reported QMS data supporting such chemisorption behavior, in which the signal of *t*-BuOH (*m/z* 59) is negligible during LiO<sup>t</sup>Bu dose

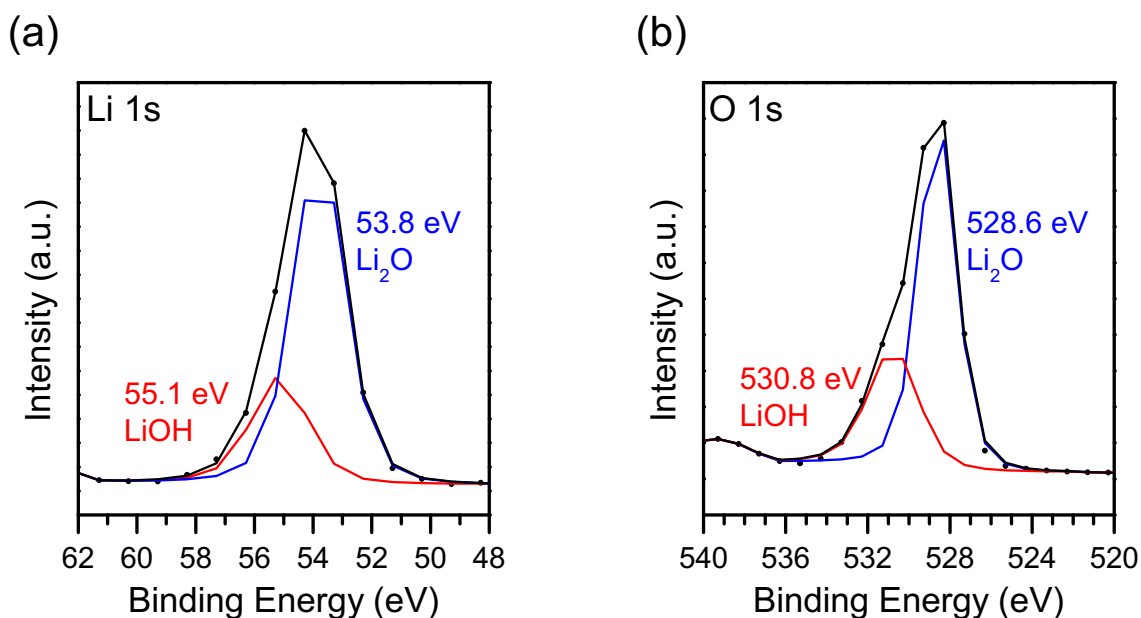


Figure 4.7. XPS Spectra of LiO<sup>t</sup>Bu pulsed on a Si wafer at 240 °C. (a) Li 1s and (b) O 1s high-resolution core-level spectra.

compared to a spike observed during the subsequent H<sub>2</sub>O pulse. In our work, a significant increase in  $m/z$  59 is

observed with repeated LiO<sup>t</sup>Bu pulses (Figure 4.8). This discrepancy can be attributed to the lower reactor temperature of 150 °C used by Hornsveld and colleagues, compared to 250 °C in this work. Based off our measurements, we can conclude that LiO<sup>t</sup>Bu readily decomposes to Li<sub>2</sub>O and LiOH at our ALD temperatures. This behavior is expected based on the TGA of LiO<sup>t</sup>Bu shown in Figure 4.2. This also supports the non-self-limiting nature observed for the AO<sup>t</sup>Bu's in Figure 4.3, as the GPC continues to increase with longer AO<sup>t</sup>Bu pulses due to prolonged thermal decomposition on the surface.

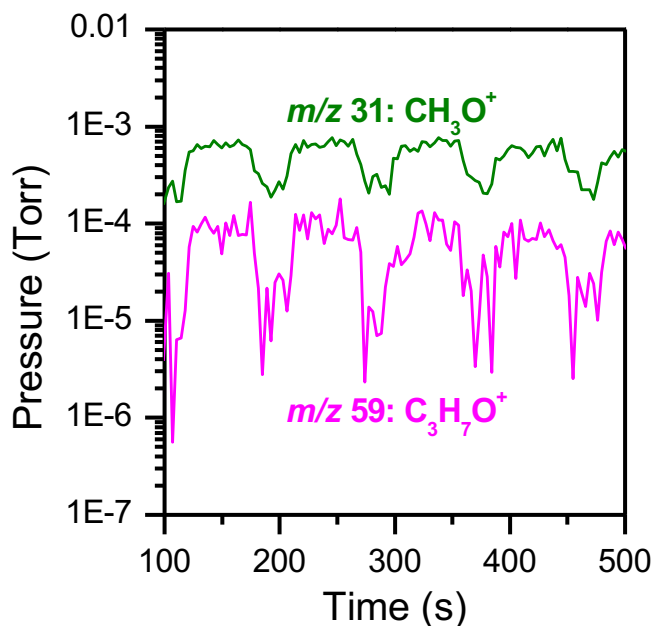


Figure 4.8. Time-resolved mass spectra of repetitive 60 s LiOtBu pulses with 30 s of purge time in-between.

### Mass Spectra of DEPA

In Figure 4.9a, the mass spectrum of DEPA shows distinguishable peaks at  $m/z = 16$  ( $\text{O}^+$ ), 17 ( $\text{OH}^+/\text{NH}_2^+$ ), 27 ( $\text{C}_2\text{H}_3^+$ ), 29 ( $\text{C}_2\text{H}_5^+/\text{CHO}^+$ ), and 45 ( $\text{C}_2\text{H}_5\text{O}^+$ ). These peaks are in agreement with the mass spectrum of DEPA in the NIST Standard Reference Database<sup>123</sup>, differing slightly

in intensity distribution. The mass spectrum of DEPA in the NIST database shows the base peak at  $m/z = 80$ , then, in descending order, at  $m/z = 98$ , 126, 81, 108, 109, 29, 27, 45, 124. However, we were unable to distinguish masses above 70 from the background noise with the scan settings during a DEPA pulse into the ALD reactor. We did however observe all of these masses when DEPA was sampled into the QMS directly from a heated cylinder, bypassing the ALD reactor

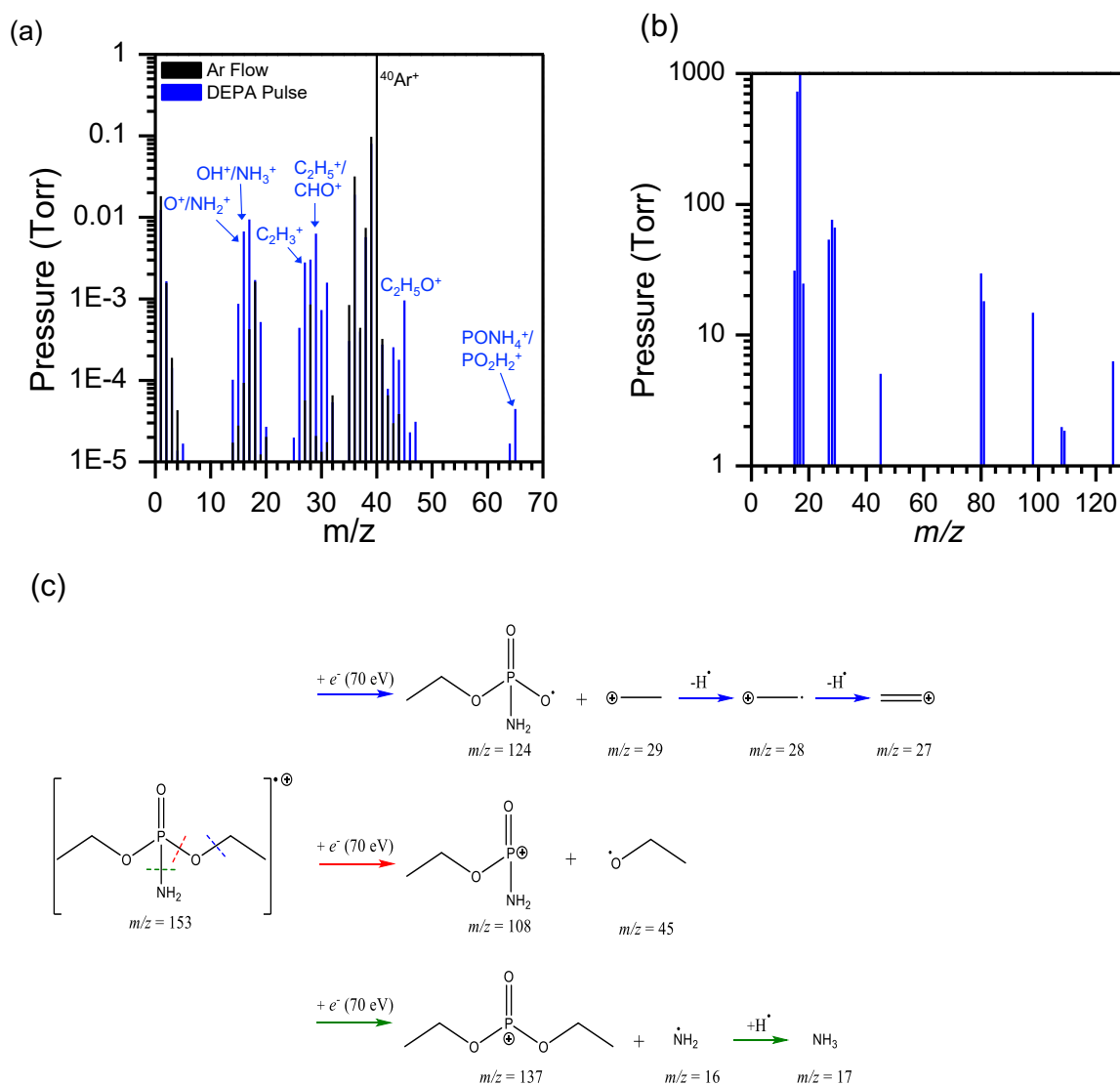


Figure 4.9. (a) Fragmentation pattern of DEPA measured by in-operando mass spectrometry in the ALD reactor. The fragmentation pattern was obtained during precursor dose in the reactor with Ar flow and is overlaid with the background spectra of the reactor under Ar flow. (b) Fragmentation pattern of DEPA measured directly from a cylinder heated to 115 °C. (c) Proposed fragmentation patterns of DEPA in the QMS.

(Figure 4.9b). In Figure 4.9b, peaks at  $m/z = 16, 17, 18, 27, 28,$  and  $29$  are still the most intense, likely indicating a boost in signal from background  $H_2O$  and  $N_2$  in the lines. The molecular fragmentation pathway of DEPA is described in Figure 4.9c. Variations in ion fragmentations arise from the electron bombardment process, e.g.  $[M-CH_3CH_2]^{*+} = 124$  vs.  $[M-CHCH_2]^{*+} = 126$ . The peaks at  $m/z = 28$  and  $45$  will be used to track DEPA during the ALD process due to higher intensity and distinguishability from  $LiO^tBu$  fragments and background species.

### Time-resolved Mass Spectra of LiPON Process.

With the fragmentation patterns of both precursors well understood, a modified ALD recipe was developed for *in-operando* monitoring of the LiPON process via QMS. The recipe included modified pulse/purge times to assist in distinguishing between reactants/products. The modified recipe is described in Table 4.1 below.

*Table 4.1. Modified ALD recipe for in-operando QMS sampling.*

	Precursor	Pulse Time (s)	Purge Time (s)	Cycles
<i>Step 1a</i>	<i>LiO<sup>t</sup>Bu</i>	15	5	1
<i>Step 1b</i>	<i>LiO<sup>t</sup>Bu</i>	5	5	6
<i>Step 1c</i>	<i>LiO<sup>t</sup>Bu</i>	2	4	3
<i>Step 2</i>	<i>DEPA</i>	8	5	2
<i>Step 3a</i>	<i>LiO<sup>t</sup>Bu</i>	15	5	2
<i>Step 3b</i>	<i>LiO<sup>t</sup>Bu</i>	2	4	3
<i>Step 4a</i>	<i>DEPA</i>	2	4	1
<i>Step 4b</i>	<i>DEPA</i>	2	6	4

In step 1, a long  $LiO^tBu$  pulse is introduced to create a stable reference measurement, followed by shorter repetitive pulses to ensure saturation of the reactive surface and dose stabilization through the needle valve to the QMS. In step 2, two long DEPA pulses are introduced to fully react with the surface and generate a high concentration of byproducts. In step 3, multiple  $LiO^tBu$  pulses are introduced to again ensure that the dose is large enough to fully saturate the

surface. In Step 4, DEPA is pulsed with shorter purge times to observe the reaction byproduct, followed by 4 pulses with slightly longer purge times to determine if the surface is saturated with DEPA molecules. This modified ALD recipe is helpful in distinguishing between reactants/products detected in the QMS. Steps 1-4 represent 1 complete cycle of the modified ALD process. Two full cycles are shown in Figure 4.10.

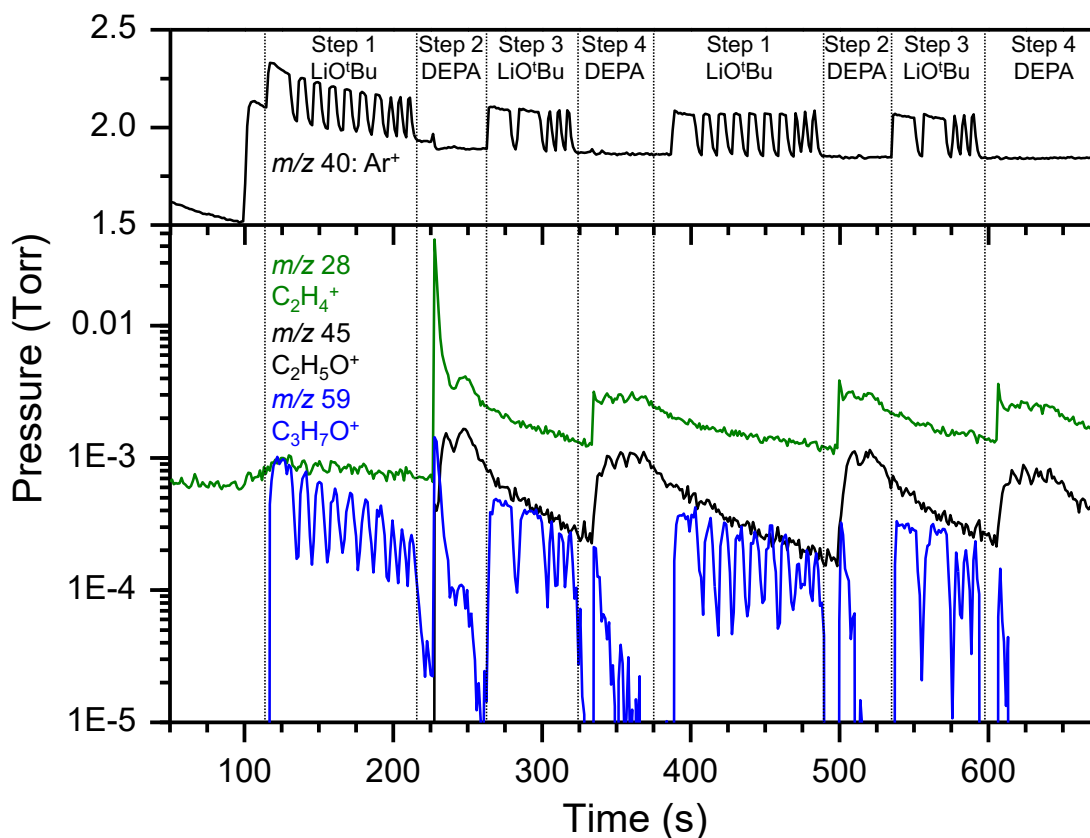


Figure 4.10. Time-resolved mass spectra for 2 complete cycles of the modified LiPON ALD process at 250 °C. Fragments are shown for  $m/z = 40$  ( $Ar^+$ ), 28 ( $C_2H_4^+$ , DEPA), 45 ( $C_2H_5O^+$ , DEPA), and 59 ( $C_3H_7O^+$ , LiO<sup>t</sup>Bu).

Figure 4.10 shows the time resolved QMS data for this modified ALD process. Based on the experiments discussed in sections 5.1 and 5.3,  $m/z$  28 ( $C_2H_4^+$ ) and 45 ( $C_2H_5O^+$ ) were chosen to track DEPA,  $m/z$  59 ( $C_3H_7O^+$ ) was used to track LiO<sup>t</sup>Bu, and  $m/z$  40 ( $Ar^+$ ) was used for reference. In step 1, ion fragment 59 tracks with the Ar peak at  $m/z$  40, as Ar is used to aid in the delivery of

low vapor pressure LiO<sup>t</sup>Bu to the reactor. Following The LiO<sup>t</sup>Bu dose in step 1,  $m/z$  59 signal decreases to  $\sim 2 \times 10^{-5}$  Torr until the leading DEPA pulse in step 2. In the first DEPA pulse of step 2,  $m/z$  28 and 59 see an immediate sharp increase, whereas  $m/z$  45 increases with a delayed response. The second DEPA pulse shows a small uptick in the decreasing signals of  $m/z$  28 and 59, and an additional peak at  $m/z$  45. In step 3, DEPA contributions continue to decrease, with increases in  $m/z$  59 at each LiO<sup>t</sup>Bu pulse. In step 4, the first DEPA pulse shows a large increase in  $m/z$  28 and 45, with an additional sharp increase in  $m/z$  59. The subsequent DEPA pulses show little or no contribution of  $m/z$  59 and saturation of DEPA in the reactor. Step 2 is the most insightful mechanistically to the ALD process and clearly shows when DEPA is pulsed, *t*-BuOH ( $m/z = 59$ ) is immediately released, followed by the release of ethanol (EtOH,  $m/z$  45).

#### **4.7. Proposed Reaction Mechanism**

Given the chemical composition of the materials (Section 5) and the detailed QMS studies (Section 6), we propose the following mechanism for the LiPON ALD process, shown in Figure 4.11. Upon initial pulse of LiO<sup>t</sup>Bu, OH surface species are replaced with O-Li, forming a surface lithium alkoxide and releasing *t*-BuOH. The remaining OH groups on the surface represent the incomplete replacement of the O-H bond with O-Li. Li<sub>2</sub>O is shown to represent some thermal decomposition of LiO<sup>t</sup>Bu. For the following reaction steps shown, we assume all LiO<sup>t</sup>Bu reacted in the first step or was otherwise purged out of the reactor. In the subsequent DEPA pulse, the DEPA molecule remains mostly intact, binding to the Li-O surface and releasing *t*-BuOH ( $m/z$  59) forming a Li-O-(PO<sub>2</sub>NH<sub>2</sub>CH<sub>2</sub>CH<sub>3</sub>) bond through the release of ethane ( $m/z$  28) from DEPA. A surface mediated polymerization then occurs where neighboring P-N bonds link, releasing ethanol ( $m/z$  45) as a byproduct. In the following LiO<sup>t</sup>Bu pulse, N from the surface interacts with LiO<sup>t</sup>Bu, causing the tert-butoxide to scavenge the H atom in the amine group, leaving as *t*-BuOH ( $m/z$  59).

The P=N bond is then formed by a resonance rearrangement from the P=O bond to form P-O-Li and movement of electron density from Li-N to N-O. This reaction sequence results in the polyphosphazene chain-like structure  $\text{Li}_2\text{PO}_2\text{N}$ . We note this is an idealized reaction mechanism to form the pure  $\text{Li}_2\text{PO}_2\text{N}$  polyphosphazene. The true ALD reaction will involve some thermal decomposition of precursors and side reactions resulting in incomplete surface binding/release of precursor ligands and the excess carbon content observed in the film. These initial experiments provide evidence for a plausible reaction mechanism.

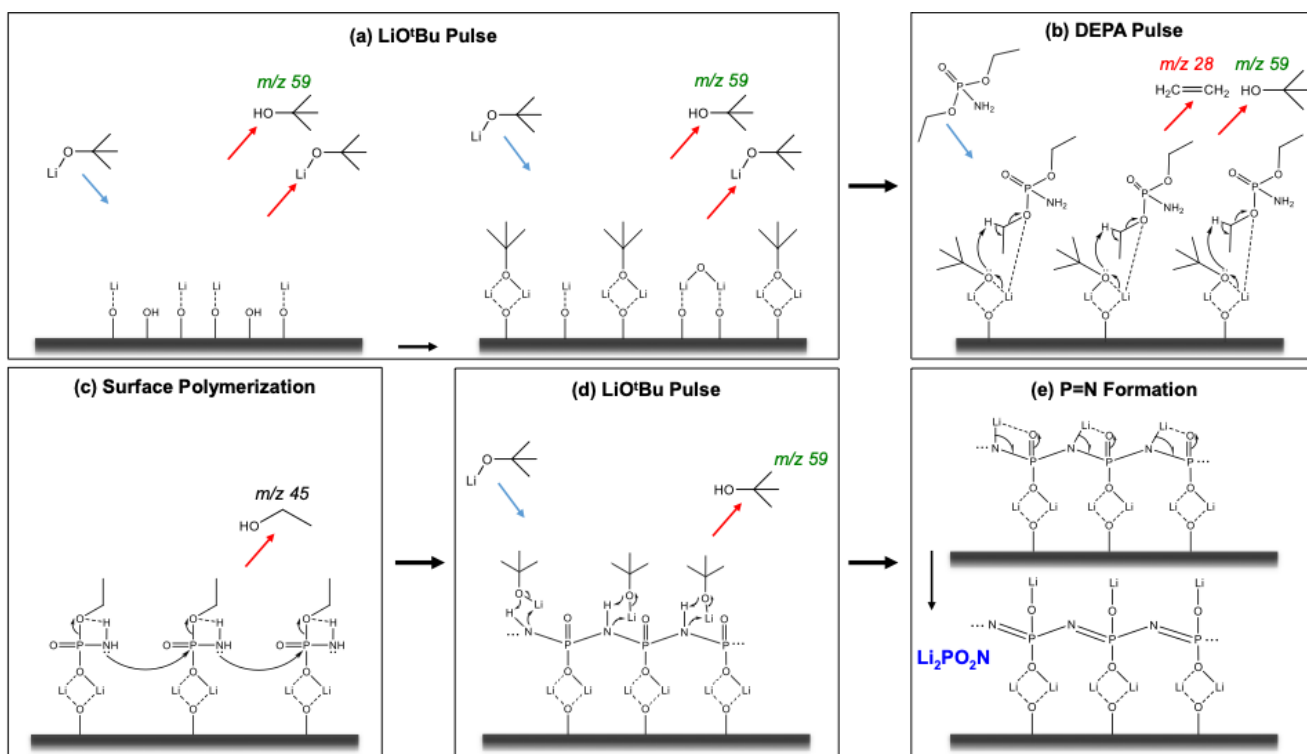


Figure 4.11. Proposed Thermal LiPON Reaction Mechanism. The reaction mechanism is based on in-situ mass spectrometry measurements of the ALD process. (a)  $\text{LiO}^t\text{Bu}$  chemisorbs on hydroxylated surface. (b) DEPA reacts with the lithium alkoxide surface to release  $\text{C}_2\text{H}_4$  and  $\text{C}(\text{CH}_3)_3\text{OH}$ . (c) Linking of the surface species occurs through the P-N bonds with the loss of  $\text{CH}_3\text{CH}_2\text{O}$ . (d)  $\text{LiO}^t\text{Bu}$  interacts with the N atoms in the chain and leads to the resonance rearrangement to form P=N. (e) The alternating P=N bond in the chain forms the basis for the polyphosphazene  $\text{Li}_2\text{PO}_2\text{N}$  structure.

## 4.8. Electrochemistry

The alkali PONs discussed herein are functional ionic materials, meaning they allow ion transport while offering negligible electronic conductivity. The most important metrics for SSE applications are the ionic conductivity and activation energy. Devices for testing were fabricated by depositing the ALD APON between metal electrodes in a metal-electrolyte-metal (MEM) stack. The ionic transport properties of LiPON, NaPON, and KPON were measured through electrochemical impedance spectroscopy (EIS). Activation energy for ion transport in LiPON and NaPON is determined from temperature-based measurements. Electrochemical analysis is presented for all APONs that were exposed to air and also for pristine MEM devices fabricated and tested in a custom UHV-Ar glovebox cluster system.

EIS measurements for all three materials are shown as Nyquist plots in Figure 4.12. Test devices were prepared by depositing the APON between Pt blocking electrodes, requiring brief air exposure for deposition of the top Pt contact. The EIS spectra of LiPON and NaPON show similar behavior with a semicircular arc at high-mid frequencies and an increase in the imaginary impedance component at low frequencies. The semicircular arc is attributed to ion transport through the electrolyte and is assigned two parallel-resistor constant phase element (CPE) components in the equivalent circuit used to model the curves (Figure 4.12a inset). The two CPEs represent bulk ionic conduction of the APON film ( $CPE_b$ ), and ion conduction through an air-reacted interphase layer ( $CPE_r$ ) formed at the surface. The sharp increase in the low frequency regime is modeled by a CPE in series ( $CPE_w$ ) with the  $CPE_b$  and  $CPE_r$  to account for Warburg diffusion in the blocking electrode. We use this equivalent circuit model to calculate the total resistance ( $R_b + R_r$ ) of the film, from which we determine its ionic conductivity. LiPON exhibited an ionic conductivity of  $1.6 \times 10^{-7}$  S/cm at 35 °C, 2 orders of magnitude higher than that of NaPON

at 25 °C ( $1.3 \times 10^{-9}$  S/cm). The EIS spectra of the K substituted version differs in that it shows only two semicircles with no Warburg-like diffusion. As in the prior cases, this curve is modeled by two CPE components,  $CPE_b$  and  $CPE_r$ , but does not include a Warburg element. Interestingly, the ionic conductivity of KPON was measured to be  $7.4 \times 10^{-9}$  S/cm at 25 °C. This is higher than that of NaPON at room temperature, despite the larger ionic radius of  $K^+$  than  $Na^+$ . The shape of the EIS curve of KPON suggests that the material acts as an electrostatic capacitor. It is unclear why KPON does not display any semi-infinite diffusion and surprisingly displays a lower overall resistance than NaPON. The different ionic behavior of KPON than LiPON and NaPON supports its deviation in structure from the Li and Na analogues. EIS testing at lower frequencies may be required to gain a better understanding of the ionic transport properties of KPON, as the measurements in Figure 4.12 were recorded with a cutoff frequency of 500 mHz.

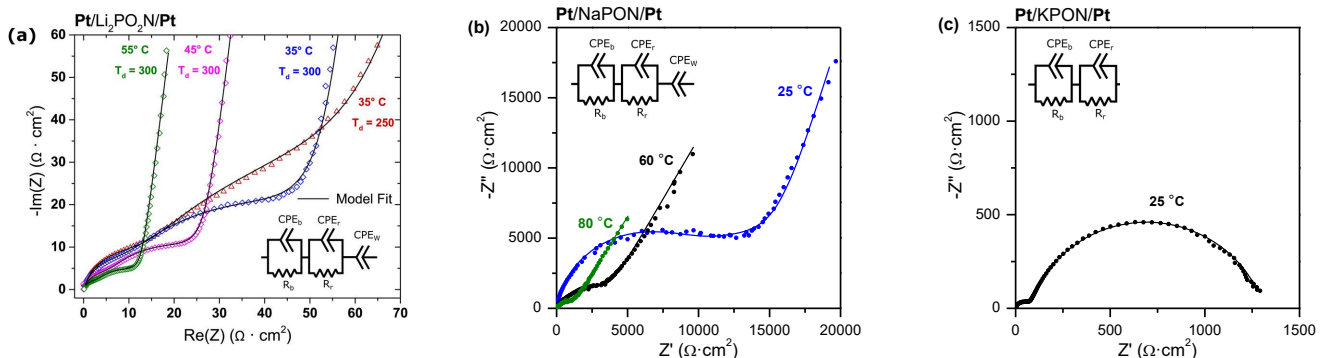


Figure 4.12. EIS measurements of APONs. (a) Nyquist plots for Pt/80 nm LiPON/Pt devices measured between 35 - 55 °C. LiPON was deposited at 300°C and 250 °C (red curve). Adapted from ref<sup>35</sup> Copyright 2017 American Chemical Society. (b) Nyquist plots for Pt/137 nm NaPON/Pt devices measured between 25-80 °C. NaPON was deposited at 375 °C. Adapted from ref<sup>6</sup> Copyright 2020 American Chemical Society. (c) Nyquist plot for Pt/97 nm KPON/Pt devices measured at 25 °C. KPON was deposited at 375 °C. All samples were briefly exposed to air for deposition of the top Pt metal blocking electrodes.

To consider the true ionic properties of the APON SSE films without the effects of an impeding interphase layer, measurements of LiPON and NaPON were also conducted while eliminating air exposure. Figure 4.13a-b shows temperature based EIS measurements of pristine LiPON and NaPON. Measurements on Pt/LiPON/Li reveal an increased conductivity of  $3.7 \times 10^{-7}$  S/cm at room temperature. A similar trend is observed for pristine NaPON, exhibiting an increase

in ionic conductivity to  $1.0 \times 10^{-7}$  S/cm at room temperature, and up to  $2.5 \times 10^{-6}$  S/cm at 80 °C. The Arrhenius plot in Figure 4.13c for LiPON and Figure 4.13d for NaPON show that the activation energies for air-exposed and pristine samples are nearly identical for both LiPON and NaPON. The activation energy for air-exposed LiPON and NaPON is 0.64 eV and 0.66 eV, respectively. The activation energy of pristine LiPON and NaPON is 0.55 eV and 0.53 eV, respectively. The lower activation energy associated with pristine samples clearly indicates the

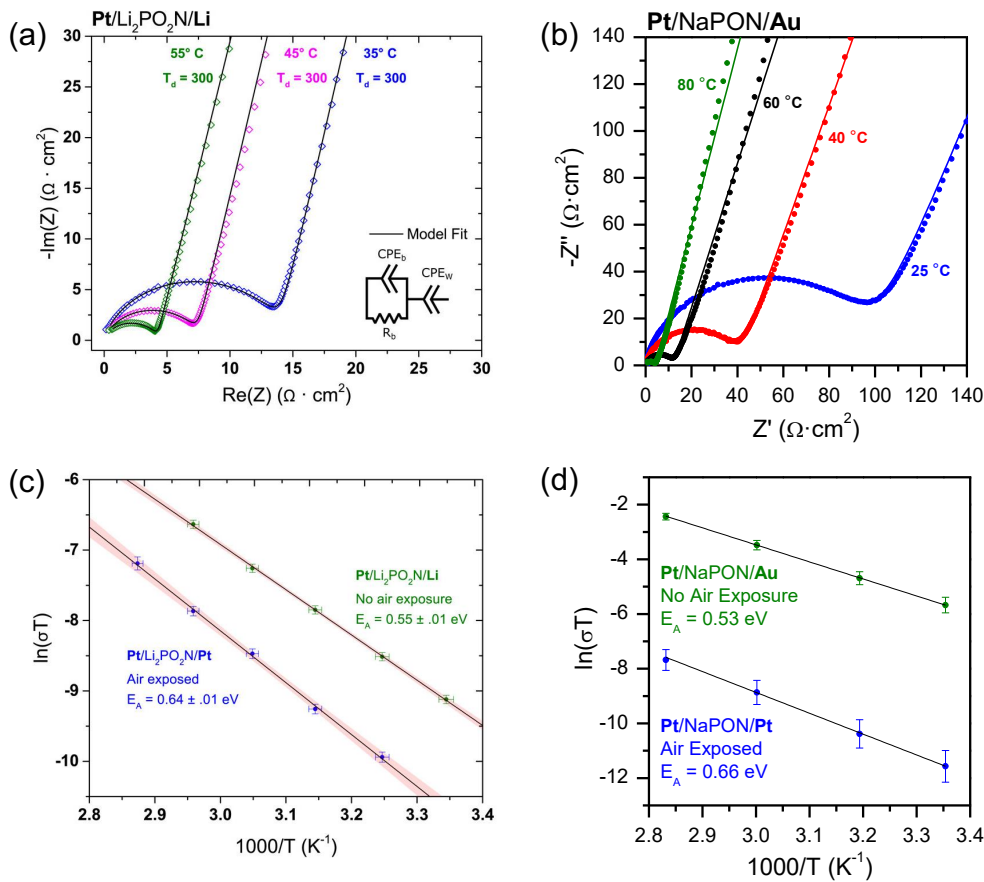


Figure 4.13. Transport properties of LiPON and NaPON without air exposure. (a) Nyquist plots for Li/80 nm LiPON/Pt measured between 35-55 °C. (b) Nyquist plot for Au/137 nm NaPON/Pt measured between 25-80 °C. (c) Arrhenius plots for air-exposed and pristine LiPON films showing activation energies of the films. (d) Arrhenius plots for air-exposed and pristine NaPON films showing activation energies of the films. (a) and (c) adapted from ref<sup>35</sup> Copyright 2017 American Chemical Society. (b) and (d) adapted from ref<sup>56</sup> Copyright 2020 American Chemical Society

removal of an resistive interphase layer as the energy barrier for ion migration is lowered. The similar activation energies additionally identify that the energy barrier for  $\text{Li}^+/\text{Na}^+$  migration relies primarily on the amorphous phosphorus oxynitride network, i.e. the energy barrier for ionic movement is independent of the ionic species but not the overall chemical structure.

## 4.9. Discussion

Through additional *in-operando* QMS studies we hope to explain differences in the LiPON/NaPON/KPON ALD processes to better understand the surface-mediated reactions of  $\text{AO}^t\text{Bu}$ 's and DEPA. Initial QMS data of  $\text{NaO}^t\text{Bu}$  pulsed into the ALD reactor indicates that  $\text{NaO}^t\text{Bu}$  is detectable in the QMS as *t*-BuOH, just as the case for  $\text{LiO}^t\text{Bu}$  (Figure 4.14). The similar

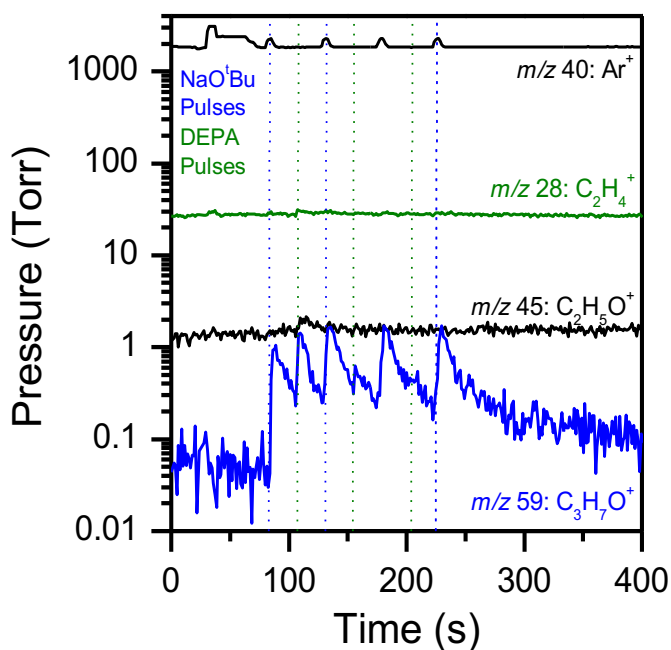


Figure 4.14. Mass spectra of the  $\text{NaOtBu}$ -DEPA NaPON process.  $\text{NaOtBu}$  was pulsed for 5 s and DEPA for 2 s, with 20s purges in between each pulse.

cracking pattern in the QMS and phosphazene structure indicated by XPS ( $\text{P}:\text{N}=1$ ) allow us to speculate that ALD NaPON proceeds in a similar reaction mechanism to LiPON, though a more thorough study would be required to confirm this assumption. The resulting films possess

differences in stoichiometry,  $\text{Li}_2\text{PO}_2\text{NC}$  vs.  $\text{Na}_4\text{PO}_3\text{NC}_2$ . This is not surprising given the higher deposition temperatures of NaPON required for comparable growth to LiPON, i.e. 375 °C vs. 300 °C. The higher process temperature provides opportunity for increased thermal decomposition of the  $\text{NaO}^t\text{Bu}$  precursor, thus producing more incorporated *tert*-butoxy and ethoxy ligands in the film.

The KPON process presents a completely different reaction mechanism, as little nitrogen (2.2% max.) is incorporated into the film. The composition of the film is instead found to be a ratio of  $\text{K}_3\text{PO}_4/\text{K}_2\text{CO}_3/\text{KO}^t\text{Bu}$ . The different reactivity towards DEPA is attributed to the  $\text{KO}^t\text{Bu}$  precursor.  $\text{KO}^t\text{Bu}$  is bulkier and a stronger base than its Li and Na counterparts. The increased steric hindrance is believed to play a role in the different reactivity of  $\text{KO}^t\text{Bu}$  towards DEPA. *In-operando* QMS of  $\text{KO}^t\text{Bu}$ -DEPA would aid in understanding the reaction mechanism by distinguishing different species desorbing from the surface than the LiPON and NaPON processes. Furthermore, in an attempt to develop an ALD process for a fully nitrogenated KPON film, alternative reaction schemes should be performed. For instance, we have had success growing LiPON and NaPON plasma-based ALD processes<sup>36</sup>, which are essentially  $\text{Li}_3\text{PO}_4/\text{Na}_3\text{PO}_4$  processes with an added nitrogen plasma pulse to dope the alkali phosphate. The base potassium phosphate has not been demonstrated but is believed to be plausible, based on the simple reaction sequence of  $\text{AO}^t\text{Bu}-\text{H}_2\text{O}-\text{TMP}$ . In addition, the large presence of phosphate in the potassium film deposited herein is promising. The addition of  $\text{N}_2$  plasma to a  $\text{K}_3\text{PO}_4$  process may be able to overcome the steric energy barrier to incorporate nitrogen into the film. If this proves unsuccessful, further novel precursors are worth exploring.

Alkali PONs are advantageous SSE materials due to their amorphous glassy structure. Crystalline SSEs have been developed by ALD but require high temperature annealing thus

limiting material and application compatibility, in addition to introducing significant thermal stress. Of amorphous ALD SSEs, only  $\text{Li}_x\text{SiO}$ <sup>128</sup> and  $\text{Li}_3\text{BO}_3\text{-Li}_2\text{CO}_3$  (LBCO)<sup>129</sup> possess a higher room temperature ionic conductivity than ALD LiPON, exhibiting ionic conductivities of 1.5 and  $2.2 \times 10^{-6}$  S/cm, respectively. Looking forward, thin-film SSEs with higher ionic conductivities are certainly desirable. Building upon the LBCO process, replacing the  $\text{Li}_2\text{CO}_3$  component with  $\text{Li}_3\text{N}$  or  $\text{Li}_3\text{PO}_4$  may improve the ionic conductivity as lithium phosphate and nitride have a higher ionic conductivity than lithium carbonate. Additionally, substituting  $\text{Li}_x\text{SiO}$  with N to make a  $\text{Li}_x\text{SiON}$  glassy material may improve the ionic conductivity in a similar manner to LiPON, in which the substituting nitrogen for oxygen is known to decrease electrostatic interactions with Li in LiPON films and improve the  $\text{Li}^+$  transport. For beyond LIBs, NaPON is a promising SSE for Na ion batteries. The ionic conductivity reported above for NaPON is on par with that of LiPON. Similar to the other glassy materials for Li ion batteries, the Na-based analogues are worth exploring due to the similar chemistries. In the processes of  $\text{Li}_x\text{SiO}$  and LBCO,  $\text{LiO}^t\text{Bu}$  is used as the Li source, so substitution with  $\text{NaO}^t\text{Bu}$  is worth implementing to synthesize the Na analogues. Although it should be mentioned, as evidenced in this work, the processes are not an exact one-for-one exchange of  $\text{NaO}^t\text{Bu}$  for  $\text{LiO}^t\text{Bu}$ , or more clearly represented in the case of  $\text{KO}^t\text{Bu}$ .

While we have worked on a few of the alkali polyphosphazenes through ALD, there remains a vast expanse of materials unexplored. Interesting possibilities building upon this work include organic linked phosphazene chains, mixed alkali ion conductors, and divalent alkaline earth phosphazenes. By replacing the alkali cations with any of the enumerable organic ligand groups, a wide range of materials with an equally wide range of potential properties remain undiscovered. Additionally, this work calls for additional ALD work on mixed alkali metal conductors. This could be possible through super cycles of processes for the alkali

oxides/oxytrinitrides/nitrides/phosphates. Sonstebly et al.<sup>130, 131</sup> have demonstrated a mixed KNbO<sub>3</sub>-NaNbO<sub>3</sub> using KO<sup>t</sup>Bu and NaO<sup>t</sup>Bu as precursors. It was found that the K:Na ratio was tunable to 1% by substituting in NaO<sup>t</sup>Bu for KO<sup>t</sup>Bu in the KNbO<sub>3</sub> process. Following a similar approach may be possible for the mixing of LiPON/NaPON processes described herein.

The development of divalent ionic conductors looks to be more challenging. A MgP<sub>x</sub>O<sub>y</sub> ALD SSE has been reported, but exhibited non-ideal electrochemical performance with a temperature of 500 °C required to obtain an ionic conductivity of  $1.6 \times 10^{-7}$  S/cm and high activation energy of 1.37 eV.<sup>132</sup> In terms of Ca ALD, a Ca phosphate glass resembling a hydroxyapatite (Ca<sub>10</sub>(PO<sub>4</sub>)<sub>6</sub>) structure has been demonstrated, but no ionic properties were reported.<sup>133</sup> Unlike the alkali metal precursors, di-*tert*-butoxides are not ideal ALD precursors. Ca and Mg based cyclopentadienyl (Cp) and β-diketonates (thd) precursors have proven to be the most desirable for alkaline earth metal deposition.<sup>16</sup> Beyond batteries and ferro/piezo-electronic devices, the APONs presented here are of interest for applications in next generation neuromorphic computing. Realization of neuromorphic computing requires interfacing with neurons, which may require the use of Na<sup>+</sup> and K<sup>+</sup> conductors. The fabrication of functional sensors that are integrable with biological systems are therefore of high interest.

#### 4.10. Summary and Conclusions

Table 4.2. Summary of ALD Deposition, Chemical Composition, and Ionic Properties of APONs.

	<b>LiPON</b>	<b>NaPON</b>	<b>KPON</b>
ALD Temperature Window (°C)	200-300	300-375	300-375
Growth Per Cycle (Å/cycle)	0.16-0.93	0.13-1.0	0.19-0.93
Stoichiometry	Li <sub>2</sub> PO <sub>2</sub> NC	Na <sub>4</sub> PO <sub>3</sub> NC <sub>2</sub>	K <sub>5</sub> PO <sub>6</sub> N <sub>0.2</sub> C <sub>5</sub>
Ionic Conductivity at 25 °C (S/cm)	$3.7 \times 10^{-7}$	$1.0 \times 10^{-7}$	$7.4 \times 10^{-9}$
Activation Energy (eV)	0.55	0.53	-

In this chapter we have presented a new ALD process of KOPN and compared it to our previous work on ALD LiPON and NaPON. Their ALD process conditions, chemical composition, and ionic properties are summarized in Table 2. The LiPON ALD process was found to exhibit the most desirable properties. Deposition of LiPON with adequate growth rates was demonstrated at relatively low temperatures, in addition to obtaining the lowest carbon contamination (~10%), and the highest overall ionic conductivity ( $3.7 \times 10^{-7}$  S/cm at 25 °C).

NaPON required temperatures ~100 °C higher than that of LiPON for comparable growth rates. The structure of NaPON is in strong agreement with LiPON, confirming its classification as a polyphosphazene, with additional disruption of the P-N=P backbone and carbon incorporation. NaPON's ionic conductivity was on the same order of magnitude of LiPON ( $10^{-7}$  S/cm) and exhibited nearly the same activation energy. This supports the XPS results indicating that the structural configuration of NaPON and LiPON are similar, as the modes of ionic conduction through the polyphosphazene chain are energetically similar despite the increased size of Na<sup>+</sup> compared to Li<sup>+</sup>.

The ALD process parameters for KPON revealed very similar growth kinetics over the temperature range of 300-375 °C to that of NaPON. Despite the similarity in ALD process parameters, the chemistry of the K-based film was quite different. KO<sup>t</sup>Bu-DEPA reacted to produce a film with little N content and its XPS analysis more closely resembled a K<sub>3</sub>PO<sub>4</sub>/K<sub>2</sub>CO<sub>3</sub> film. The difference in reactivity of the film is attributed to increased steric bulk of the KO<sup>t</sup>Bu precursor, and increased degree of basicity compared to Li- and NaO<sup>t</sup>Bu. The similarities in growth rates to the NaPON process are indicative of the thermal decomposition facilitated growth of these processes due to their similarities in sublimation behavior determined by TGA. The ionic properties of KPON are promising, as it exhibited an ionic conductivity of  $7.4 \times 10^{-9}$  S/cm at room

temperature with brief air exposure, which is slightly higher than that of air-exposed NaPON. KPON would be expected to follow a similar trend as that of LiPON/NaPON and exhibit a further increase in ionic conductivity for a pristine film. As mentioned, further electrochemical characterization of KPON is necessary to fully understand its ionic transport behavior and provide a direct comparison to NaPON and LiPON.

# Chapter 5: Nanoscale Sodium Solid-State Batteries Enabled by the Solid Electrolyte NaPON

## 5.1. Introduction

The development of an ALD process for the solid electrolyte NaPON has the potential to enable the first nanoscale Na-SSB, as there are no documented deposition methods for thin-film solid Na electrolytes. NaPON possesses a relatively high ionic conductivity ( $10^{-7}$  S/cm) and a wide voltage stability window up to 6 V vs. Na/Na<sup>+</sup> while remaining ionically conductive and electronically insulating.<sup>56</sup> Further, its stability with Na metal potentially enables high energy density Na metal batteries. In this chapter, the electrochemical stability of NaPON with a V<sub>2</sub>O<sub>5</sub> cathode is measured. V<sub>2</sub>O<sub>5</sub> possesses a unique crystal structure with a large interlayer spacing of 4.4 Å, allowing for intercalation of alkali ions such as Li<sup>+</sup>, Na<sup>+</sup>, and K<sup>+</sup>.<sup>134</sup> V<sub>2</sub>O<sub>5</sub> has proven to be a successful cathode for LIBs due to its high theoretical capacity of 294 mAh/g and excellent stability<sup>135</sup>. The capacity of V<sub>2</sub>O<sub>5</sub> is slightly lower in SIBs but still possesses a relatively similar theoretical capacity of 235 mAh/g. The large size of Na<sup>+</sup> compared to Li<sup>+</sup> also results in a lower diffusivity in the host V<sub>2</sub>O<sub>5</sub>, causing slower sodiation/desodiation kinetics. The electrochemical properties of V<sub>2</sub>O<sub>5</sub> can be improved through nanostructuring or surface modifications.<sup>107</sup> Specifically, nanostructuring provides improved contact between the electrode/electrolyte and shortened diffusion lengths to compensate for the low Na<sup>+</sup> diffusivity, enabling higher charge-discharge rates. The nanoscale V<sub>2</sub>O<sub>5</sub> deposited by ALD in this work provides such improved contact for high performing SIBs.

In this chapter, the electrochemical behavior of nanoscale V<sub>2</sub>O<sub>5</sub> and NaPON are examined. Reversible Na<sup>+</sup> electrochemistry is demonstrated with bare V<sub>2</sub>O<sub>5</sub> and NaPON coated V<sub>2</sub>O<sub>5</sub> electrodes in a liquid-based electrolyte before moving to all solid-state devices. SSBs are

fabricated in a Na/NaPON/V<sub>2</sub>O<sub>5</sub> configuration, using a thermal evaporated Na metal anode. This achievement represents the first realized ALD-based Na-SSB, or thin-film for that matter. The thermal evaporation of Na is non-trivial, with this being the first demonstration of employing a thermally evaporated thin-film Na metal anode. To complement the observed electrochemistry of the Na-SSB, interface characterization is performed using X-ray photoelectron spectroscopy (XPS) and cryo-Transmission Electron Microscopy (TEM) to reveal the formation of interphases at the electrode/electrolyte interface. Cryo-TEM proves to be an essential technique for the understanding of interphases/interfaces at the nanoscale with sensitive materials such as those in Na-SSBs.

## **5.2. Experimental Procedures**

### **Fabrication**

V<sub>2</sub>O<sub>5</sub> was deposited at 170 °C with vanadium oxytriisopropoxide (VTOP) and ozone as precursors in a Beneq TFS 500 ALD reactor. Polished 304 stainless-steel discs were used as substrates for liquid electrochemistry experiments and Pt-coated Si wafers for SSBs. NaPON was deposited directly on V<sub>2</sub>O<sub>5</sub> samples at 375 °C using sodium *tert*-butoxide (NaO<sup>t</sup>Bu) and diethyl phosphoramidate (DEPA) as precursors in a Fiji F200 ALD reactor. The NaO<sup>t</sup>Bu precursor was kept at 155°C, while the DEPA was maintained at 115°C. The thickness of each layer was measured by spectroscopic ellipsometry (SE) to be 40 nm for V<sub>2</sub>O<sub>5</sub> and 100 nm for NaPON using predetermined phenomenological optical models with thicknesses confirmed by *ex-situ* SEM measurements. Na was evaporated in a custom-built thermal evaporator attached to an Ar filled glovebox. Sodium metal cubes were cleaned and loaded into a tantalum crucible and resistively

heated to 300 °C. The samples were exposed to the evaporated Na flux for one hour, resulting in a thickness of  $\sim 2$   $\mu\text{m}$ .

## Electrochemistry

Liquid-based electrochemistry measurements were performed in a CR2032 coin-cell assembly (MTI) with a 1M NaClO<sub>4</sub> propylene carbonate (PC)/ethylene carbonate (EC) (Sigma-Aldrich) and a Na metal anode. Na metal foil is not readily available as it is for Li, so Na metal anodes were cut from Na cubes (Sigma-Aldrich). For all SSB experiments, a Na metal anode was evaporated through a shadow mask onto the NaPON/V<sub>2</sub>O<sub>5</sub>/Pt sample. SSB samples were tested on a custom-built stage with heating control using a micromanipulator probe contacts inside the glovebox. A biologic VSP potentiostat was used for all electrochemical tests in liquid and solid samples. Electrochemical tests include cyclic voltammetry (CV), galvanostatic cycling, and electrochemical impedance spectroscopy (EIS). EIS measurements were collected at a frequency range of 200 kHz – 300mHz with a sinusoidal amplitude of 40 mV.

## Characterization

A J.A. Woollam M-2000D spectroscopic ellipsometer was used for *operando* monitoring of NaPON growth on a V<sub>2</sub>O<sub>5</sub>/Si starting surface. The NaPON film on Si was fit to a Tauc-Lorentz oscillator model that was determined during the NaPON process development.<sup>56</sup> A B-spline model was used to fit the real-time NaPON growth on a V<sub>2</sub>O<sub>5</sub> surface.

After deposition, films were transferred under UHV directly to a Kratos Ultra DLD Surface Analysis system ( $1 \times 10^{-9}$  Torr) for XPS analysis. All XPS data were collected using monochromatic Al K $\alpha$  radiation (12 kV) at a total anode power of 144 W. Survey spectra were collected using a pass energy of 160 eV and a binding energy step size of 1 eV. High- resolution

spectra were collected using a pass energy of 20 eV and a binding energy step size of 0.1 eV. Charge neutralization was employed using an electron flood gun. Samples were observed not to change over time in the vacuum environment. All data were analyzed using CasaXPS with a Shirley background and 50/50 Gaussian/Lorentzian pseudo-Voigt functions. High-resolution peak area ratios were used for elemental quantification, using tabulated Kratos relative sensitivity factors. Ar<sup>+</sup> depth profile was performed with 5 kV Ar<sup>+</sup> ions with a calibrated sputter rate of 5.5 nm/minute on Ta<sub>2</sub>O<sub>5</sub>. Survey and core-level spectra were recorded every 60 s from 0-2400 s of etch time.

Cryo-focused ion beam (FIB) and Cryo-TEM measurements were performed at the Center for Integrated Nanotechnologies (CINT) at Sandia National Laboratory. Samples were loaded into the cryo-FIB directly from a glovebox using an inert transfer shuttle. TEM lamella sample preparation was performed on a Scios 2 Dual Beam scanning electron microscope (SEM)/FIB with a Leica vacuum cryo transfer system (VCT) cryogenic stage installed. To preserve the structural integrity of the beam sensitive materials and reduce artifact inclusion the sample was cooled to -145 °C in ~20 minutes and kept at -140 °C during the Ga<sup>+</sup> FIB process. FIB milling was performed at a reduced accelerating voltage of 16 keV (1.5 nA) for trenching. Final thinning was carried out using a beam current of 50 pA. The E-beam was kept at 5kV (50 pA) and imaged with the secondary electron detector during this process.

The TEM lamella was directly transferred to a scanning TEMs (STEM) for further analysis. Cryo-STEM high-angle annular dark-field (HAADF) imaging and chemical mapping were performed on a probe-corrected FEI Company ChemiSTEM Titan G2 80–200 STEM equipped with a X-field emission gun (X-FEG, an ultra-stable high-brightness Schottky FEG source) operated at 200 kV. Chemical mapping of the cryo-FIB lamella was performed with the equipped

Super-X energy-dispersive x-ray spectroscopy (EDX) detector system (four windowless silicon drift detectors with a combined solid angle of 0.7 sr) and Gatan Quantum 963 electron energy loss spectroscopy (EELS)/imaging filter systems. The lamella was loaded into the microscope in a Gatan 626 Single tilt cryo-TEM holder and HAADF imaging preceded chemical mapping. Analysis of the EELS and EDS chemical component maps was done with multivariate statistical analysis.

### **5.3. Electrochemical Analysis in Liquid Electrolyte**

The electrochemical activity of  $V_2O_5$  and NaPON were characterized in a coin-cell configuration with a conventional liquid electrolyte and a Na metal anode. CV measurements were performed to determine the redox activity associated with  $Na^+$  intercalation in bare  $V_2O_5$  and NaPON-coated  $V_2O_5$ . Figure 5.1 shows the CV curve for  $V_2O_5$  and NaPON/ $V_2O_5$ , both indicating reversible  $Na^+$  electrochemistry. For the bare  $V_2O_5$  electrode, the electrochemical cell first undergoes a reductive potential sweep towards 1.2 V, followed by an oxidative potential sweep to 4 V. A gradual decrease in current is observed at 2.0 V corresponding to the  $Na^+$  intercalation of  $V_2O_5 \rightarrow NaV_2O_5$ , and an anodic peak at 1.3 V representing further sodiation to  $Na_2V_2O_5$ . The following  $Na^+$  insertion reactions are reversed on the subsequent oxidation sweep, where at 1.8 V  $Na_2V_2O_5 \rightarrow NaV_2O_5$  occurs, and at 2.3 V further oxidation to un-sodiated  $V_2O_5$ . For NaPON/ $V_2O_5$ , these ion-insertion reactions are less distinct in the CV due to a higher contribution of pseudocapacitive current than the diffusive dominated current in bare  $V_2O_5$ .<sup>136</sup> The CV for NaPON/ $V_2O_5$  begins with a positive potential sweep, resulting in two distinct peaks at 2.0 V and 2.4 V. The peak at 2.0 V corresponds to  $Na_2V_2O_5 \rightarrow NaV_2O_5$ , and the peak at 2.4 V represents  $NaV_2O_5 \rightarrow V_2O_5$ . It should be noted that there is an obvious difference in the initial open-circuit

voltage (OCV) of the assembled cells, that being bare  $V_2O_5$  at 2.4 V and NaPON/ $V_2O_5$  at 1.1 V. The voltage of the  $V_2O_5$  electrode vs. Na/Na<sup>+</sup> is a strong indication of the sodiation state of  $V_2O_5$ , with 1.1 V representing a sodiation state of  $Na_2V_2O_5$ .<sup>137, 138</sup> This observation is attributed to Na<sup>+</sup> pre-intercalating the  $V_2O_5$  electrode during the NaPON ALD deposition and further confirmed by TEM-based EELS and XPS measurements later in this chapter.

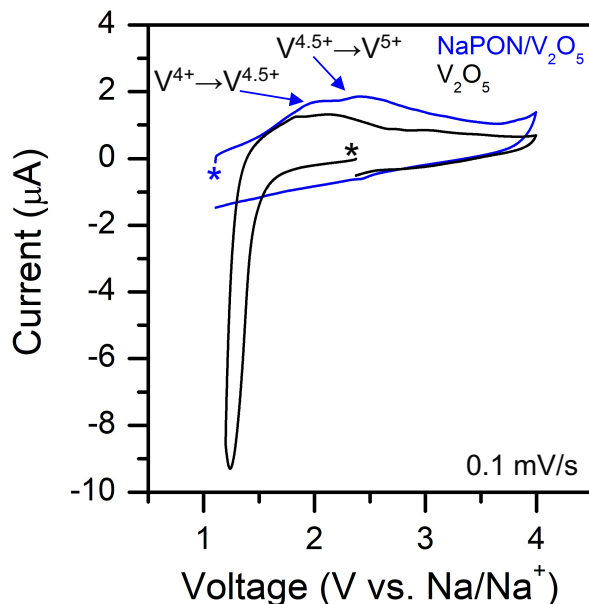


Figure 5.1. Cyclic voltammetry of bare  $V_2O_5$  and NaPON/ $V_2O_5$  in a 1M NaClO<sub>4</sub> PC:EC electrolyte with a Na metal reference/counter electrode. \* refers to the open-circuit voltage (OCV) of the battery as assembled prior to the measurement.

GV cycling and EIS tests were also performed to understand the electrochemical cycling behavior. The results for bare  $V_2O_5$  are shown in Figure 5.2a,b and NaPON/ $V_2O_5$  in Figure 5.2c,d. Both samples display stable charge/discharge behavior for up to 50 cycles. The sodiation of bare  $V_2O_5$  is clearly observed in the discharge curve for cycle 25 and 50. From 2.5-2.1 V there is a peak indicating Na<sup>+</sup> insertion to Na $V_2O_5$ , followed by another broad feature at 2.0-1.6 V representing further sodiation to  $Na_2V_2O_5$ . In the case of NaPON/ $V_2O_5$ , the GV curves lack obvious peaks/plateaus representing Na<sup>+</sup> insertion/de-insertion. This is attributed to an enhanced pseudocapacitive electrochemical response, caused by the polarization of the thick NaPON layer

(~75 nm) with the thinner  $V_2O_5$  (~40 nm). The sodiation of bare  $V_2O_5$  in Figure 5.2a shows an initial discharge capacity of 275 mAh/g in cycle 1 and an increase to 325 mAh/g in cycle 50. The discharge capacity hardly changes for NaPON/ $V_2O_5$  during cycling, as cycle 1 shows a capacity of 225 mAh/g and a small increase to 240 mAh/g in cycle 50. From this observation, it is hypothesized that the increase in discharge capacity with cycling in bare  $V_2O_5$  is due to solid-electrolyte interphase (SEI) reaction, causing a passivating layer on the electrode surface due to liquid electrolyte byproducts. The SEI formation is consistent with the observed high discharge

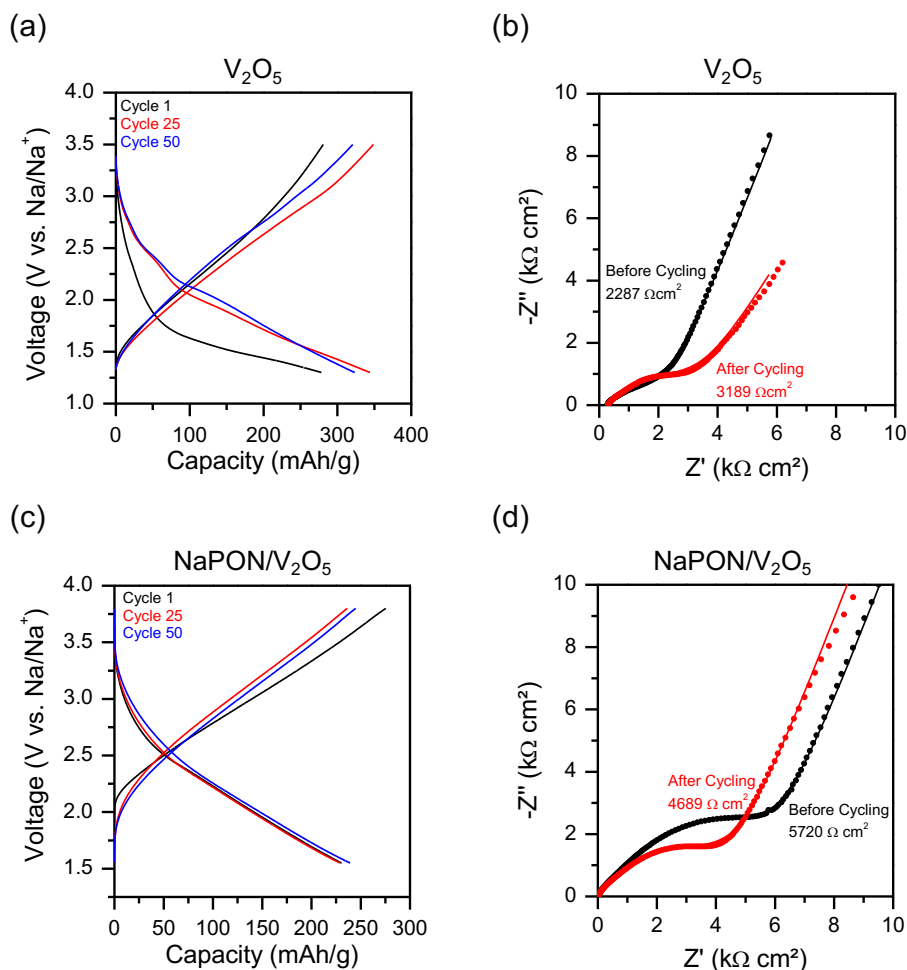


Figure 5.2. Galvanostatic cycling stability of  $V_2O_5$  and NaPON/ $V_2O_5$  in 1M NaClO<sub>4</sub> PC:EC electrolyte. (a) Charge/discharge curves for  $V_2O_5$  at a current density of 0.5  $\mu$ A/cm<sup>2</sup> between 1.3-3.5 V. (b) Nyquist plot for  $V_2O_5$  before and after cycling. (c) Charge/discharge curves for NaPON/ $V_2O_5$  at a current density of 1.0  $\mu$ A/cm<sup>2</sup> between 1.55-3.8 V. (d) Nyquist plot for NaPON/ $V_2O_5$  before and after cycling.

capacity that is over the theoretical capacity of 235 mAh/g. The EIS spectra of bare  $V_2O_5$  in Figure 5.2b supports the formation of an undesired SEI layer, as the total impedance before/after cycling increases. The NaPON/ $V_2O_5$  electrode shows excellent capacity retention with cycling, and the EIS spectra in Figure 5.2d shows a decrease in overall impedance of the electrode after the 50 cycling. This result implies that NaPON forms a stable SEI between  $V_2O_5$  and the liquid electrolyte, facilitating  $Na^+$  and mitigating electrolyte breakdown. It is promising that the reaction occurring during the ALD NaPON deposition on  $V_2O_5$  does not negatively affect the electrochemical activity of  $V_2O_5$ , rather the observed data here suggests it is improved through the  $Na^+$  pre-intercalation compared to bare  $V_2O_5$ .

#### **5.4. Solid-State Electrochemistry**

All solid-state electrochemical characterization of NaPON was performed by fabricating Na/NaPON/Pt devices. A thermal evaporator attached directly to an Argon glovebox was used for depositing thin-film Na metal contacts through a shadow mask on the NaPON. CV and EIS measurements for Na/NaPON/Pt are shown in Figure 5.3. In Figure 5.3a, CV was performed from -0.1 V to 3.0 V in the first cycle and increasing up to 6.0 V in the third cycle. A sharp negative current response is observed at -0.7 V corresponding to Na-Pt alloying, and on the positive sweep a sharp peak at 0.05 V represents the Na-Pt dealloying reaction. These peaks continue to appear in the second and third cycle, with increasing intensity. A broad oxidative peak is observed at 2.42 V in the first cycle, shifting towards 2.8 V in the second cycle, and in the third cycle there is a subtle broadening at 3.0 V. There are additional minor oxidative peaks at 0.05 V in the second and third cycle, and evolution of a new reduction peak at 0.96 V after charging to 6.0 V in the third cycle. This is similar to the CV response of ALD LiPON with Li and Pt evaporated electrodes, which displays reversible Li alloying/dealloying just below 0 V and minor oxidative peaks at high

voltage.<sup>35</sup> The oxidative peaks are likely due to interfacial reaction of Na metal with NaPON, but does not result in electrolyte breakdown as the NaPON film remains the ability to pass ionic current while remaining electronically insulating. This is evidenced in Figure 5.3b, in which EIS spectra before and after cycling display a reduced impedance following the CV sweeps. The reduced impedance implies the formation of a stable SEI, facilitating Na<sup>+</sup> diffusion and enabling operation of the SSE in a voltage window beyond its theoretical thermodynamic potential window.

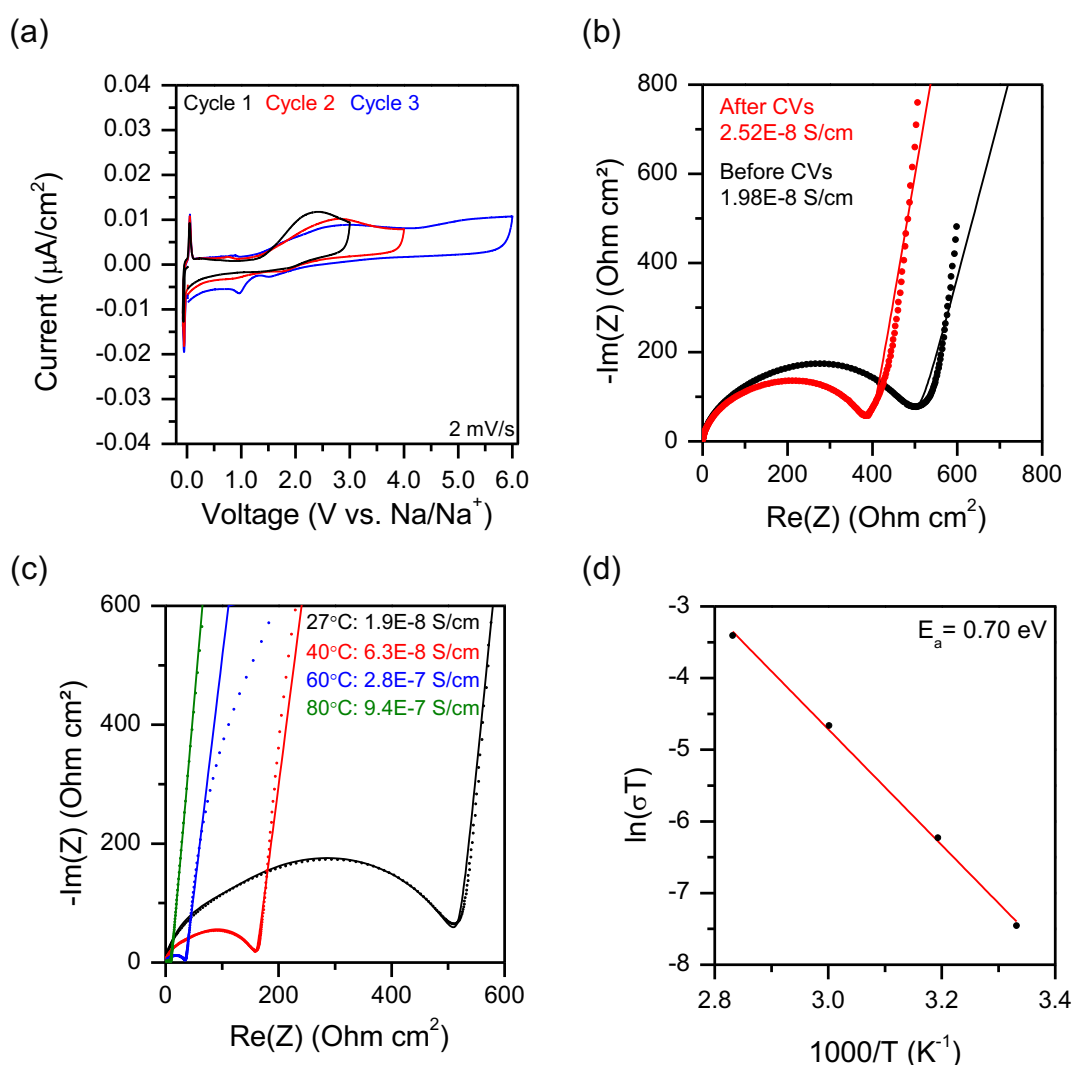


Figure 5.3. Solid-state electrochemical stability of NaPON. (a) CV of Na/NaPON/Pt stack from -0.8-6 V at 2 mV/s. (b) EIS spectra of Na/NaPON/Pt before and after CV measurements. (c) EIS spectra of Na/NaPON/Pt between 27 and 80 °C. (d) Arrhenius plot for Na/NaPON/Pt showing activation energy for Na<sup>+</sup> conduction.

EIS measurements were also carried out from room temperature up to 80 °C (Figure 5.3c). The initial room temperature ionic conductivity was  $1.9 \times 10^{-8}$  S/cm, and increased up to  $9.4 \times 10^{-7}$  S/cm at 80 °C. From these temperature-based measurements, the activation energy for ion conduction could be determined from the Arrhenius relationship  $\sigma T = A \exp\left(\frac{-E_A}{kT}\right)$ , plotted in Figure 5.3d. The observed ionic conductivities are approximately one order of magnitude higher than we previously reported for NaPON in the case of using a Au blocking electrode ( $1.0 \times 10^{-7}$  S/cm at 25 °C) instead of Na.<sup>56</sup> The activation energy is determined to be 0.70 eV for Na/NaPON/Pt, which is slightly higher than 0.53 eV which was measured for Au/NaPON/Pt. The excess energetic cost to ion conduction through NaPON is attributed to the interface of NaPON/Na. Despite the higher ionic conductivity, the CVs and EIS support the stability of NaPON with Na metal and the formation of a stable SEI, providing effective ion conduction.

SSBs were fabricated using a V<sub>2</sub>O<sub>5</sub> electrode (40 nm), NaPON SSE (100 nm), and a Na metal anode (1000 nm). A schematic for the fabrication process flow along with an optical image of the as-prepared SSBs is displayed in Figure 5.4. The entire fabrication process and electrochemical testing was performed in an inert environment with samples passed among UHV coupled ALD reactors, metal evaporation chambers, and an Ar-filled glovebox.

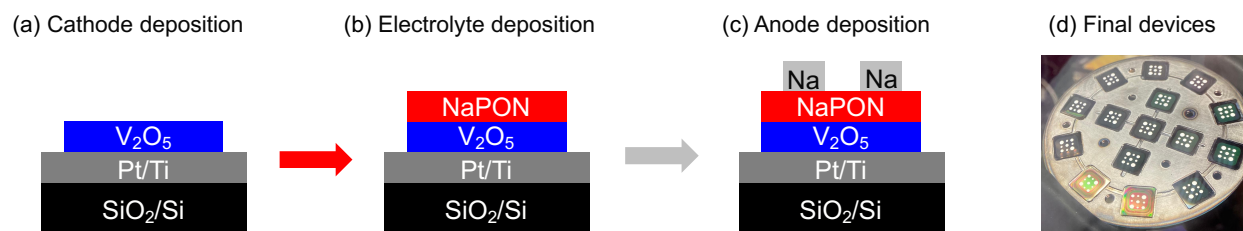


Figure 5.4. Fabrication process for Na-SSBs. (a) ALD deposition of V<sub>2</sub>O<sub>5</sub> cathode, (b) ALD deposition of NaPON SSE, (c) thermal evaporation of Na metal anode, (d) optical images of final devices on 1x1 cm<sup>2</sup> Pt coated Si chips.

CV measurements were performed to understand the electrochemical behavior of NaPON/V<sub>2</sub>O<sub>5</sub> / Na in this all-solid-state configuration. Figure 5.5a shows the CV curve for the Na-SSB. The battery is charged up to 4.0 V from its initial OCV of 0.05 V at 1 mV/s, and repeated for a second cycle stopping at a discharge voltage of 1.0 V. In cycle 1, oxidative peaks are observed at 0.18 V, 1.8 V, 2.6 V, and 3.7 V. The peak at 0.18 V likely represents Na<sup>+</sup> extraction due to the highly sodiated starting state based on the low electrochemical potential. The peak at 1.8 V is assigned to the oxidation reaction of Na<sub>3</sub>V<sub>2</sub>O<sub>5</sub> → Na<sub>2</sub>V<sub>2</sub>O<sub>5</sub>, 2.6 V to Na<sub>2</sub>V<sub>2</sub>O<sub>5</sub> → NaV<sub>2</sub>O<sub>5</sub>, and 3.7 V to NaV<sub>2</sub>O<sub>5</sub> → V<sub>2</sub>O<sub>5</sub>. In the reductive sweep of the CV, broad features are observed representing the reduction of V<sub>2</sub>O<sub>5</sub> and associated insertion of Na<sup>+</sup> into the host structure. In the second cycle, the lowest voltage peak in cycle one is not observed, and the three oxidation peaks of vanadium are shifted down by ~ 1 V due to the higher scan rate of 2 mV/s. The disappearance of the first peak and lack of clear electrochemical responses in the cathodic region of the CV suggests irreversible Na<sup>+</sup> transport, further supported by the EIS spectra in Figure 5.5b. The resistivity

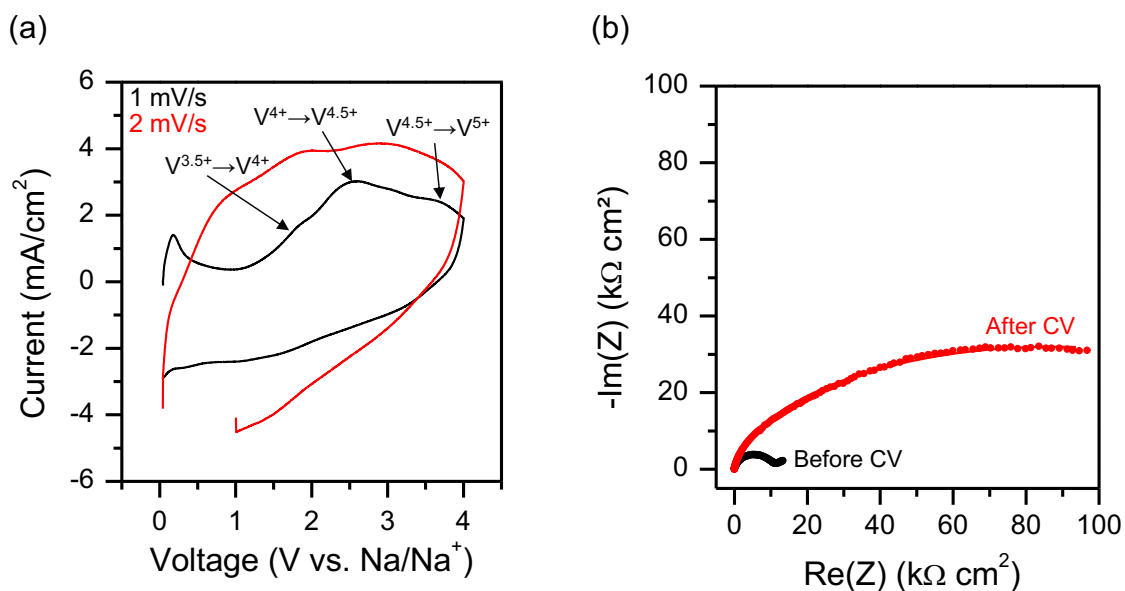


Figure 5.5 (a) CV of solid-state Na/NaPON/V<sub>2</sub>O<sub>5</sub> between 0.05 V and 4.0 V. The scan rate is 1 mV/s for cycle 1 and 2 mV/s for cycle 2. (b) EIS spectra of solid-state Na/NaPON/V<sub>2</sub>O<sub>5</sub> before and after CV measurements.

increases more than an order of magnitude after the CV measurements, indicating the formation of an interphase within the SSB, which supports the irreversible electrochemistry observed in the CV.

Galvanostatic cycling was performed on the Na/NaPON/V<sub>2</sub>O<sub>5</sub> SSB to evaluate its cycling stability. Figure 5.6a shows the initial charge/discharge cycles for the SSB. The initial OCV for this SSB was 0.008 V, indicating an excess of 3 Na<sup>+</sup> in stoichiometric V<sub>2</sub>O<sub>5</sub>. In the first cycle, the cell is charged up to 4.0 V achieving a capacity of 1.6 μAh/cm<sup>2</sup>. On the subsequent discharge to 1.2 V, a discharge capacity of only 0.8 μAh/cm<sup>2</sup> is obtained, indicating the V<sub>2</sub>O<sub>5</sub> is unable to store as much Na as was initially present in the electrode. For the following cycles, the discharge capacity is able to match the charge capacity. This is shown in Figure 5.6b, where nearly 100% coulombic efficiency is achieved for 100 cycles. Despite this high coulombic efficiency, the discharge capacity decays rapidly, dropping from 0.8 μAh/cm<sup>2</sup> to 0.4 μAh/cm<sup>2</sup> in the first 5 cycles, and approaching 0.2 μAh/cm<sup>2</sup> after 100 cycles. The rate performance of the Na-SSB is displayed in Figure 5.6c. The discharge capacity approaches 0 μAh/cm<sup>2</sup> at an applied power density of 25 μA/cm<sup>2</sup>, but recovers its initial discharge capacity of 0.8 μAh/cm<sup>2</sup> when returning to the original

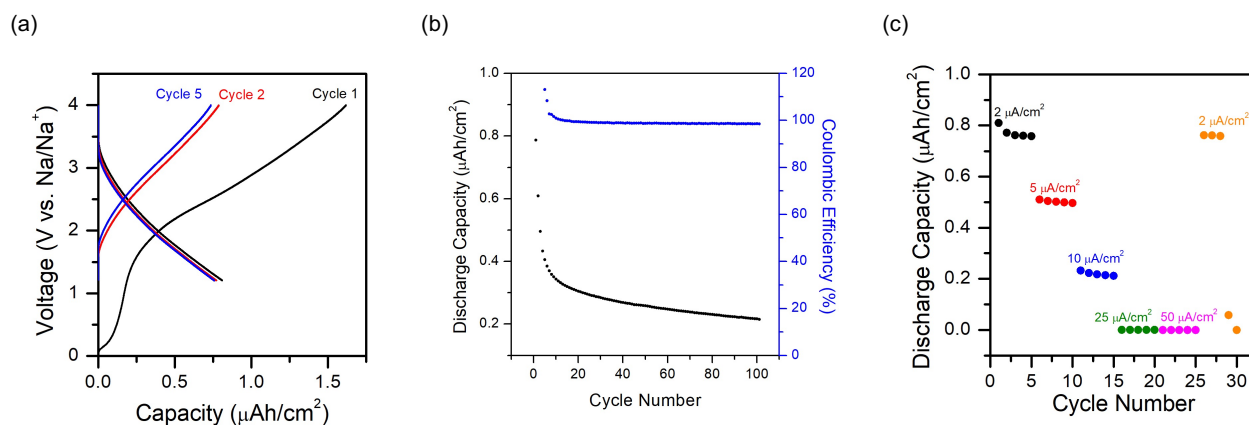


Figure 5.6. Galvanostatic Cycling of Na/NaPON/V<sub>2</sub>O<sub>5</sub> SSBs. (a) Charge/discharge curves between 1.2 – 4.0 V at 2 μA/cm<sup>2</sup>. (b) Discharge capacity and coulombic efficiency for 100 cycles between 1.2 – 4.0 V at 5 μA/cm<sup>2</sup>. (c) Rate performance of Na/NaPON/V<sub>2</sub>O<sub>5</sub> SSB. Charge/discharge was performed for 5 cycles at each rate. Cell failure occurred after returning to initial rate at the end of the test.

rate of  $2 \mu\text{A}/\text{cm}^2$ . However, despite this capacity retention after reaching high rates, the cell fails on the 5<sup>th</sup> cycle upon return to  $2 \mu\text{A}/\text{cm}^2$ . The cycling results of the Na-SSB imply severe resistance to  $\text{Na}^+$  mobility and irreversibility leading to low capacity and rapid decay.

The Na-SSB displays both inferior rate and capacity metrics in comparison to the analogues nanoscale Li-SSB (Li/LiPON/ $\text{V}_2\text{O}_5$ ) reported by Pearse et al.<sup>10</sup> In that case, the Li-SSB maintained a capacity of  $3 \mu\text{Ah}/\text{cm}^2$  at a rate of  $10 \mu\text{A}/\text{cm}^2$ , which is 6 times greater than the capacity at the equivalent rate in the Na-SSB. Despite the inferior performance, it is worth emphasizing that this thesis represents a novel demonstration of the first thin-film Na-SSB, and as such processing conditions and device integration have not been adequately optimized. The NaPON SSE proves to be stable with Na metal in absence of a  $\text{V}_2\text{O}_5$  electrode, remaining ionically conductive without showing additional impedance to  $\text{Na}^+$  conduction after cycling the Na/NaPON/Pt stack. However, there are clearly significant complications with the inclusion of a  $\text{V}_2\text{O}_5$  electrode. In the following section, we present structural characterization to discern the observed electrochemical phenomena resulting from electrochemical degradation of the NaPON/ $\text{V}_2\text{O}_5$  interface.

## **5.5. Interfacial Characterization**

### **NaPON-V2O5**

The observed electrochemical phenomena suggests that there is dynamic reactivity occurring during the fabrication of the Na/NaPON/ $\text{V}_2\text{O}_5$  SSB. To understand this phenomena, we employed *in-operando* SE, XPS, and cryo-TEM to investigate the underlying reactivity in a stepwise manner. Cryo-FIB-TEM is used because the NaPON and Na films are extremely sensitive to ion-beam and electron-beam induced damage at room temperature, necessitating cryo

conditions to maintain their integrity. First, we consider just the consequence of depositing NaPON on a  $V_2O_5$  surface, and then move towards the characterization of a full Na/NaPON/ $V_2O_5$  SSB.

*In-operando* SE was used to provide evidence for the reaction occurring between NaPON and  $V_2O_5$  during the ALD deposition. The *in-operando* experimental condition is particularly useful due to its ability to discern alternations in the surface of the NaPON film in real-time during its growth on the  $V_2O_5$  surface. Figure 5.7 shows the raw data captured by the SE and the modeled thickness profiles for NaPON deposition on a Si substrate (Figure 5.7a-b) and  $V_2O_5$  substrate (Figure 5.7c-d). The raw SE data measures the change of polarization as light interacts with the sample surface, which is correlated to the film thickness through an optical model. The polarization is represented by the amplitude ratio,  $\Psi$ , and is measured dynamically throughout the process at various wavelengths (220 nm – 1000 nm). Figure 5.7a shows minimal change in the  $\Psi$  component during the deposition, consistent with the optical properties of NaPON remaining the same throughout its deposition on Si. This implies that the NaPON film is not undergoing any changes during the deposition. Figure 5.7c shows dramatic change in the  $\Psi$  component for deposition on a  $V_2O_5$  surface. The data indicates that the optical properties of the NaPON layer are changing during deposition, in addition to the underlying  $V_2O_5$  layer being modified during the first 200-300 minutes. To account for this dynamic change, it is assumed the  $V_2O_5$  thickness is not changing as it is being modified. For the NaPON model we use a B-spline model to accommodate the dynamic change while minimizing model fitting error. The continuous spectral data and thickness profile both show dramatic changes in their slopes at 250-350 minutes, then a return to a linear trend for the rest of the deposition. The data implies a significant change taking place beyond the simple linear growth of a NaPON ALD film. At the end of the 1000 cycle deposition of NaPON on  $V_2O_5$ , the final thicknesses are measured to be 74 nm of NaPON and 39 nm of  $V_2O_5$ .

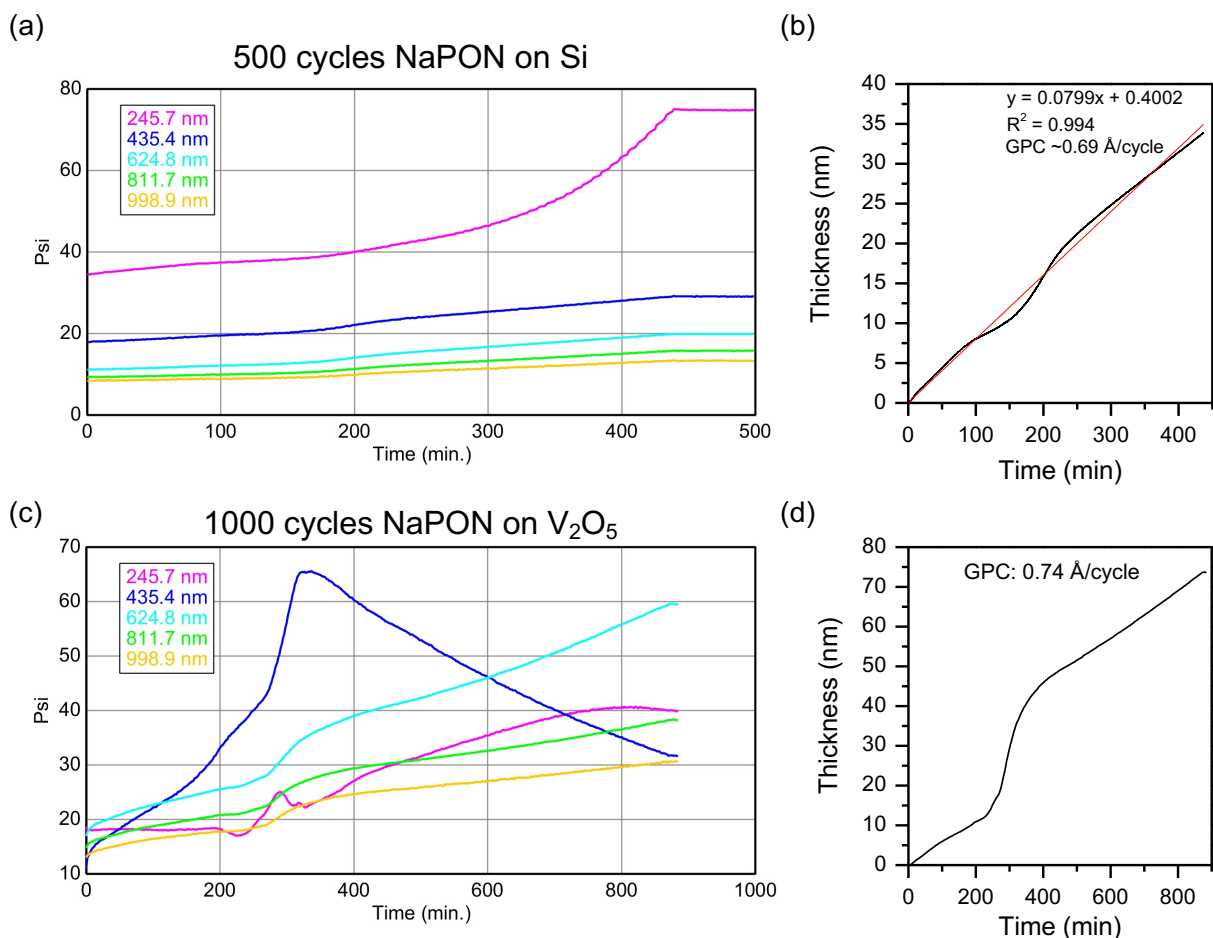


Figure 5.7. In-operando SE characterization of NaPON growth at 375 °C. (a) Raw dynamic data and (b) film thickness profile for NaPON deposition on Si. (c) Raw dynamic data and (d) thickness profile for NaPON deposition on V<sub>2</sub>O<sub>5</sub>/Si.

Further characterization into the reactivity of ALD NaPON on V<sub>2</sub>O<sub>5</sub> was performed by XPS. The same sample was transferred under UHV directly the XPS chamber, where the Ar<sup>+</sup> gun was used to sputter through the stack to measure the composition as a function of thickness. The results of the depth profile are plotted in Figure 5.8a, showing that Na is present throughout the entire materials stack and V is detected in the top NaPON layer. The depth profile reveals three distinct regions: Region I represents the NaPON layer, ranging from 0-400 s in etch time until the boundary where the V signal crosses the P signal. Here, the intersection of increasing/decreasing

atomic concentrations is indicative of the beginning/end of atomic species in the film and thus evidence of a materials boundary. Region II represents a NaPON-V<sub>2</sub>O<sub>5</sub> intermixing layer, ranging from 400-840 s until the Na signal crosses the V signal. Region III represents the bottom VO<sub>x</sub> layer, extending from 840-1150s where the V signal crosses the Si signal. Region III is referred to as VO<sub>x</sub>, representing a mix of vanadium oxides (V<sup>3+</sup>, V<sup>4+</sup>, V<sup>5+</sup>) because of deviations in oxidation state from the starting material V<sub>2</sub>O<sub>5</sub>, implying the presence of mixed VO<sub>x</sub>'s. The surface of region I possesses a chemical composition of Na<sub>3.6</sub>PO<sub>3.0</sub>N<sub>0.7</sub>C<sub>1.6</sub>, in strong agreement with the nominal composition for ALD NaPON.<sup>56</sup> Upon etching, N and C etch at a faster rate than P and Na, with the N concentration reaching 0% at 200 s and C at 300 s. At this same time, the V concentration begins to increase, reaching a maximum within the NaPON region of ~6% V at 240s. The overall stoichiometry at this point is Na<sub>7.4</sub>PO<sub>6.0</sub>N<sub>0.1</sub>C<sub>0.3</sub>V, indicating there is diffusion of V well into the NaPON layer. In region II, phosphorus is etched away and only Na, V, and O remain. The Na signal decreases across the region, while V and O follow the same increasing trend. The overall composition about half-way through the intermixing layer (630s) is Na<sub>1.2</sub>VO<sub>2</sub>. In Region III, Na linearly decreases, while V and O reach a maximum concentration at 1020s, then decrease in concentration through the rest of the region. At 1020s the composition of the VO<sub>x</sub> layer is Na<sub>0.6</sub>VO<sub>1.8</sub>. The thicknesses of each of the layers are determined from the measured thickness by SE prior to XPS depth profile analysis, in congruence with the etch rates. A control NaPON/Si sample found an etch rate of 7.2 nm/minute for NaPON. The etch rate for the full stack is applied to determine the thickness of the mixing and VO<sub>x</sub> regions. Based off these rates, the VO<sub>x</sub> region is 33.4 nm, the mixing region is 40.7 nm, and NaPON is 47.8 nm. This total thickness of 121.9 nm is within 8% difference of the originally measured thickness by the SE of 113 nm. The XPS depth

profile analysis confirms the reactivity observed by *in-operando* SE and reveals that there is reduction of  $V_2O_5$  to  $VO_2$ , and  $Na^+$  intercalation into the oxide host structure.

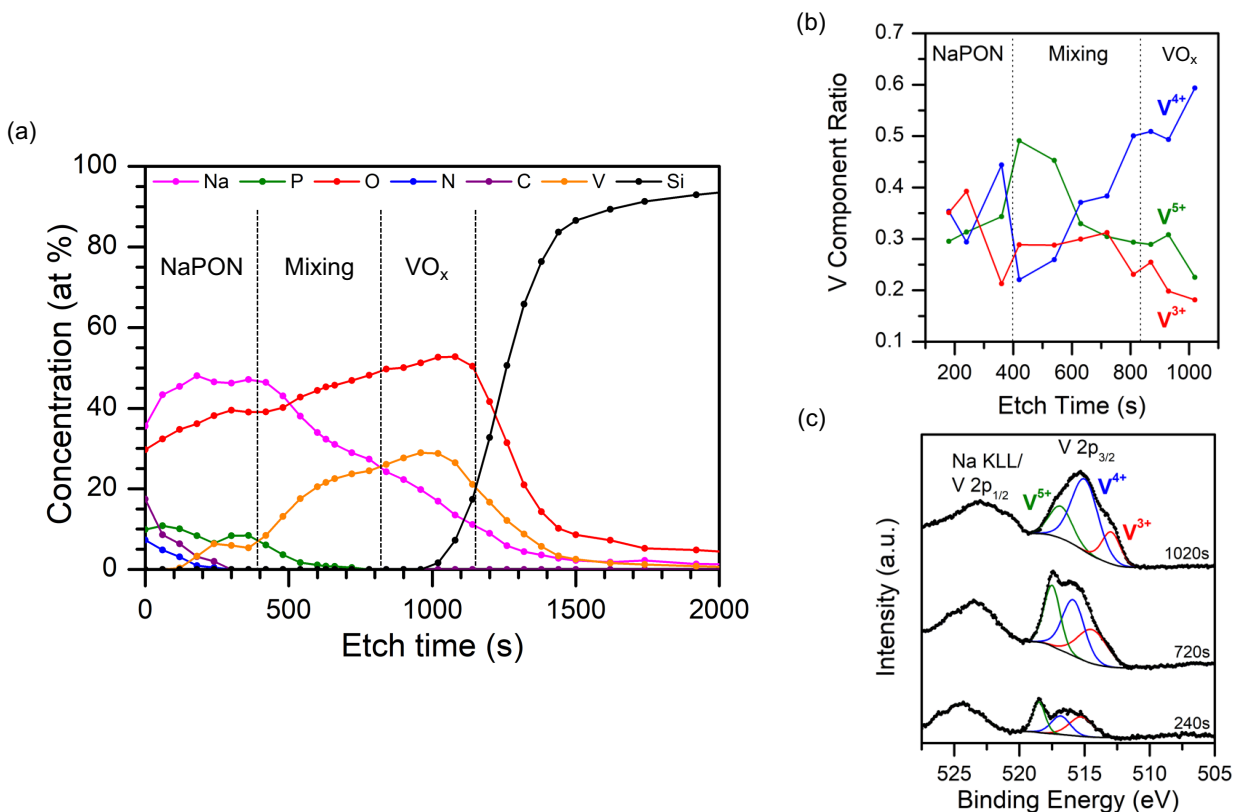


Figure 5.8. XPS depth profile analysis of 1000 cycles of NaPON deposited at 375 °C on  $V_2O_5$ . (a) Depth concentration profile of atomic species. (b) Vanadium oxidation state concentration as a function of etch time. (c) Core-level XPS spectra for the V 2p region measured in the NaPON (240s), mixing (720s), and  $VO_x$  (1020s) regions.

In Figure 5.8b the ratio of vanadium species per total vanadium is plotted as a function of etch time. The general trend follows that the relative amount of  $V^{4+}$  increases as the sample is etched and  $V^{5+}$  and  $V^{3+}$  decrease. At the top half of the mixing region, the vanadium that is present is primarily  $V^{5+}$ , and it becomes more oxidized with  $V^{4+}$  being the dominant species for the lower half of the mixing region and  $VO_x$ . The V 2p core-level XPS spectra is plotted in Figure 5.8c, displaying spectra recorded at the center of each of the three regions. The Na KLL peak overlaps with the V 2p<sub>1/2</sub> peak, so only the V 2p<sub>3/2</sub> peak is fitted for clarity. Not only does the  $V^{5+}$  peak go from the highest intensity component to the lowest with etching, but each of the peaks shift to

lower binding energy with further etching. The  $V^{5+}$  peak is at 518.5 eV at 240 s etching and decreased to 516.8 eV at 1020 etching. A similar trend in decreasing binding energy with etch time is also observed for core-level spectra of other atomic components. This is likely due to the effect of the  $Ar^+$  sputtering on the surface charge of the sample. Overall, this result is telling in that it

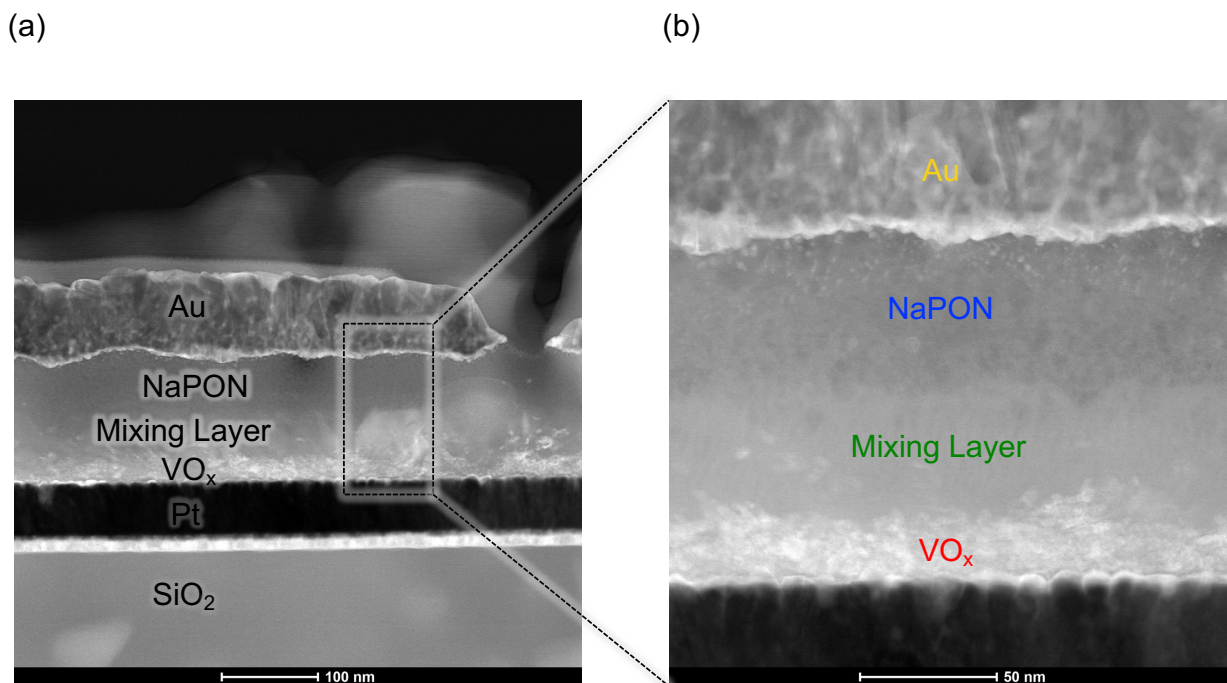


Figure 5.9. Cryo-STEM imaging of NaPON/ VO<sub>x</sub>/Pt stack. (a) Full view of the stack and (b) zoomed in on the stack showing clear distinction of the NaPON, mixing, and VO<sub>x</sub> layers. Imaging was performed with the mid-angle dark field (DF4) detector.

reveals that the oxidation state of the presumed V<sub>2</sub>O<sub>5</sub> ( $V^{5+}$ ) starting material has changed significantly. XPS analysis on a pristine V<sub>2</sub>O<sub>5</sub> sample determined it to be 90%  $V^{5+}$ /10%  $V^{4+}$ .

Visualization of the mixing region described by XPS analysis is realized through cryo-TEM in collaboration with the CINT facility at Sandia National Laboratories. The NaPON film is unable to be imaged by TEM at room temperature due to beam damage, in addition to incurring damage during the FIB process. Cryo-FIB-TEM alleviates such destruction through use of ultra-cool temperatures (-140 °C). The NaPON/V<sub>2</sub>O<sub>5</sub> sample was capped with evaporated Au in our UHV integrated system prior to removal for TEM to preserve the NaPON structure from air

exposure and FIB damage. The Cryo-STEM cross-section of the stack is shown in Figure 5.9, with Figure 5.9a showing the full-view of the FIB cut out and Figure 5.9b focused in on the Au/NaPON/V<sub>2</sub>O<sub>5</sub>/Pt layers. Figure 5.9a displays unavoidable ice contamination above the thin FIB cap and artifacts of the FIB milling. More importantly, it is clearly seen that there is a mixing layer of intermediate contrast between the NaPON and VO<sub>x</sub> layer and is evident in Figure 5.9b. The thickness of each layer is determined from the scale in Figure 5.9b, in which NaPON is 50.1 nm, mixing layer is 48.2 nm, and the VO<sub>x</sub> layer is 21.2 nm. This is in excellent agreement with the thicknesses of each of the layers determined by SE and XPS as shown in Figures 5.7 and 5.8, respectively.

EELS analysis was also performed in the cryo-TEM to provide precise chemical analysis of the observed layers. The EELS coreloss mapping of the C, N, V, and O edge is displayed in Figures 5.10a-d, where the background was removed, and the individual signals were integrated. In Figure 5.10e, multivariate curve mapping is shown to distinguish the NaPON, mixing, and VO<sub>x</sub> layers from each other using the EELS core loss edge integrations. The EELS spectra for each region are displayed in Figure 5.10f-h. The carbon K edge peak at 285 eV and nitrogen K edge peak at 399 eV confirm that carbon and nitrogen are present in NaPON, and not in any of the other layers, also confirmed by XPS measurements. There is a strong V L<sub>3</sub> and V L<sub>2</sub> edge peak in the VO<sub>x</sub> and mixing region, and a low intensity peak in the NaPON region. The transition loss energy can be used to infer the oxidation state of vanadium, as it can exhibit several stable oxidation states ranging from +2 to +5. For the VO<sub>x</sub> region, the height ratio of the V L<sub>3</sub>/L<sub>2</sub> edge and energy position are closest aligned with V<sub>2</sub>O<sub>3</sub> in the literature.<sup>139</sup> However, the oxygen K edge for the VO<sub>x</sub> region is in closer agreement with that of a VO<sub>2</sub> state. This suggests that in the VO<sub>x</sub> region both V<sup>3+</sup> and V<sup>4+</sup> are present. The V edge is at higher energy for the mixed region, implying that the V in the

mixed region is in a higher oxidation state. The EELS and STEM cross-section analysis confirms the Na mobility throughout the layers, in addition to vanadium diffusion beyond the bottom VO<sub>x</sub> electrode.

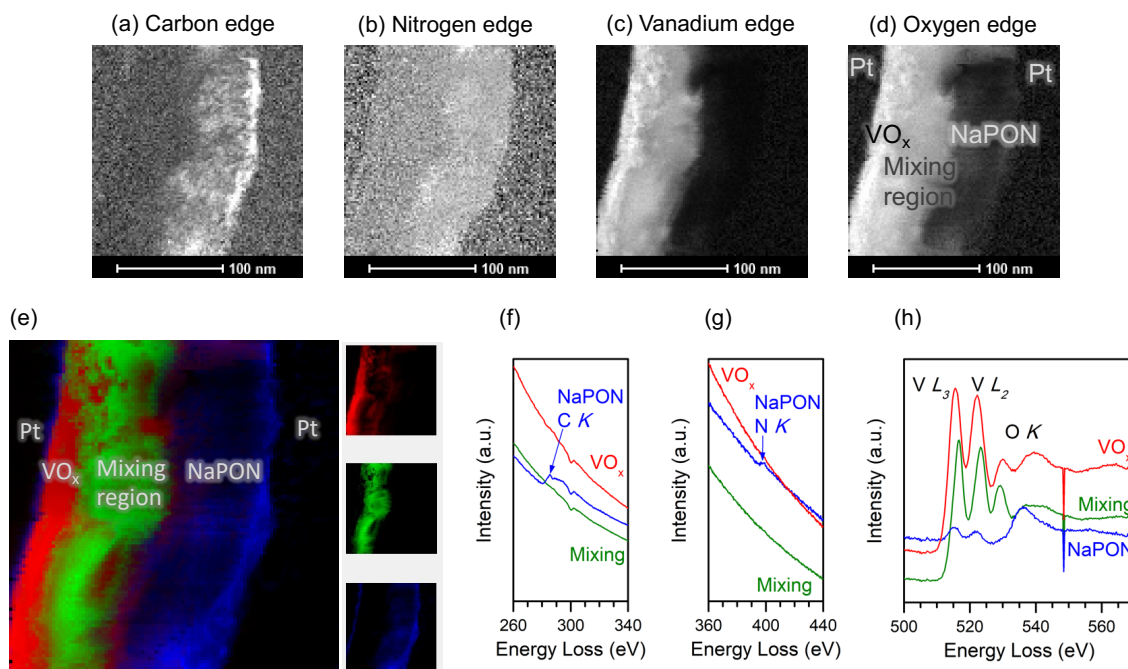


Figure 5.6. EELS coreloss analysis of NaPON/ VO<sub>x</sub>/Pt stack. (a-d) EELS mapping edge integration for carbon, nitrogen, vanadium, and oxygen. (e) multivariate mapping of the VO<sub>x</sub>, mixing, and NaPON regions. (f) C edge EELS spectra, (g) N edge EELS spectra, and (h) V and O edge EELS spectra. The EELS spectra are separated into individual curves for each of the VO<sub>x</sub>, mixing, and NaPON regions. The sharp dip in intensity at 550 eV is due to a dead pixel on the EELS detector.

The intermixing of NaPON and V<sub>2</sub>O<sub>5</sub> is confirmed through the characterization techniques described above. *In-operando* SE presented evidence that there was dynamic change occurring during the NaPON ALD process. XPS depth profiling through the layers suggested the formation of a mixing region between NaPON and V<sub>2</sub>O<sub>5</sub>, and this region was confirmed through cryo-TEM analysis. The cryo-TEM analysis proves to be an excellent companion to the XPS analysis, providing information on oxidation state as well as thickness. The measured thickness of the VO<sub>x</sub>, mixing, and NaPON layers are in excellent agreement with those calculated from XPS depth

profiling and SE analysis. The XPS depth profile results show fast etching of carbon and nitrogen half-way through the top NaPON layer. However, the EELS core loss mapping shows that nitrogen and carbon are present throughout the NaPON layer. This result indicates the preferential etching of nitrogen and carbon to be a result of the  $\text{Ar}^+$  sputtering process, rather than physical implications of nitrogen and carbon only present in the top of NaPON. There is also slight deviation in the oxidation state of vanadium between the two techniques. XPS finds that the predominant V species is  $\text{V}^{5+}$  for the top half and  $\text{V}^{4+}$  for the bottom half of the mixing layer, and even more predominantly  $\text{V}^{4+}$  in the  $\text{VO}_x$  layer. However, EELS shows that V is more reduced in the  $\text{VO}_x$  layer and more oxidized in the mixed region. Discrepancies between the two techniques are attributed to surface damage by the  $\text{Ar}^+$  sputtering process for XPS depth profile, giving rise to multiple oxidation states of V.

### **Na-NaPON-V2O5**

The electrochemical results of the Na/NaPON/ $\text{V}_2\text{O}_5$  SSB showed that when Na is evaporated on NaPON the SSE is stable within a wide voltage window (0-6 V) and retains its overall cell impedance as compared to the Au/NaPON/ $\text{V}_2\text{O}_5$  half cell. However, when assembled in a full SSB with a Na anode and a  $\text{V}_2\text{O}_5$  cathode, there is rapid capacity decay and buildup of an enormous impedance within the cell after only a few charge-discharge cycles. The cryo-TEM analysis for the NaPON/ $\text{V}_2\text{O}_5$  proved to be extremely effective at characterizing the contents of the interface between the layers without erroneous decomposition of the materials. Therefore, we perform similar cryo-TEM analysis for a Na/NaPON/ $\text{V}_2\text{O}_5$  SSB.

Cross-sectional Cryo-TEM analysis is shown in Figure 5.11. The HAADF-STEM image in Figure 5.11a shows a porous and heterogeneous Na layer that is  $\sim 1100$  nm thick. 3 Pt depositions were put down on the sample prior to FIB. Figure 5.11b-g show the EDS mapping for the HAADF

STEM image. The EDS results show that Na is present everywhere, extending all the way above the bottom Pt layer. The V map shows that V has been removed from the bottom electrode layer and is present throughout the stack even at the top of the Na/Pt interface. This finding explains the poor electrochemistry behavior observed in the Na-SSB. This is likely a consequence of the thermal evaporation of the Na metal anode. The hot molten Na appears to be diffusing through the NaPON film during deposition, and reacting with the bottom  $\text{VO}_x$  layer, quite possibly oversodating it and releasing V throughout the stack and forming multiple phases of  $\text{VO}_x$ .

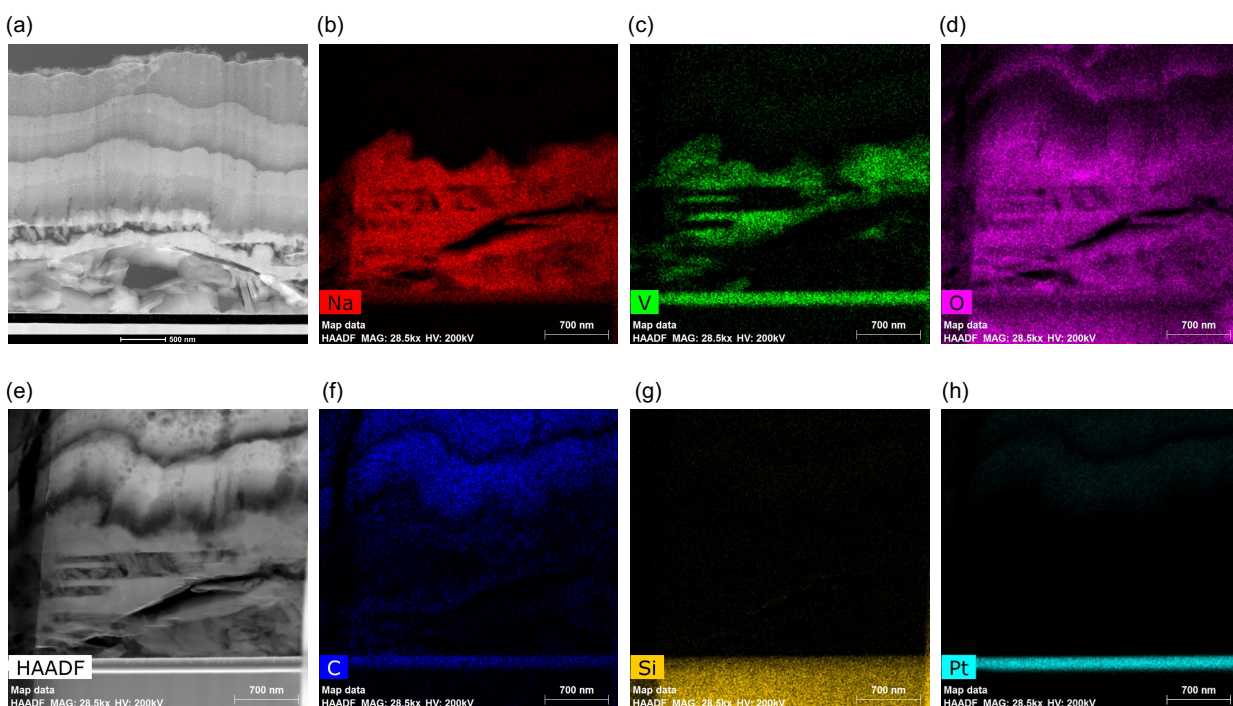


Figure 5.11. Cryo-STEM imaging of Na/NaPON/  $\text{VO}_x$ /Pt stack. (a) HAADF-STEM image of stack. (b-h) EDS images of atomic species.

## 5.6. Discussion

The ALD NaPON deposition on  $V_2O_5$  forms a significant interphase between the two materials, however this interphase does not inhibit its electrochemical performance. Testing in liquid-based systems shows an enhanced cycling stability and reduced impedance with cycling in comparison with bare  $V_2O_5$ . This is believed to be due to the effect of NaPON forming a stable SEI layer at the solid electrode/liquid electrolyte interface. The NaPON/ $V_2O_5$  electrode was presumed to be composed of 75 nm of NaPON and 40 nm of  $V_2O_5$ , however interfacial characterization (Figures 5.8-10) revealed three distinct regions consisting of: 50 nm NaPON/50 nm mixing region/20 nm  $VO_x$  (approximate thicknesses from TEM). The OCV of 1.1 V in the assembled NaPON/ $V_2O_5$  electrode in liquid electrolyte suggests a sodiation state of  $x=2$  for a  $Na_xV_2O_5$  host structure.<sup>137, 138</sup> XPS and EELS analysis confirmed the suspected pre-intercalation reactivity and surprisingly revealed that all the vanadium is primarily in the  $VO_2$  state. The composition was determined to be  $Na_{1.2}VO_2$  for the mixing region and  $Na_{0.6}VO_{1.9}$  for the  $VO_x$  layer. The average composition for these two layers would be  $Na_{0.9}VO_2$ . This sodiation state of  $x=1$   $Na_xVO_2$  at 1.1 V is in excellent agreement with previous voltage correlated sodiation states for  $VO_2$  cathodes. Hamani et al.<sup>140</sup> investigated the sodiation of both the O3 and P2  $Na_xVO_2$  phases, and found that  $x=1$  at 1.2 V for  $Na_xVO_2$  (O3) and  $x=0.92$  at 1.2 V for  $Na_xVO_2$  (P2). The coupled electrochemical-metrology data strongly supports that the starting  $V_2O_5$  is primarily in the  $VO_2$  state, which still exhibits reversible and stable electrochemistry.

$NaVO_2$  is another promising  $VO_x$ -based cathode material for  $V_2O_5$ . In comparison to the theoretical capacity of 235 mAh/g for  $V_2O_5$ ,  $VO_2$  possess a higher theoretical capacity of 323 mAh/g.  $VO_2$  shares a similar layered structure to  $V_2O_5$ , composed of  $VO_6$  octahedron layers, but there are no vacancies in the  $VO_2$  framework.<sup>107</sup>  $VO_2$  is shown to exceed  $V_2O_5$  in performance as

a cathode material in terms of capacity, cycling stability, and voltage stability.<sup>141</sup> A key difference in the electrochemical behavior of VO<sub>2</sub> and V<sub>2</sub>O<sub>5</sub> is that the charge storage mechanism of VO<sub>2</sub> is majority capacitance dominated compared to ion-insertion type in V<sub>2</sub>O<sub>5</sub>.<sup>142, 143</sup> This explains the lack of clear plateaus in the charge/discharge profiles for NaPON/V<sub>2</sub>O<sub>5</sub> in Figure 5.2.

The dynamic change observed in the *in-operando* SE of NaPON deposition on V<sub>2</sub>O<sub>5</sub> is further understood through the XPS and TEM analysis, clearly demonstrating that the reduction of V<sub>2</sub>O<sub>5</sub> to VO<sub>2</sub> (V<sup>5+</sup> → V<sup>4+</sup>) has occurred through the *ex-situ* characterization, in addition to the evidence of Na<sup>+</sup> intercalation into the host VO<sub>x</sub> structure. This is attributed not only to the relatively high deposition temperature of 375 °C for the NaPON process, but also the use of the NaO<sup>t</sup>Bu precursor for NaPON growth provides a reducing environment on the sample surface during NaPON growth. Thermal reduction of V<sub>2</sub>O<sub>5</sub> to VO<sub>2</sub> and V<sub>2</sub>O<sub>3</sub> has been reported by *in-situ* heating under vacuum, in which TEM and EELS revealed reduction from V<sub>2</sub>O<sub>5</sub> to VO<sub>2</sub> occurs at 400 °C and further reduction to V<sub>2</sub>O<sub>3</sub> at 600 °C.<sup>144</sup> The high deposition temperature is enough to support this thermal reduction to VO<sub>2</sub> as the sample is held at this 375 °C for over 24 h during the NaPON deposition. The use of NaO<sup>t</sup>Bu further enhances the likeliness for V<sup>5+</sup> → V<sup>4+</sup> reduction, as NaO<sup>t</sup>Bu is a strong base, readily willing to give up electrons towards V<sub>2</sub>O<sub>5</sub>. Cuthbertson et al.<sup>145</sup> provide a model for the reducing power of AO<sup>t</sup>Bu's (A = Li, Na, K), in which the alkoxide is in dynamic equilibrium between the covalent O-A and ionic O<sup>-</sup>-K<sup>+</sup> species. Additionally, the charge separated species can be considered as a species with a loosely bound electron. This electron can be readily transferred to initiate reduction reactions, such as V<sub>2</sub>O<sub>5</sub> reduction in this case. This reduction induced intermixing occurs for the first half of the NaPON deposition, giving rise to the ~40-50 nm mixing region below the 'pure' NaPON. The EELS analysis shows that V is more reduced in the bottom VO<sub>x</sub> layer than the mixing region. One explanation for this is the direct

exposure of the bottom  $\text{VO}_x$  surface to the reducing  $\text{NaO}^t\text{Bu}$ , whereas at the mixing layer the contents are already in a reduced state  $\text{NaVO}_2$  state and less susceptible to further reduction by  $\text{NaO}^t\text{Bu}$ . It is interesting that V diffusion occurs as well, with small amounts of V detected even in the top NaPON layer. This could be due to breakdown of the  $\text{VO}_6$  octahedra within the  $\text{V}_2\text{O}_5$  and  $\text{VO}_2$  layered structures with reaction during the NaPON deposition. Further TEM and EELS characterization will be performed to provide precise clarity to the intermixing process and specific components.

This work provides a warning for the higher difficulty and more complex nature of fabricating Na-SSBs as compared to Li-SSBs. The Li analogue to NaPON, LiPON, has been very successful as a thin-film SSE when paired with  $\text{V}_2\text{O}_5$  cathodes.<sup>10, 26, 146, 147</sup> Our group has demonstrated the ability for Li-SSB fabrication in a similar manner to that in this work, i.e. an ALD metal oxide electrode, ALD LiPON SSE, and a thermally evaporated Li metal anode, that being Li/LiPON/ $\text{V}_2\text{O}_5$  and Li/LiPON/ $\text{SnO}_2$ .<sup>10, 148</sup> It was expected that NaPON would have a similar compatibility with  $\text{V}_2\text{O}_5$  given its highly reversible  $\text{Na}^+$  electrochemistry and that the Na anode would not induce extreme reactions throughout the stack. The process of thermal Na metal evaporation is too reactive for deposition on NaPON/ $\text{V}_2\text{O}_5$ , however, this reactivity may be avoided if substrate cooling capabilities are implemented. This would require major lab infrastructure development and is beyond our current bandwidth.

Other strategies to realize the feat of a nanoscale Na-SSB are to use an ion-insertion anode material instead of using a Na metal anode. This would not require any external solution-based sodiation of electrode materials. Instead, this method could take advantage of the NaPON deposition on  $\text{V}_2\text{O}_5$ , resulting in a  $\text{NaVO}_2$  pre-sodiated cathode material. Metal oxides such as  $\text{SnO}_2$  and  $\text{TiO}_2$  are promising options for anodes. Both possess well-established ALD process and

have proven to be effective as anode materials in SIBs.<sup>21, 108, 110, 149</sup> Another creative option is to make use of a symmetric battery composed of a VO<sub>x</sub>-based anode and cathode. In doing so, the intermixing during the NaPON deposition could be taken advantage of, resulting in a pre-sodiated NaVO<sub>2</sub> as an anode and depositing V<sub>2</sub>O<sub>5</sub> as an un-sodiated cathode on top of NaPON/NaVO<sub>2</sub>. The V<sub>2</sub>O<sub>5</sub> ALD deposition is not presumed to result in intermixing in a similar manner that NaPON does during its deposition, because of the low deposition temperature of 170 °C.<sup>23</sup> Alternatively, a true symmetric VO<sub>2</sub> battery could be fabricated using the tetrakis[ethylmethylamino]vanadium (TEMAV) precursor for ALD deposition that contains V<sup>4+</sup> instead of V<sup>5+</sup> in VTOP. This thermal VO<sub>2</sub> process can also be grown at a low temperature of 150 °C.<sup>150, 151</sup> However, the as-deposited VO<sub>2</sub> film using the TEMAV precursor is amorphous, unlike the crystalline NaVO<sub>2</sub> layer formed during the ALD NaPON deposition. Ideally both electrodes should be crystalline or amorphous, but ALD VO<sub>2</sub> can be crystallized by a post-annealing at 450 °C.<sup>151</sup> The symmetric electrode configurations are promising, especially a NaVO<sub>2</sub>/V<sub>2</sub>O<sub>5</sub> electrode pair, which takes advantage of both the high rate pseudocapacitive intercalation behavior of VO<sub>2</sub> and the high voltage battery-type intercalation of V<sub>2</sub>O<sub>5</sub>. This combination allows for enhancement in energy density while operating at high rates. Dunn et al.<sup>143</sup> have extensively reviewed the pseudocapacitive properties of vanadium materials and proposed the fabrication of such next-generation sodium-ion capacitor/battery hybrid devices. Dunn et al.<sup>142</sup> have more recently reported on a symmetric SIB composed of amorphous VO<sub>2</sub> electrodes. The authors show the enhancement in pseudocapacitive behavior of amorphous VO<sub>2</sub>, exhibiting 90% capacitive controlled kinetics, whereas crystalline VO<sub>2</sub> is only 60% capacitive controlled. The pseudocapacitive intercalation behavior of amorphous VO<sub>2</sub> was attributed to facilitate high-rate performance with a high reversible capacity up to 400

mAh/g. A fully symmetric NaVO<sub>2</sub>/NaPON/VO<sub>2</sub> is a promising route towards realization of a thin-film Na-SSB.

## 5.7. Conclusions

The electrochemistry (with solid and liquid electrolytes) and interfacial characterization provide a cumulative insight into the fabrication of nanoscale Na-SSBs. In absence of an ion-insertion host, the NaPON SSE exhibits excellent stability with evaporated Na metal, displaying no electrolyte breakdown or conductivity loss when charged up to 6 V vs. Na/Na<sup>+</sup>. However, in SSB fabrication, intermixing of the NaPON/V<sub>2</sub>O<sub>5</sub> layers occur during the ALD NaPON deposition, and further reaction occurs during the Na metal evaporation step. X-ray photoelectron spectroscopy depth profiling and cryo-TEM analysis provide explanation to the underlying processing reactivity. The reaction during the ALD NaPON deposition on V<sub>2</sub>O<sub>5</sub> is two-fold: (1) reduction of V<sub>2</sub>O<sub>5</sub> to VO<sub>2</sub> and (2) Na<sup>+</sup> insertion into VO<sub>2</sub> to form Na<sub>x</sub>VO<sub>2</sub>. The Na metal evaporation process is found to exacerbate this reactivity, resulting in the formation of irreversible interphases leading to poor SSB performance. This work highlights the high reactivity of Na compared to Li, and the extreme caution needed for fabrication of Na-SSBs or liquid sodium-ion batteries, as interfacial coatings will certainly be required in liquid-based batteries. Despite the relatively poor battery performance, this work represents the first report of a fully nanoscale Na-SSB and showcases cryo-TEM as a powerful characterization technique for nanoscale SSBs.

Looking forward, the intermixing during the ALD NaPON deposition does not impact the cycling of the Na<sub>x</sub>VO<sub>2</sub> electrode in liquid-based cells, with it outperforming that of unsodiated V<sub>2</sub>O<sub>5</sub> electrodes. This may be advantageous for the fabrication of SSBs, as the SSE deposition simultaneously pre-sodiate a stable cathode material, excluding the need for *ex-situ* sodiation in liquid solutions or depositing a pre-sodiated electrode material. An all ALD fabricated symmetric

$\text{NaVO}_2/\text{NaPON}/\text{VO}_2$  or  $\text{NaVO}_2/\text{NaPON}/\text{V}_2\text{O}_5$  are promising routes that will be explored as next-generation energy storage devices.

## Chapter 6: Conclusions and Future Work

### 6.1. Conclusions

This dissertation contributes significant knowledge on the fabrication, materials chemistry, and electrochemistry of thin-film SSBs. The motivation for this work owes much to that accomplished during 11-year (2009-2020) Department of Energy funded Energy Frontier Research Center on Nanostructures for Electrical Energy Storage (NEES). Through this multi-institutional EFRC, our group and collaborators demonstrated the profound influence and capabilities of nanostructures on battery performance and novel methods for fabricating nanoscale battery materials. Our group's role in NEES culminated with the first fully conformal 3D nanoscale SSB by Pearse et al.<sup>10</sup> The key enabler of this achievement was the development of a thermal ALD process for the LiPON SSE. This dissertation sought to develop and characterize new solid electrolyte materials, namely NaPON and KPON, using micro-processing techniques for their incorporation in nanostructured beyond-lithium batteries.

The NaPON SSE is the primary focus of this thesis, and much time was devoted to characterizing the film and its incorporation in liquid and SSBs. This work represents the first report of a fully nanoscale Na-SSB. The interfacial reactions during ALD deposition of NaPON on  $V_2O_5$  and subsequent Na evaporation on NaPON were unexpected, as such reactivity was not previously observed for Li analogues, i.e. ALD LiPON SSE and Li evaporated anode.<sup>10, 148</sup> However, such processing related reactions in the Na-SSB invoked the use of cryo-TEM analysis, a powerful technique for characterizing highly reactive thin-films and their interfaces, proving to be fruitful for understanding underlying phenomena in SSBs. Though unfinished, this work provides profound knowledge and insight into the fabrication and electrochemistry of beyond-Li nanoscale SSBs.

In summary, the achievements of this dissertation include: (1) Development of the first reported ALD process of a Na-ion conducting film, NaPON. (2) Development of the first reported ALD process of a K-ion conducting film, KPON. (3) Demonstration of *in-operando* mass spectrometry to infer the underlying surface reactions of the ALD LiPON process and propose a reaction mechanism for the resulting film. (4) Fabrication and testing of a proof-of-principle nanoscale Na-SSB. (5) Development of a low temperature plasma-based ALD process for NaPON.

The body of work in this thesis resulted in the following publications:

1. **R.B. Nuwayhid**, A.C. Kozen, G.W. Rubloff, K.E. Gregorczyk. Nanoscale Solid-State Sodium-Ion Batteries Enabled by the Solid Electrolyte NaPON. *In preparation*.
2. D.M. Long, K.A. Small, **R.B. Nuwayhid**, A.C. Kozen, M. Singh, J.D. Watt. Cryo-FIB Lamella Preparation for TEM investigation of Soft- and Low-Z Materials. *In preparation*.
3. D. Fontecha, **R.B. Nuwayhid**, A.C. Kozen, G.W. Rubloff, K.E. Gregorczyk. Plasma Enhanced Atomic Layer Deposition of Sodium Phosphorus Oxynitride. *J. Vac. Sci. Technol. A*, **2022**, 40, 032403. DOI: 10.1116/6.0001752.
4. *Invited*: **R.B. Nuwayhid**, D. Fontecha, A.C. Kozen, G.W. Rubloff, K.E. Gregorczyk. Atomic Layer Deposition of Li, Na, and K ion-conducting phosphazenes. *Dalton Transactions* **2022**, 51, 2068-2082. DOI: 10.1039/d1dt03736f
5. **R. Blake Nuwayhid**, Angelique Jarry, Gary W. Rubloff, and Keith E. Gregorczyk. Atomic Layer Deposition of Sodium Phosphorus Oxynitride: A Conformal Solid-State Sodium-Ion Conductor. *ACS Applied Materials & Interfaces* **2020** 12 (19), 21641-21650. DOI: 10.1021/acsami.0c03578

## 6.2. Future Work

In an ideal lab in an ideal world, equipment issues are minimal. I would be remiss not to mention the significant equipment-induced downtime during this dissertation. In the final year (2021-2022) of this dissertation major delays were experienced and are recounted in this section. The ALD reactor, where all the NaPON SSE depositions were conducted, began experiencing trouble with its turbo pump in August 2021. This limited depositions on the tool that were longer than 2 hours because the turbo pump would overheat and shut off. Numerous solutions were tested

to solve the overheating issue, including shortening the vacuum backing line, installing new water-cooling lines, using an external water chiller, and cleaning out the cooled water loop of the turbo pump. After exhausting all options, it was determined the pump needed to be sent to its manufacturer (Edwards Vacuum) for repair. Edwards Vacuum attempted to send us back a repaired pump in November 2021, however we received an empty box. The pump was located in January 2022 and required further repair which was further delayed due to on-going COVID-19 related supply chain issues. Due to negligence of Edwards Vacuum, as I am writing this in April 2022, said turbo pump has still not been returned to UMD. This repair delay significantly impacted experimental progress, specifically bringing all Na-SSB fabrication to a halt, and thus preventing testing and characterization of devices. Needless to say, there are plenty of experiments left to be considered. A few future experiments are discussed below.

1. Fabricate new Na/NaPON/V<sub>2</sub>O<sub>5</sub> SSBs and send to collaborators at the Center for Integrated Nanotechnologies (CINT) at Sandia National Laboratory for cryo-TEM analysis. We were not able to characterize the full Na-SSB to the extent we did the Au/NaPON/V<sub>2</sub>O<sub>5</sub> sample with the cryo-TEM and EELS. This would provide a more detailed insight into the interphases in the Na capped sample. The first results we have lack sharp edges of the layers and is possibly due to aging of the samples.
2. Fabricate a symmetric Na<sub>x</sub>VO<sub>2</sub>/NaPON/VO<sub>2</sub> or Na<sub>x</sub>VO<sub>2</sub>/NaPON/V<sub>2</sub>O<sub>5</sub> SSB. As evidenced in Chapter 5, the NaPON deposition results in a pre-sodiated Na<sub>x</sub>VO<sub>2</sub> electrode. The V<sub>2</sub>O<sub>5</sub> ALD deposition is not presumed to result in intermixing in a similar manner that NaPON does during its deposition, because of the low deposition temperature of 170 °C.<sup>23</sup> Alternatively, a true symmetric VO<sub>2</sub> battery could be fabricated using the tetrakis[ethylmethylamino]vanadium (TEMAV) precursor for

ALD deposition that contains  $V^{4+}$  instead of  $V^{5+}$  in VTOP. This thermal  $VO_2$  process can also be grown at a low temperature of 150 °C.<sup>150, 151</sup> However, the as-deposited  $VO_2$  film using the TEMAV precursor is amorphous, unlike the crystalline  $NaVO_2$  layer formed during the ALD NaPON deposition. Ideally both electrodes should be crystalline or amorphous, but ALD  $VO_2$  can be crystallized by a post-annealing at 450 °C.<sup>151</sup>

3. Achieving a SSB with deposition of a non-vanadium based anode material on top of the NaPON/ $NaVO_x$  electrolyte/electrode. Metal oxides such as  $SnO_2$  and  $TiO_2$  are promising options for anodes. Both possess well-established ALD process and have proven to be effective as anode materials in SIBs.<sup>21, 108, 110, 149</sup>
4. Exploring the reaction ALD reaction of KPON and further electrochemical characterization of the resulting film. *In-operando* QMS of KO<sup>t</sup>Bu-DEPA would aid in understanding the reaction mechanism by distinguishing different species desorbing from the surface than the LiPON and NaPON processes. Furthermore, in an attempt to develop an ALD process for a fully nitrogenated KPON film, alternative reaction schemes should be performed. For instance, we have had success growing LiPON and NaPON plasma-based ALD processes<sup>36</sup>, which are essentially  $Li_3PO_4/Na_3PO_4$  processes with an added nitrogen plasma pulse to dope the alkali phosphate. The base potassium phosphate has not been demonstrated but is believed to be plausible, based on the simple reaction sequence of AO<sup>t</sup>Bu- $H_2O$ -TMP. The addition of  $N_2$  plasma to a  $K_3PO_4$  process may be able to overcome the steric energy barrier to incorporate nitrogen into the film. If this proves unsuccessful, further novel precursors are worth exploring.

5. Exploring ALD synthesis of mixed alkali PON SSEs. Lopez et al.<sup>152</sup> have reported a room temperature ionic conductivity of  $6.5 \times 10^{-6}$  S/cm for  $\text{Li}_2\text{NaPO}_4$ , which is more than an order of magnitude higher than that the nominal  $\gamma\text{-Li}_3\text{PO}_4$  ( $4.0 \times 10^{-7}$  S/cm). This is a result of the decreased ionic migration energy barrier with the larger Na atom in the phosphate structure. The authors also provided theoretical calculations predicting a further enhancement in ionic conductivity with the replacement of Na with the larger K atom to form  $\text{Li}_2\text{KPO}_4$ . A similar behavior may occur for LiPON with Na or K doping, which could be done with high controllability by alternating ALD processes. Numerous combinations combining the alkali PON/oxide/phosphate/nitride processes can be explored.

## Bibliography

1. Takada, K., Progress and prospective of solid-state lithium batteries. *Acta Materialia* **2013**, *61* (3), 759-770.
2. Sun, C.; Liu, J.; Gong, Y.; Wilkinson, D. P.; Zhang, J., Recent advances in all-solid-state rechargeable lithium batteries. *Nano Energy* **2017**, *33*, 363-386.
3. Manthiram, A.; Yu, X.; Wang, S., Lithium battery chemistries enabled by solid-state electrolytes. *Nature Reviews Materials* **2017**, *2* (4), 16103.
4. Yabuuchi, N.; Kubota, K.; Dahbi, M.; Komaba, S., Research development on sodium-ion batteries. *Chem Rev* **2014**, *114* (23), 11636-11682.
5. Zhao, Y.; Zheng, K.; Sun, X., Addressing Interfacial Issues in Liquid-Based and Solid-State Batteries by Atomic and Molecular Layer Deposition. *Joule* **2018**, *2* (12), 2583-2604.
6. Meng, X.; Yang, X.-Q.; Sun, X., Emerging Applications of Atomic Layer Deposition for Lithium-Ion Battery Studies. *Advanced Materials* **2012**, *24* (27), 3589-3615.
7. Lin, C.-F.; Qi, Y.; Gregorczyk, K.; Lee, S. B.; Rubloff, G. W., Nanoscale Protection Layers To Mitigate Degradation in High-Energy Electrochemical Energy Storage Systems. *Accounts of Chemical Research* **2018**, *51* (1), 97-106.
8. Noked, M.; Liu, C.; Hu, J.; Gregorczyk, K.; Rubloff, G. W.; Lee, S. B., Electrochemical Thin Layers in Nanostructures for Energy Storage. *Accounts of Chemical Research* **2016**, *49* (10), 2336-2346.
9. Moitzheim, S.; Put, B.; Vereecken, P. M., Advances in 3D Thin-Film Li-Ion Batteries. *Advanced Materials Interfaces* **2019**, *6* (15).
10. Pearse, A.; Schmitt, T.; Sahadeo, E.; Stewart, D. M.; Kozen, A.; Gerasopoulos, K.; Talin, A. A.; Lee, S. B.; Rubloff, G. W.; Gregorczyk, K. E., Three-Dimensional Solid-State Lithium-Ion Batteries Fabricated by Conformal Vapor-Phase Chemistry. *ACS Nano* **2018**, *12* (5), 4286-4294.
11. Long, J. W.; Dunn, B.; Rolison, D. R.; White, H. S., Three-Dimensional Battery Architectures. *Chemical Reviews* **2004**, *104* (10), 4463-4492.
12. Oudenhoven, J. F. M.; Baggetto, L.; Notten, P. H. L., All-Solid-State Lithium-Ion Microbatteries: A Review of Various Three-Dimensional Concepts. *Advanced Energy Materials* **2011**, *1* (1), 10-33.
13. Talin, A. A.; Ruzmetov, D.; Kolmakov, A.; McKelvey, K.; Ware, N.; El Gabaly, F.; Dunn, B.; White, H. S., Fabrication, Testing, and Simulation of All-Solid-State Three-Dimensional Li-Ion Batteries. *ACS Applied Materials & Interfaces* **2016**, *8* (47), 32385-32391.
14. George, S. M., Atomic layer deposition: an overview. *Chemical reviews* **2009**, *110* (1), 111-131.
15. Cremers, V.; Puurunen, R. L.; Dendooven, J., Conformality in atomic layer deposition: Current status overview of analysis and modelling. *Applied Physics Reviews* **2019**, *6* (2), 021302.
16. Miikkulainen, V.; Leskelä, M.; Ritala, M.; Puurunen, R. L., Crystallinity of inorganic films grown by atomic layer deposition: Overview and general trends. *Journal of Applied Physics* **2013**, *113* (2), 021301.

17. Zhao, Y.; Zhang, L.; Liu, J.; Adair, K.; Zhao, F.; Sun, Y.; Wu, T.; Bi, X.; Amine, K.; Lu, J.; Sun, X., Atomic/molecular layer deposition for energy storage and conversion. *Chemical Society Reviews* **2021**, *50* (6), 3889-3956.
18. George, S. M.; Sneh, O.; Dillon, A. C.; Wise, M. L.; Ott, A. W.; Okada, L. A.; Way, J. D., Atomic layer controlled deposition of SiO<sub>2</sub> and Al<sub>2</sub>O<sub>3</sub> using ABAB... binary reaction sequence chemistry. *Applied Surface Science* **1994**, *82-83*, 460-467.
19. Ma, L.; Nuwayhid, R. B.; Wu, T.; Lei, Y.; Amine, K.; Lu, J., Atomic Layer Deposition for Lithium-Based Batteries. *Advanced Materials Interfaces* **2016**, *3* (21), 1600564.
20. Han, L.; Hsieh, C.-T.; Chandra Mallick, B.; Li, J.; Ashraf Gandomi, Y., Recent progress and future prospects of atomic layer deposition to prepare/modify solid-state electrolytes and interfaces between electrodes for next-generation lithium batteries. *Nanoscale Advances* **2021**, *3* (10), 2728-2740.
21. Wang, H.; Jia, G.; Guo, Y.; Zhang, Y.; Geng, H.; Xu, J.; Mai, W.; Yan, Q.; Fan, H. J., Atomic Layer Deposition of Amorphous TiO<sub>2</sub> on Carbon Nanotube Networks and Their Superior Li and Na Ion Storage Properties. *Advanced Materials Interfaces* **2016**, *3* (21), 1600375.
22. Aravindan, V.; Jinesh, K. B.; Prabhakar, R. R.; Kale, V. S.; Madhavi, S., Atomic layer deposited (ALD) SnO<sub>2</sub> anodes with exceptional cycleability for Li-ion batteries. *Nano Energy* **2013**, *2* (5), 720-725.
23. Chen, X.; Pomerantseva, E.; Banerjee, P.; Gregorczyk, K.; Ghodssi, R.; Rubloff, G., Ozone-Based Atomic Layer Deposition of Crystalline V<sub>2</sub>O<sub>5</sub> Films for High Performance Electrochemical Energy Storage. *Chemistry of Materials* **2012**, *24* (7), 1255-1261.
24. Donders, M. E.; Arnoldbik, W. M.; Knoops, H. C. M.; Kessels, W. M. M.; Notten, P. H. L., Atomic Layer Deposition of LiCoO<sub>2</sub> Thin-Film Electrodes for All-Solid-State Li-Ion Micro-Batteries. *Journal of The Electrochemical Society* **2013**, *160* (5), A3066-A3071.
25. Sheil, R.; Butts, D.; Jungjohann, K.; Yoo, J.; Dunn, B.; Chang, J. P., Plasma enhanced atomic layer deposition of thin film Li<sub>1+x</sub>Mn<sub>2-x</sub>O<sub>4</sub> for realization of all solid-state 3D lithium-ion microbatteries. *Journal of Vacuum Science & Technology A* **2021**, *39* (1), 012408.
26. Bates, J. B.; Dudney, N. J.; Gruzalski, G. R.; Zuhr, R. A.; Choudhury, A.; Luck, C. F.; Robertson, J. D., Fabrication and characterization of amorphous lithium electrolyte thin films and rechargeable thin-film batteries. *Journal of Power Sources* **1993**, *43* (1), 103-110.
27. Bates, J. B.; Dudney, N. J.; Gruzalski, G. R.; Zuhr, R. A.; Choudhury, A.; Luck, C. F.; Robertson, J. D., Electrical properties of amorphous lithium electrolyte thin films. *Solid State Ionics* **1992**, *53-56*, 647-654.
28. LaCoste, J. D.; Zakutayev, A.; Fei, L., A Review on Lithium Phosphorus Oxynitride. *The Journal of Physical Chemistry C* **2021**, *125* (7), 3651-3667.
29. Lacivita, V.; Artrith, N.; Ceder, G., Structural and Compositional Factors That Control the Li-Ion Conductivity in LiPON Electrolytes. *Chemistry of Materials* **2018**, *30* (20), 7077-7090.
30. Lacivita, V.; Westover, A. S.; Kercher, A.; Phillip, N. D.; Yang, G.; Veith, G.; Ceder, G.; Dudney, N. J., Resolving the Amorphous Structure of Lithium Phosphorus Oxynitride (Lipon). *J Am Chem Soc* **2018**, *140* (35), 11029-11038.
31. Fleutot, B.; Pecquenard, B.; Martinez, H.; Letellier, M.; Levasseur, A., Investigation of the local structure of LiPON thin films to better understand the role of nitrogen on their performance. *Solid State Ionics* **2011**, *186* (1), 29-36.

32. Wang, B.; Kwak, B. S.; Sales, B. C.; Bates, J. B., Ionic conductivities and structure of lithium phosphorus oxynitride glasses. *Journal of Non-Crystalline Solids* **1995**, *183* (3), 297-306.
33. Shibata, S., Thermal Atomic Layer Deposition of Lithium Phosphorus Oxynitride as a Thin-Film Solid Electrolyte. *Journal of The Electrochemical Society* **2016**, *163* (13), A2555-A2562.
34. Nisula, M.; Shindo, Y.; Koga, H.; Karppinen, M., Atomic Layer Deposition of Lithium Phosphorus Oxynitride. *Chemistry of Materials* **2015**, *27* (20), 6987-6993.
35. Pearse, A. J.; Schmitt, T. E.; Fuller, E. J.; El-Gabaly, F.; Lin, C.-F.; Gerasopoulos, K.; Kozen, A. C.; Talin, A. A.; Rubloff, G.; Gregorczyk, K. E., Nanoscale Solid State Batteries Enabled by Thermal Atomic Layer Deposition of a Lithium Polyphosphazene Solid State Electrolyte. *Chemistry of Materials* **2017**, *29* (8), 3740-3753.
36. Kozen, A. C.; Pearse, A. J.; Lin, C.-F.; Noked, M.; Rubloff, G. W., Atomic Layer Deposition of the Solid Electrolyte LiPON. *Chemistry of Materials* **2015**, *27* (15), 5324-5331.
37. Allcock, H. R.; Desorcie, J. L.; Riding, G. H., The organometallic chemistry of phosphazenes. *Polyhedron* **1987**, *6* (2), 119-157.
38. Allcock, H. R., Recent advances in phosphazene (phosphonitrilic) chemistry. *Chemical Reviews* **1972**, *72* (4), 315-356.
39. United States Geological Survey. In *Mineral Commodity Summaries*, Reston, VA, 2021; p 200.
40. Newman, G. H.; Klemann, L. P., Ambient Temperature Cycling of an Na - TiS<sub>2</sub> Cell. *Journal of The Electrochemical Society* **1980**, *127* (10), 2097-2099.
41. Nagelberg, A. S.; Worrell, W. L., A thermodynamic study of sodium-intercalated TaS<sub>2</sub> and TiS<sub>2</sub>. *Journal of Solid State Chemistry* **1979**, *29* (3), 345-354.
42. Whittingham, M. S., Chemistry of intercalation compounds: Metal guests in chalcogenide hosts. *Progress in Solid State Chemistry* **1978**, *12* (1), 41-99.
43. Whittingham, M. S., Electrical Energy Storage and Intercalation Chemistry. *Science* **1976**, *192* (4244), 1126-1127.
44. Goodenough, J. B.; Hong, H. Y. P.; Kafalas, J. A., Fast Na<sup>+</sup>-ion transport in skeleton structures. *Materials Research Bulletin* **1976**, *11* (2), 203-220.
45. Hueso, K. B.; Armand, M.; Rojo, T., High temperature sodium batteries: status, challenges and future trends. *Energy & Environmental Science* **2013**, *6* (3), 734-749.
46. Ellis, B. L.; Nazar, L. F., Sodium and sodium-ion energy storage batteries. *Current Opinion in Solid State and Materials Science* **2012**, *16* (4), 168-177.
47. Hayashi, A.; Noi, K.; Sakuda, A.; Tatsumisago, M., Superionic glass-ceramic electrolytes for room-temperature rechargeable sodium batteries. *Nature Communications* **2012**, *3* (1), 856.
48. Chu, I.-H.; Kompella, C. S.; Nguyen, H.; Zhu, Z.; Hy, S.; Deng, Z.; Meng, Y. S.; Ong, S. P., Room-temperature all-solid-state rechargeable sodium-ion batteries with a Cl-doped Na<sub>3</sub>PS<sub>4</sub> superionic conductor. *Scientific reports* **2016**, *6*, 33733.
49. Banerjee, A.; Park, K. H.; Heo, J. W.; Nam, Y. J.; Moon, C. K.; Oh, S. M.; Hong, S. T.; Jung, Y. S., Na<sub>3</sub>SbS<sub>4</sub>: A Solution Processable Sodium Superionic Conductor for All-Solid-State Sodium-Ion Batteries. *Angewandte Chemie International Edition* **2016**, *55* (33), 9634-9638.
50. Richards, W. D.; Tsujimura, T.; Miara, L. J.; Wang, Y.; Kim, J. C.; Ong, S. P.; Uechi, I.; Suzuki, N.; Ceder, G., Design and synthesis of the superionic conductor Na<sub>10</sub>SnP<sub>2</sub>S<sub>12</sub>. *Nature communications* **2016**, *7*, 11009.

51. Yu, Z.; Shang, S. L.; Seo, J. H.; Wang, D.; Luo, X.; Huang, Q.; Chen, S.; Lu, J.; Li, X.; Liu, Z. K., Exceptionally High Ionic Conductivity in Na<sub>3</sub>P<sub>0.62</sub>As<sub>0.38</sub>S<sub>4</sub> with Improved Moisture Stability for Solid-State Sodium-Ion Batteries. *Advanced materials* **2017**, *29* (16), 1605561.
52. Doeff, M. M.; Visco, S. J.; Ma, Y. P.; Peng, M.; Ding, L.; Dejonghe, L. C., Thin-Film Solid-State Sodium Batteries for Electric Vehicles. *Electrochimica Acta* **1995**, *40* (13-14), 2205-2210.
53. Bang, Y.-I.; Song, K.-D.; Joo, B.-S.; Huh, J.-S.; Choi, S.-D.; Lee, D.-D., Thin film micro carbon dioxide sensor using MEMS process. *Sensors and Actuators B: Chemical* **2004**, *102* (1), 20-26.
54. Horwat, D.; Pierson, J. F.; Billard, A., Towards a thin films electrochromic device using NASICON electrolyte. *Ionics* **2007**, *14* (3), 227-233.
55. Chun, S.-E., Characterization of RF Sputter-deposited Sodium Phosphorous Oxynitride Thin Films as a Solid-state Sodium-ion Conductor. *Journal of the Korean institute of surface engineering* **2017**, *50* (4), 237-243.
56. Nuwayhid, R. B.; Jarry, A.; Rubloff, G. W.; Gregorczyk, K. E., Atomic Layer Deposition of Sodium Phosphorus Oxynitride: A Conformal Solid-State Sodium-Ion Conductor. *ACS Applied Materials & Interfaces* **2020**, *12* (19), 21641-21650.
57. Zhang, Z.; Zhang, Q.; Shi, J.; Chu, Y. S.; Yu, X.; Xu, K.; Ge, M.; Yan, H.; Li, W.; Gu, L.; Hu, Y.-S.; Li, H.; Yang, X.-Q.; Chen, L.; Huang, X., A Self-Forming Composite Electrolyte for Solid-State Sodium Battery with Ultralong Cycle Life. *Advanced Energy Materials* **2017**, *7* (4), 1601196.
58. Hooper, A., A study of the electrical properties of single-crystal and polycrystalline  $\beta$ -alumina using complex plane analysis. *Journal of Physics D: Applied Physics* **1977**, *10* (11), 1487-1496.
59. Baffier, N.; Badot, J. C.; Colomban, P., Conductivity of ion rich  $\beta$  and  $\beta''$  alumina: Sodium and potassium compounds. *Materials Research Bulletin* **1981**, *16* (3), 259-265.
60. Richards, W. D.; Tsujimura, T.; Miara, L. J.; Wang, Y.; Kim, J. C.; Ong, S. P.; Uechi, I.; Suzuki, N.; Ceder, G., Design and synthesis of the superionic conductor Na<sub>10</sub>SnP<sub>2</sub>S<sub>12</sub>. *Nat Commun* **2016**, *7*, 11009.
61. Rao, R. P.; Chen, H.; Wong, L. L.; Adams, S., Na<sub>3+x</sub>M<sub>x</sub>P<sub>1-x</sub>S<sub>4</sub> (M = Ge<sup>4+</sup>, Ti<sup>4+</sup>, Sn<sup>4+</sup>) enables high rate all-solid-state Na-ion batteries Na<sub>2+2 $\delta$</sub> Fe<sub>2- $\delta$</sub> (SO<sub>4</sub>)<sub>3</sub>|Na<sub>3+x</sub>M<sub>x</sub>P<sub>1-x</sub>S<sub>4</sub>|Na<sub>2</sub>Ti<sub>3</sub>O<sub>7</sub>. *J. Mater. Chem. A* **2017**, *5* (7), 3377-3388.
62. Yu, Z.; Shang, S. L.; Seo, J. H.; Wang, D.; Luo, X.; Huang, Q.; Chen, S.; Lu, J.; Li, X.; Liu, Z. K.; Wang, D., Exceptionally High Ionic Conductivity in Na<sub>3</sub> P<sub>0.62</sub> As<sub>0.38</sub> S<sub>4</sub> with Improved Moisture Stability for Solid-State Sodium-Ion Batteries. *Adv Mater* **2017**, *29* (16).
63. Jansen, M.; Henseler, U., Synthesis, structure determination, and ionic conductivity of sodium tetrathiosphosphate. *Journal of Solid State Chemistry* **1992**, *99* (1), 110-119.
64. Noi, K.; Hayashi, A.; Tatsumisago, M., Structure and properties of the Na<sub>2</sub>S–P<sub>2</sub>S<sub>5</sub> glasses and glass–ceramics prepared by mechanical milling. *Journal of Power Sources* **2014**, *269*, 260-265.
65. Tanibata, N.; Noi, K.; Hayashi, A.; Tatsumisago, M., Preparation and characterization of highly sodium ion conducting Na<sub>3</sub>PS<sub>4</sub>–Na<sub>4</sub>Si<sub>4</sub> solid electrolytes. *RSC Adv.* **2014**, *4* (33), 17120-17123.

66. Hibi, Y.; Tanibata, N.; Hayashi, A.; Tatsumisago, M., Preparation of sodium ion conducting Na<sub>3</sub>PS<sub>4</sub>–NaI glasses by a mechanochemical technique. *Solid State Ionics* **2015**, *270*, 6-9.
67. Zhang, L.; Yang, K.; Mi, J.; Lu, L.; Zhao, L.; Wang, L.; Li, Y.; Zeng, H., Na<sub>3</sub>PSe<sub>4</sub>: A Novel Chalcogenide Solid Electrolyte with High Ionic Conductivity. *Advanced Energy Materials* **2015**, *5* (24).
68. Sadikin, Y.; Brighi, M.; Schouwink, P.; Černý, R., Superionic Conduction of Sodium and Lithium in Anion-Mixed Hydroborates Na<sub>3</sub>BH<sub>4</sub>B<sub>12</sub>H<sub>12</sub> and (Li<sub>0.7</sub>Na<sub>0.3</sub>)<sub>3</sub>BH<sub>4</sub>B<sub>12</sub>H<sub>12</sub>. *Advanced Energy Materials* **2015**, *5* (21).
69. Duchêne, L.; Kühnel, R. S.; Rentsch, D.; Remhof, A.; Hagemann, H.; Battaglia, C., A highly stable sodium solid-state electrolyte based on a dodeca/deca-borate equimolar mixture. *Chemical Communications* **2017**, *53* (30), 4195-4198.
70. Yoshida, K.; Sato, T.; Unemoto, A.; Matsuo, M.; Ikeshoji, T.; Udovic, T. J.; Orimo, S.-i., Fast sodium ionic conduction in Na<sub>2</sub>B<sub>10</sub>H<sub>10</sub>–Na<sub>2</sub>B<sub>12</sub>H<sub>12</sub> pseudo-binary complex hydride and application to a bulk-type all-solid-state battery. *Applied Physics Letters* **2017**, *110* (10), 103901.
71. Wang, Y.; Wang, Q.; Liu, Z.; Zhou, Z.; Li, S.; Zhu, J.; Zou, R.; Wang, Y.; Lin, J.; Zhao, Y., Structural manipulation approaches towards enhanced sodium ionic conductivity in Na-rich antiperovskites. *Journal of Power Sources* **2015**, *293*, 735-740.
72. Gao, H.; Xue, L.; Xin, S.; Park, K.; Goodenough, J. B., A Plastic–Crystal Electrolyte Interphase for All-Solid-State Sodium Batteries. *Angewandte Chemie International Edition* **2017**, *56* (20), 5541-5545.
73. Ni'mah, Y. L.; Cheng, M.-Y.; Cheng, J. H.; Rick, J.; Hwang, B.-J., Solid-state polymer nanocomposite electrolyte of TiO<sub>2</sub>/PEO/NaClO<sub>4</sub> for sodium ion batteries. *Journal of Power Sources* **2015**, *278*, 375-381.
74. Zhang, C.; Gamble, S.; Ainsworth, D.; Slawin, A. M. Z.; Andreev, Y. G.; Bruce, P. G., Alkali metal crystalline polymer electrolytes. *Nature Materials* **2009**, *8* (7), 580-584.
75. Ponrouch, A.; Marchante, E.; Courty, M.; Tarascon, J.-M.; Palacín, M. R., In search of an optimized electrolyte for Na-ion batteries. *Energy & Environmental Science* **2012**, *5* (9), 8572-8583.
76. Einstein, A., On a heuristic point of view concerning the production and transformation of light. *Annalen der Physik* **1905**, *17* (132), 1-18.
77. Fujiwara, H., *Spectroscopic ellipsometry: principles and applications*. John Wiley & Sons: Tokyo, Japan, 2007.
78. Bard, A. J.; Faulkner, L. R., *Electrochemical methods: fundamentals and applications*. Wiley: New York, 2001.
79. Tarascon, J.-M., Is lithium the new gold? *Nature Chemistry* **2010**, *2* (6), 510-510.
80. Hwang, J. Y.; Myung, S. T.; Sun, Y. K., Sodium-ion batteries: present and future. *Chem Soc Rev* **2017**, *46* (12), 3529-3614.
81. Braconnier, J.-J.; Delmas, C.; Fouassier, C.; Hagenmuller, P., Comportement électrochimique des phases Na<sub>x</sub>CoO<sub>2</sub>. *Materials Research Bulletin* **1980**, *15* (12), 1797-1804.
82. Parant, J.-P.; Olazcuaga, R.; Devalette, M.; Fouassier, C.; Hagenmuller, P., Sur quelques nouvelles phases de formule Na<sub>x</sub>MnO<sub>2</sub> (x ≤ 1). *Journal of Solid State Chemistry* **1971**, *3* (1), 1-11.
83. Choi, J. W.; Aurbach, D., Promise and reality of post-lithium-ion batteries with high energy densities. *Nature Reviews Materials* **2016**, *1* (4).

84. Vaalma, C.; Buchholz, D.; Weil, M.; Passerini, S., A cost and resource analysis of sodium-ion batteries. *Nature Reviews Materials* **2018**, *3* (4), 18013.
85. United States Geological Survey. In *Mineral Commodity Summaries*, Reston, VA, 2020; p 204.
86. Meng, X., Atomic-scale surface modifications and novel electrode designs for high-performance sodium-ion batteries via atomic layer deposition. *J. Mater. Chem. A* **2017**, *5* (21), 10127-10149.
87. Sinha, S.; Didwal, P. N.; Nandi, D. K.; Cho, J. Y.; Kim, S.-H.; Park, C.-J.; Heo, J., Atomic layer deposited-ZnO@3D-Ni-foam composite for Na-ion battery anode: A novel route for easy and efficient electrode preparation. *Ceramics International* **2019**, *45* (1), 1084-1092.
88. Sreedhara, M. B.; Gope, S.; Vishal, B.; Datta, R.; Bhattacharyya, A. J.; Rao, C. N. R., Atomic layer deposition of crystalline epitaxial MoS<sub>2</sub> nanowall networks exhibiting superior performance in thin-film rechargeable Na-ion batteries. *J. Mater. Chem. A* **2018**, *6* (5), 2302-2310.
89. Liu, J.; Banis, M. N.; Xiao, B.; Sun, Q.; Lushington, A.; Li, R.; Guo, J.; Sham, T.-K.; Sun, X., Atomically precise growth of sodium titanates as anode materials for high-rate and ultralong cycle-life sodium-ion batteries. *J. Mater. Chem. A* **2015**, *3* (48), 24281-24288.
90. Dudney, N. J., Solid-state thin-film rechargeable batteries. *Materials Science and Engineering: B* **2005**, *116* (3), 245-249.
91. Hämäläinen, J.; Holopainen, J.; Munnik, F.; Hatanpää, T.; Heikkilä, M.; Ritala, M.; Leskelä, M., Lithium Phosphate Thin Films Grown by Atomic Layer Deposition. *Journal of The Electrochemical Society* **2012**, *159* (3), A259-A263.
92. Kozen, A. C.; Pearse, A. J.; Lin, C.-F.; Schroeder, M. A.; Noked, M.; Lee, S. B.; Rubloff, G. W., Atomic Layer Deposition and in Situ Characterization of Ultraclean Lithium Oxide and Lithium Hydroxide. *The Journal of Physical Chemistry C* **2014**, *118* (48), 27749-27753.
93. Ostreng, E.; Sonstebj, H. H.; Oien, S.; Nilsen, O.; Fjellvag, H., Atomic layer deposition of sodium and potassium oxides: evaluation of precursors and deposition of thin films. *Dalton Trans* **2014**, *43* (44), 16666-16672.
94. Gaskell, K. J.; Asunskis, A. L.; Sherwood, P. M., Sodium Polyphosphate (Na<sub>4</sub>P<sub>4</sub>O<sub>12</sub>) by XPS. *Surface Science Spectra* **2002**, *9* (1), 151-158.
95. Gaskell, K. J.; Asunskis, A. L.; Sherwood, P. M., Sodium Pyrophosphate Decahydrate (Na<sub>4</sub>P<sub>2</sub>O<sub>7</sub> · 10H<sub>2</sub>O) by XPS. *Surface Science Spectra* **2002**, *9* (1), 135-142.
96. Brow, R. K.; Reidmeyer, M. R.; Day, D. E., Oxygen bonding in nitrated sodium- and lithium-metaphosphate glasses. *Journal of Non-Crystalline Solids* **1988**, *99* (1), 178-189.
97. Reidmeyer, M. R.; Day, D. E.; Brow, R. K., Phosphorus oxynitride glasses of variable sodium content. *Journal of Non-Crystalline Solids* **1994**, *177*, 208-215.
98. Reidmeyer, M. R.; Day, D. E., Phosphorus oxynitride glasses. *Journal of Non-Crystalline Solids* **1995**, *181* (3), 201-214.
99. Marchand, R.; Agliz, D.; Boukbir, L.; Quemerais, A., Characterization of nitrogen containing phosphate glasses by X-ray photoelectron spectroscopy. *Journal of Non-Crystalline Solids* **1988**, *103* (1), 35-44.
100. Liu, J.; Banis, M. N.; Li, X.; Lushington, A.; Cai, M.; Li, R.; Sham, T.-K.; Sun, X., Atomic Layer Deposition of Lithium Tantalate Solid-State Electrolytes. *The Journal of Physical Chemistry C* **2013**, *117* (39), 20260-20267.

101. Perng, Y.-C.; Cho, J.; Sun, S. Y.; Membreno, D.; Cirigliano, N.; Dunn, B.; Chang, J. P., Synthesis of ion conducting  $\text{Li}_x\text{Al}_y\text{Si}_z\text{O}$  thin films by atomic layer deposition. *Journal of Materials Chemistry A* **2014**, *2* (25), 9566-9573.
102. Østreg, E.; Sønsteby, H. H.; Sajavaara, T.; Nilsen, O.; Fjellvåg, H., Atomic layer deposition of ferroelectric  $\text{LiNbO}_3$ . *Journal of Materials Chemistry C* **2013**, *1* (27), 4283-4290.
103. Desmaison-Brut, M.; Desmaison, J.; Verdier, P., Oxidation behaviour of an oxynitride glass in the system  $\text{Ca-Si-Al-O-N}$ . *Journal of Non-Crystalline Solids* **1988**, *105* (3), 323-329.
104. O'Meara, C.; Dunlop, G. L.; Pompe, R., Formation, crystallisation and oxidation of selected glasses in the  $\text{Y-Si-Al-O-N}$  system. *Journal of the European Ceramic Society* **1991**, *8* (3), 161-170.
105. Wusirika, R. R., Oxidation Behavior of Oxynitride Glasses. *Journal of the American Ceramic Society* **1985**, *68* (11), C-294-C-297.
106. Paraschiv, G. L.; Muñoz, F.; Jensen, L. R.; Yue, Y.; Smedskjaer, M. M., Structural stability of NaPON glass upon heating in air and nitrogen. *Journal of Non-Crystalline Solids* **2018**, *482*, 137-146.
107. Wang, Q.; Xu, J.; Zhang, W.; Mao, M.; Wei, Z.; Wang, L.; Cui, C.; Zhu, Y.; Ma, J., Research progress on vanadium-based cathode materials for sodium ion batteries. *J. Mater. Chem. A* **2018**, *6* (19), 8815-8838.
108. Su, D.; Dou, S.; Wang, G., Anatase  $\text{TiO}_2$ : Better Anode Material Than Amorphous and Rutile Phases of  $\text{TiO}_2$  for Na-Ion Batteries. *Chemistry of Materials* **2015**, *27* (17), 6022-6029.
109. Wang, H.; Jia, G.; Guo, Y.; Zhang, Y.; Geng, H.; Xu, J.; Mai, W.; Yan, Q.; Fan, H. J., Atomic Layer Deposition of Amorphous  $\text{TiO}_2$  on Carbon Nanotube Networks and Their Superior Li and Na Ion Storage Properties. *Advanced Materials Interfaces* **2016**, *3* (21).
110. Su, D.; Wang, C.; Ahn, H.; Wang, G., Octahedral tin dioxide nanocrystals as high capacity anode materials for Na-ion batteries. *Phys Chem Chem Phys* **2013**, *15* (30), 12543-12550.
111. Cras, F. L.; Pecquenard, B.; Dubois, V.; Phan, V.-P.; Guy-Bouyssou, D., All-Solid-State Lithium-Ion Microbatteries Using Silicon Nanofilm Anodes: High Performance and Memory Effect. *Advanced Energy Materials* **2015**, *5* (19), 1501061.
112. Khan, Y.; Ostfeld, A. E.; Lochner, C. M.; Pierre, A.; Arias, A. C., Monitoring of Vital Signs with Flexible and Wearable Medical Devices. *Advanced Materials* **2016**, *28* (22), 4373-4395.
113. Liu, C.; Gillette, E. I.; Chen, X.; Pearse, A. J.; Kozen, A. C.; Schroeder, M. A.; Gregorczyk, K. E.; Lee, S. B.; Rubloff, G. W., An all-in-one nanopore battery array. *Nature Nanotechnology* **2014**, *9* (12), 1031-1039.
114. Banerjee, P.; Perez, I.; Henn-Lecordier, L.; Lee, S. B.; Rubloff, G. W., Nanotubular metal-insulator-metal capacitor arrays for energy storage. *Nature Nanotechnology* **2009**, *4* (5), 292-296.
115. Aaltonen, T.; Nilsen, O.; Magrasó, A.; Fjellvåg, H., Atomic Layer Deposition of  $\text{Li}_2\text{O-Al}_2\text{O}_3$  Thin Films. *Chemistry of Materials* **2011**, *23* (21), 4669-4675.
116. Perng, Y.-C.; Cho, J.; Sun, S. Y.; Membreno, D.; Cirigliano, N.; Dunn, B.; Chang, J. P., Synthesis of ion conducting  $\text{Li}_x\text{Al}_y\text{Si}_z\text{O}$  thin films by atomic layer deposition. *J. Mater. Chem. A* **2014**, *2* (25), 9566-9573.

117. Ruud, A.; Miikkulainen, V.; Mizohata, K.; Fjellvåg, H.; Nilsen, O., Enhanced process and composition control for atomic layer deposition with lithium trimethylsilanolate. *Journal of Vacuum Science & Technology A* **2017**, *35* (1), 01B133.
118. Putkonen, M.; Aaltonen, T.; Alnes, M.; Sajavaara, T.; Nilsen, O.; Fjellvåg, H., Atomic layer deposition of lithium containing thin films. *Journal of Materials Chemistry* **2009**, *19* (46), 8767-8771.
119. Sønsteby, H. H.; Bratvold, J. E.; Killi, V. A. L. K.; Choudhury, D.; Elam, J. W.; Fjellvåg, H.; Nilsen, O., tert-butoxides as precursors for atomic layer deposition of alkali metal containing thin films. *Journal of Vacuum Science & Technology A* **2020**, *38* (6).
120. Chisholm, M. H.; Drake, S. R.; Naiini, A. A.; Streib, W. E., Synthesis and X-ray crystal structures of the one-dimensional ribbon chains [MOBut·ButOH] $\infty$  and the cubane species [MOBut]<sub>4</sub> (M = K and Rb). *Polyhedron* **1991**, *10* (3), 337-345.
121. Nekola, H.; Olbrich, F.; Behrens, U., Kristall- und Molekülstrukturen von Lithium- und Natrium-tert-butoxid. *Zeitschrift für anorganische und allgemeine Chemie* **2002**, *628* (9-10), 2067-2070.
122. Coats, A. W.; Redfern, J. P., Thermogravimetric analysis. A review. *Analyst* **1963**, *88* (1053), 906-924.
123. Mass Spectra, NIST Chemistry WebBook. National Institute of Standards and Technology: Gaithersburg MD, Accessed 12/11/2020.
124. Hornsveld, N.; Kessels, W. M. M.; Creatore, M., Mass Spectrometry Study of Li<sub>2</sub>CO<sub>3</sub> Film Growth by Thermal and Plasma-Assisted Atomic Layer Deposition. *The Journal of Physical Chemistry C* **2019**, *123* (7), 4109-4115.
125. Kahn, J. D.; Haag, A.; Schleyer, P. v. R., Mass spectrometry of gas-phase lithium alkoxides. *The Journal of Physical Chemistry* **1988**, *92* (1), 212-220.
126. Hartwell, G. E.; Brown, T. L., The Mass Spectra of Lithiomethyltrimethylsilane and Lithium t-Butoxide. *Inorganic Chemistry* **1966**, *5* (7), 1257-1259.
127. Cavanagh, A. S.; Lee, Y.; Yoon, B.; George, S., Atomic layer deposition of LiOH and Li<sub>2</sub>CO<sub>3</sub> using lithium t-butoxide as the lithium source. *ECS transactions* **2010**, *33* (2), 223.
128. Wang, B.; Liu, J.; Norouzi Banis, M.; Sun, Q.; Zhao, Y.; Li, R.; Sham, T.-K.; Sun, X., Atomic Layer Deposited Lithium Silicates as Solid-State Electrolytes for All-Solid-State Batteries. *ACS Applied Materials & Interfaces* **2017**, *9* (37), 31786-31793.
129. Kazyak, E.; Chen, K.-H.; Davis, A. L.; Yu, S.; Sanchez, A. J.; Lasso, J.; Bielinski, A. R.; Thompson, T.; Sakamoto, J.; Siegel, D. J.; Dasgupta, N. P., Atomic layer deposition and first principles modeling of glassy Li<sub>3</sub>BO<sub>3</sub>-Li<sub>2</sub>CO<sub>3</sub> electrolytes for solid-state Li metal batteries. *J. Mater. Chem. A* **2018**, *6* (40), 19425-19437.
130. Sonsteby, H. H.; Nilsen, O.; Fjellvåg, H., Chemical Uniformity in Ferroelectric K<sub>x</sub>Na<sub>1-x</sub>NbO<sub>3</sub> Thin Films. *Glob Chall* **2019**, *3* (10), 1800114.
131. Sønsteby, H. H.; Nilsen, O.; Fjellvåg, H., Atomic layer deposition of (K,Na)(Nb,Ta)O<sub>3</sub> thin films. *Journal of Vacuum Science & Technology A: Vacuum, Surfaces, and Films* **2016**, *34* (4).
132. Su, J.; Tsuruoka, T.; Tsujita, T.; Nishitani, Y.; Nakura, K.; Terabe, K., Atomic Layer Deposition of a Magnesium Phosphate Solid Electrolyte. *Chemistry of Materials* **2019**, *31* (15), 5566-5575.
133. Putkonen, M.; Sajavaara, T.; Rahkila, P.; Xu, L.; Cheng, S.; Niinistö, L.; Whitlow, H. J., Atomic layer deposition and characterization of biocompatible hydroxyapatite thin films. *Thin Solid Films* **2009**, *517* (20), 5819-5824.

134. McNulty, D.; Buckley, D. N.; O'Dwyer, C., Synthesis and electrochemical properties of vanadium oxide materials and structures as Li-ion battery positive electrodes. *Journal of Power Sources* **2014**, *267*, 831-873.
135. Pan, A.; Zhang, J.-G.; Nie, Z.; Cao, G.; Arey, B. W.; Li, G.; Liang, S.-q.; Liu, J., Facile synthesized nanorod structured vanadium pentoxide for high-rate lithium batteries. *Journal of Materials Chemistry* **2010**, *20* (41), 9193-9199.
136. Brousse, T.; Bélanger, D.; Long, J. W., To Be or Not To Be Pseudocapacitive? *Journal of The Electrochemical Society* **2015**, *162* (5), A5185-A5189.
137. Adamczyk, E.; Anger, E.; Freire, M.; Pralong, V., A chemical redox reaction to generate rock salt-type materials: the case of Na<sub>3</sub>V<sub>2</sub>O<sub>5</sub>. *Dalton Trans* **2018**, *47* (9), 3112-3118.
138. Ali, G.; Lee, J. H.; Oh, S. H.; Cho, B. W.; Nam, K. W.; Chung, K. Y., Investigation of the Na Intercalation Mechanism into Nanosized V<sub>2</sub>O<sub>5</sub>/C Composite Cathode Material for Na-Ion Batteries. *ACS Appl Mater Interfaces* **2016**, *8* (9), 6032-6039.
139. Su, D. S.; Hävecker, M.; Willinger, M.; Schlögl, R., Chemical and Electron Beam Reduction of Vanadium Oxides Monitored by EELS and NEXAFS. *Microscopy and Microanalysis* **2001**, *7* (S2), 440-441.
140. Hamani, D.; Ati, M.; Tarascon, J.-M.; Rozier, P., Na<sub>x</sub>VO<sub>2</sub> as possible electrode for Na-ion batteries. *Electrochemistry Communications* **2011**, *13* (9), 938-941.
141. Li, H.; He, P.; Wang, Y.; Hosono, E.; Zhou, H., High-surface vanadium oxides with large capacities for lithium-ion batteries: from hydrated aerogel to nanocrystalline VO<sub>2</sub>(B), V<sub>6</sub>O<sub>13</sub> and V<sub>2</sub>O<sub>5</sub>. *Journal of Materials Chemistry* **2011**, *21* (29).
142. Chao, D.; DeBlock, R.; Lai, C. H.; Wei, Q.; Dunn, B.; Fan, H. J., Amorphous VO<sub>2</sub> : A Pseudocapacitive Platform for High-Rate Symmetric Batteries. *Adv Mater* **2021**, *33* (49), 2103736.
143. Wei, Q.; DeBlock, R. H.; Butts, D. M.; Choi, C.; Dunn, B., Pseudocapacitive Vanadium-based Materials toward High-Rate Sodium-Ion Storage. *Energy & Environmental Materials* **2020**, *3* (3), 221-234.
144. Su, D. S.; Schlögl, R., Thermal Decomposition of Divanadium Pentoxide V<sub>2</sub>O<sub>5</sub>: Towards a Nanocrystalline V<sub>2</sub>O<sub>3</sub> Phase. *Catalysis Letters* **2002**, *83* (3), 115-119.
145. Cuthbertson, J.; Gray, V. J.; Wilden, J. D., Observations on transition metal free biaryl coupling: potassium tert-butoxide alone promotes the reaction without diamine or phenanthroline catalysts. *Chem Commun (Camb)* **2014**, *50* (20), 2575-8.
146. Baddour-Hadjean, R.; Navone, C.; Pereira-Ramos, J. P., In situ Raman microspectrometry investigation of electrochemical lithium intercalation into sputtered crystalline V<sub>2</sub>O<sub>5</sub> thin films. *Electrochimica Acta* **2009**, *54* (26), 6674-6679.
147. Baba, M.; Kumagai, N.; Fujita, N.; Ohta, K.; Nishidate, K.; Komaba, S.; Groult, H.; Devilliers, D.; Kaplan, B., Fabrication and electrochemical characteristics of all-solid-state lithium-ion rechargeable batteries composed of LiMn<sub>2</sub>O<sub>4</sub> positive and V<sub>2</sub>O<sub>5</sub> negative electrodes. *Journal of Power Sources* **2001**, *97-98*, 798-800.
148. Stewart, D. M.; Pearse, A. J.; Kim, N. S.; Fuller, E. J.; Talin, A. A.; Gregorczyk, K.; Lee, S. B.; Rubloff, G. W., Tin Oxynitride Anodes by Atomic Layer Deposition for Solid-State Batteries. *Chemistry of Materials* **2018**, *30* (8), 2526-2534.
149. Li, X.; Meng, X.; Liu, J.; Geng, D.; Zhang, Y.; Banis, M. N.; Li, Y.; Yang, J.; Li, R.; Sun, X.; Cai, M.; Verbrugge, M. W., Tin Oxide with Controlled Morphology and Crystallinity by Atomic Layer Deposition onto Graphene Nanosheets for Enhanced Lithium Storage. *Advanced Functional Materials* **2012**, *22* (8), 1647-1654.

150. Kozen, A. C.; Joress, H.; Currie, M.; Anderson, V. R.; Eddy, C. R.; Wheeler, V. D., Structural Characterization of Atomic Layer Deposited Vanadium Dioxide. *The Journal of Physical Chemistry C* **2017**, *121* (35), 19341-19347.
151. Rampelberg, G.; Schaekers, M.; Martens, K.; Xie, Q.; Deduytsche, D.; De Schutter, B.; Blasco, N.; Kittl, J.; Detavernier, C., Semiconductor-metal transition in thin VO<sub>2</sub> films grown by ozone based atomic layer deposition. *Applied Physics Letters* **2011**, *98* (16).
152. Lopez, M. C.; Ortiz, G. F.; Arroyo-de Dompablo, E. M.; Tirado, J. L., An unnoticed inorganic solid electrolyte: dilithium sodium phosphate with the nalipoite structure. *Inorg Chem* **2014**, *53* (4), 2310-6.